UC Santa Barbara

UC Santa Barbara Electronic Theses and Dissertations

Title

Visual Processing Mechanism in the Basal Chordate Ciona

Permalink

https://escholarship.org/uc/item/9745578j

Author

Borba, Cezar

Publication Date

2022

Peer reviewed|Thesis/dissertation

eScholarship.org Powered by the California Digital Library
University of California

UNIVERSITY OF CALIFORNIA

Santa Barbara

Visual Processing Mechanism in the Basal Chordate *Ciona*

A dissertation submitted in partial satisfaction of the requirements for the degree Doctor of Philosophy in Molecular, Cellular, and Developmental Biology

by

Cezar G. Borba

Committee in charge:

Professor William C. Smith, Chair

Professor Michael Goard

Professor Sung Soo Kim

Professor Joel H. Rothman

Professor Julie Simpson

September 2022

The dissertation of Cezar Borba is approved.

_____

William C. Smith, Committee Chair

_____

Michael Goard

_____

Sung Soo Kim

_____

Joel H. Rothman

_____

Julie Simpson

September 2022

ACKNOWLEDGEMENTS

It is impossible to list all the people with whom I feel gratitude towards in the duration of my graduate education. I will list a few of them here, but this in no way encompasses everyone who I should acknowledge.

Firstly, my thanks to the Smith lab. It has been a great honor and pleasure to work with the many members in the Smith Lab. Haley, Matt, Erin, Steph, Sam, Michaela, Priscilla, Yishen, Janeva, among others, have been great company and support. I've enjoyed our variety of conversations between experiments to make every second in the lab exciting. All your different forms of support and encouragement helped me in so many ways. I cannot give thanks enough to Bill for not only the opportunity to work in his lab, but for his endless support throughout my PhD. I would absolutely not be where I am today if not for all that Bill has done for me. Thank you so much, Bill! I would also like to thank my thesis committee for all their feedback and support to help me complete this journey. Thank you, Joel, Julie, Michael, and Sung Soo!

Next, I would like to thank my entire family. My parents, Karen and Cezar, who always believed in me and helped me in any way they could. They were ready to celebrate all my successes (and even my setbacks), because no matter what happened, they wanted to be involved and be there for me. Their constant positive energy always kept me going forward. My grandmothers, Neusa and Dorvalina, who always expressed how proud they were of me to take on graduate school and were always supporting me with love and anything else they could do. I love my crazy family!

I would also like to thank my best friend and basically my brother, Giulliano. He's been a constant in my life since 2005, and I could always count on him and his amazing positivity. Despite barely understanding what I do, he would always be willing to provide feedback and support. I could always count on him when I needed someone, and I am forever grateful for our friendship. I love you, bro!

Lastly, but definitely not least, I want to thank my partner and love of my life, my wife, Nany. She has been by my side through all of the good and the bad of this path, and she was a powerful ally to help me battle the almighty imposter syndrome. She refused to ever let me doubt myself, and her support and understanding nature throughout the difficult times made it all possible. Te amo, Nany!

VITA OF CEZAR BORBA

August 2022

EDUCATION

University of California, Santa Barbara
Doctor of Philosophy in Molecular, Cellular, and Developmental Biology, 2022

University of California, Irvine
Bachelor of Science in Neurobiology, 2017

Palo Alto College
Associate of Science in Biology, 2013

WORK EXPERIENCE

University of California, Santa Barbara (2017-2022)
Teaching Assistant
Introductory Biology Lab (Fall 2017 & Winter 2022)
Recombinant DNA Lab (Spring 2021)
Cell Biology Lab (Winter 2019, 2021)

PUBLICATIONS & PRESENTATIONS

*Contributed equally

Zhang, A., Shailja, S., **Borba, C.**, Miao, Y., Goebel, M., Ruschel, R., Ryan, K., Smith, W.C., Manjunath, B.S. 2022. "Automatic Detection and Neurotransmitter Prediction of Synapses in Electron Microscopy". *Biological Imaging*, 1-18.

Borba, C., Kourakis, M.J., Schwennicke, S., Brasnic, L., Smith, W.C. 2021. "Fold Change Detection in Visual Processing". *Front. Neural Circuits* 15:705161.

Bostwick, M.*, Smith, E.L.*, **Borba, C.**, Newman-Smith, E., Guleria, I., Kourakis, M.J., Smith, W.C. 2020. "Antagonistic Inhibitory Circuits Integrate Visual and Gravitactic Behaviors,". *Curr. Biol.* S0960982219316124.

Kourakis, M.J.*, **Borba, C.***, Zhang, A., Newman-Smith, E., Salas, P., Manjunath, B.S., Smith, W.C. 2019. "Parallel Visual Circuitry in a Basal Chordate". *eLife*, 8, e44753.

11th International Tunicate Meeting – Kobe, Japan (July 11-15th, 2022)
Neural Circuits – Cold Spring Harbor, NY (March 16-19th, 2022)
Society for Neuroscience: Global Connectome – Virtual (January 11-13th, 2021)
10th International Tunicate Meeting – Villefranche-sur-mer, France (July 7-12th, 2019)

ABSTRACT

Visual Processing Mechanisms in the Simple Chordate *Ciona*

by

Cezar Borba

In my dissertation studies, I have focused on uncovering the neural circuitry driving sensorimotor behaviors in a remarkable animal - *Ciona*. Understanding the signal transmission properties neurons use to elicit behavior is essential for determining functionality. An advantage to using the *Ciona* larval tadpole is its relatively simple nervous system. Another, and powerful, advantage is the availability of the completely described connectome for the *Ciona* larval-stage central nervous system (CNS). Furthermore, *Ciona* are tunicates, a subphylum of chordates, and are the closest living relatives of vertebrates, making their connectome the sole representative in the chordate phylum. The *Ciona* tadpole larva shows several vertebrate-like features, including a CNS that shows strong conservation with vertebrate CNSs. Despite having only ~180 neurons, *Ciona* larvae have a surprisingly complex set of behaviors. Among these behaviors are negative phototaxis and a response to rapid light dimming called the *dim response* (also known as the looming shadow behavior). Previous work in the Smith lab investigated these two behaviors and showed that they are mediated by distinct groups of photoreceptors. However, the details of the circuits, such as neurotransmitters used, were still unknown. To explore these circuits, I used a range of approaches, including gene expression analysis to discern the distribution of neurotransmitters and their receptors in individual neurons, and behavioral studies using pharmacological agents and behavioral mutants. Together, these approaches allowed me to

fill in many of the details of the circuits predicted by the connectome, and to construct models that link circuits to behavior. In my first published study, I found that the two photoreceptor groups have distinct, but overlapping, circuits. The first circuit is excitatory and responds to the direction of light, driving phototaxis. The second circuit is disinhibitory and responds to rapid changes in light, driving the dim response. In my second published study, I found that both circuits detect fold-change differences. In fold-change detection (FCD), behavioral (i.e., swimming) responses scales with relative change in sensory input, and not to the overall magnitude of the stimulus. Furthermore, the two visuomotor behaviors have different input/output relationships, indicating different FCD strategies. Pharmacological manipulation of specific relay neurons in the *posterior Brain Vesicle* (pBV) led to an extinction of FCD without eliminating the visuomotor behavior, suggesting the FCD circuits lie at the neuronal level outside of the visual organ, as opposed to a mechanism of the photoreceptors. The role of pBV in sensory processing, along with it receiving converging inputs from other sensory systems, has lent further support of the pBV being a vertebrate midbrain homolog. By examining neurotransmitter receptor expression with *in situ* hybridization, I found broad expression of the glutamate receptor, NMDA-R, in the *Ciona* CNS, except in the photoreceptors. When NMDA-R is pharmacologically inhibited, the larvae lose their ability to respond to sensory input, suggesting an important role of the receptor in sensory processing. Further work is necessary to determine the specific components involved in visual processing and FCD, as well as the role of NMDA-R across the sensory systems. The work described here established a model to study sensory neural circuits for behavior in a new chordate model system.

Table of Contents

1. INTRODUCTION

Eve Marder, a scientist well known for her work on neural circuits in the crustacean stomatogastric nervous system, once famously said, “if we want to understand the brain, the connectome is absolutely necessary and completely insufficient”. This is a quote that rings far too true to me. Although knowing all the connections of neurons in a nervous system is helpful, how these connections generate complex behaviors of an animal is usually not readily apparent. The connectome can be seen as a bare wiring diagram of a nervous system, and unless we know the properties of neurons, and how they interact, whether positively, negatively, or by modulation, the connectome is of limited use.

Animals receive various types of information from the environment and make critical decisions about actions in order to survive. The central nervous system (CNS) has specialized areas for different types of sensory signals, and these areas work together to reach a decision on how to respond (or whether to respond at all). This is the subject of this dissertation; I examine the neural circuits involved in behavior, guided in my research by the connectome of the marine invertebrate chordate *Ciona*.

As a model, *Ciona* tadpole larvae offer a small CNS and the availability of a completely described connectome (Ryan et al., 2016). *Ciona* are Chordates, specifically Tunicates, which are the closest living relatives of the vertebrates (Delsuc et al., 2006). This evolutionary relationship is most evident in the *Ciona* tadpole larva. The larvae are roughly 1 mm in length and contain less than 1600 cells (Figure 1A)(Nakamura et al., 2012). The *Ciona* larva has a stereotyped chordate body plan with a long tail containing a central notochord and flanking muscle cells. Anterior to the tail, the trunk contains the larval brain (Figure 1B).

The larval CNS develops in a manner homologous to vertebrates (Hashimoto et al., 2015) and, once formed, has three distinct domains (Ikuta and Saiga, 2007): the brain vesicle (BV; also referred to as the sensory vesicle), the motor ganglion (MG; also referred to as the visceral ganglion) and the caudal nerve cord (CNC; also referred to as the tail nerve cord) (Figure 1B). The structure, function, and genes expressed within the *Ciona* larval CNS has led to the identification of anatomical homologs of vertebrate CNS domains [reviewed in (Hudson, 2016)]. Previously, the entire BV had been equated to the vertebrate forebrain. However, the BV is divided by anatomy and connectivity into the *anterior Brain Vesicle* (aBV) and the *posterior Brain Vesicle* (pBV). The differing anatomy, function, and gene expression of the aBV and pBV reveals a more likely homology to the vertebrate forebrain and midbrain, respectively (this will be expanded on in Chapter 3 of this dissertation). The MG and the CNC are equated with the vertebrate hindbrain and spinal cord, respectively, with the narrow neck region joining the BV to the MG having homology to the vertebrate midbrain/hindbrain junction. Despite having this strong conservation with vertebrate nervous systems, the *Ciona* larva has only ~180 neurons in the CNS (Figure 1C)(Ryan et al., 2016).

Despite the small number of CNS neurons, the *Ciona* larva exhibits complex behaviors. Their larval stage only lasts for a few days, during which the larvae need to find and attach to a substrate to undergo metamorphosis to form the sessile adult. The *Ciona* larvae are free swimming, and therefore rely on sensory systems to navigate and find a substrate. The sensory input utilized by the larva includes visual, geotactic, tactile, and possibly hydrostatic pressure. Despite the relatively short larval stage, visual and gravity responses vary temporally (Bostwick et al., 2020; Kajiwara and Yoshida, 1985; Salas et al., 2018; Svane and Young, 1989; Zega et al., 2006).

I will first briefly review the *Ciona* sensory systems. The two best-studied sensory systems are found in the brain vesicle: the light sensitive ocellus and the gravity-sensitive otolith (Tsuda et al., 2003a). The ocellus is composed of two groups of photoreceptors (Eakin and Kuda, 1971; Horie et al., 2008a; Ryan et al., 2016): Group I and II photoreceptors (PR-I and PR-II, respectively). The PR-I group is larger and contains 23 photoreceptors. These photoreceptors extend their outer segments into a cup-shaped pigment cell that only allows light passing through the lens cells to strike the photoreceptors from one direction. This property is essential for phototaxis. In contrast, the PR-II group contains only 7 photoreceptors and are found adjacent to the PR-I photoreceptors. The outer segments of the PR-II photoreceptors extend into the brain ventricle rather than into the pigment cell, and therefore, unlike the PR-I photoreceptors, receive light from all directions. Outside the ocellus, there is a third group of photoreceptors known as the PR-III. The function of the PR-III photoreceptors is largely unknown, but the group alone is not sufficient to evoke any light response behavior in *Ciona* larvae, as demonstrated through laser ablation (Horie et al., 2008a). PR-III photoreceptors make very few synaptic connections and differentiate later, unlike PR-I and -II, and their presence persistence during early stages of metamorphosis suggests a potential function of PR-III in metamorphosis.

Ciona larvae detect gravity via the otolith organ in the aBV. The otolith contains a single pigmented cell tethered to the ventral floor of the central brain ventricle. As the larvae move with respect to gravity, the pigment cell will move within the ventricle. Two antenna sensory neurons detect the movement of the pigment cell and project axons to the pBV. The movement of the pigment cell is interpreted by the antenna pathway and is used to orient the larva with respect to gravity (Sakurai et al., 2004).

There is an additional putative sensory system in the BV composed of the 16 coronet cells (Moret et al., 2005a; Ryan et al., 2016); however, their function is still unknown. The coronet cell cluster has been speculated to be homologous to the hypothalamus and may also be involved in the metamorphosis process (Lemaire et al., 2021; Moret et al., 2005b, 2005a). In addition to the CNS-associated sensory systems in the BV (photoreceptors and antenna cells), the *Ciona* larva also contains an extensive peripheral nervous system (PNS) consisting of ciliated sensory nerves in the epidermis that transduce mechanical stimuli (Ryan et al., 2018).

The visuomotor responses of tunicate larvae have been studied for over 100 years, and many species have been described to phototax and be responsive to rapid light dimming (Grave, 1920; Kajiwara and Yoshida, 1985; Mast, 1921; McHenry, 2005; Salas et al., 2018; Svane and Young, 1989; Tsuda et al., 2003b, 2003b; Young and Chia, 1985; Zega et al., 2006). It is evident that major behavioral differences exist between species. Despite this, tunicate larval visuomotor behaviors were generalized across species, and often poorly described (McHenry, 2005; Young and Chia, 1985). Previous work in the Smith lab investigated these two behaviors and showed that they are mediated by distinct groups of photoreceptors, with PR-I being responsible for phototaxis, and PR-II being responsible for the dim response (Salas et al., 2018). The primary interneurons of the photoreceptor circuits are known as relay neurons and are found in the pBV. These are known as the *photoreceptor relay neurons* (prRN) and the *photoreceptor-ascending MG neuron relay neuron* (pr-AMG RN). There are six prRNs and they receive input from the PR-I photoreceptors. There are eight pr-AMG RNs, and they receive input from both PR-I and -II neurons. Both relay neuron groups synapse to each other, as well as to the *MG paired descending interneuron*

(MGIN) in the MG, which then project to the motor neurons (MN; Figure 1D-E)(Ryan et al., 2016). The elaboration on the visuomotor circuits and behavior is the focus of this dissertation.

The first chapter of this dissertation covers my first published study in which I describe two parallel visuomotor circuits that are responsive to different visual stimuli using neurotransmitter expression maps and behavioral assays. The next chapter covers my second published study describing the ability of the two previously mentioned circuits to detect fold-change differences in light input, rather than to absolute changes. This work points to the significance of the pBV in sensory processing and highlights its conserved function with the vertebrate midbrain. The final chapter discusses ongoing work on describing glutamate receptor expression in the *Ciona* nervous system. This work highlights the broad role of NMDA receptors, independent of AMPA receptors, in sensory processing, and assists in illuminating essential neurons in the glutamate sensory systems.

1.1 Figures

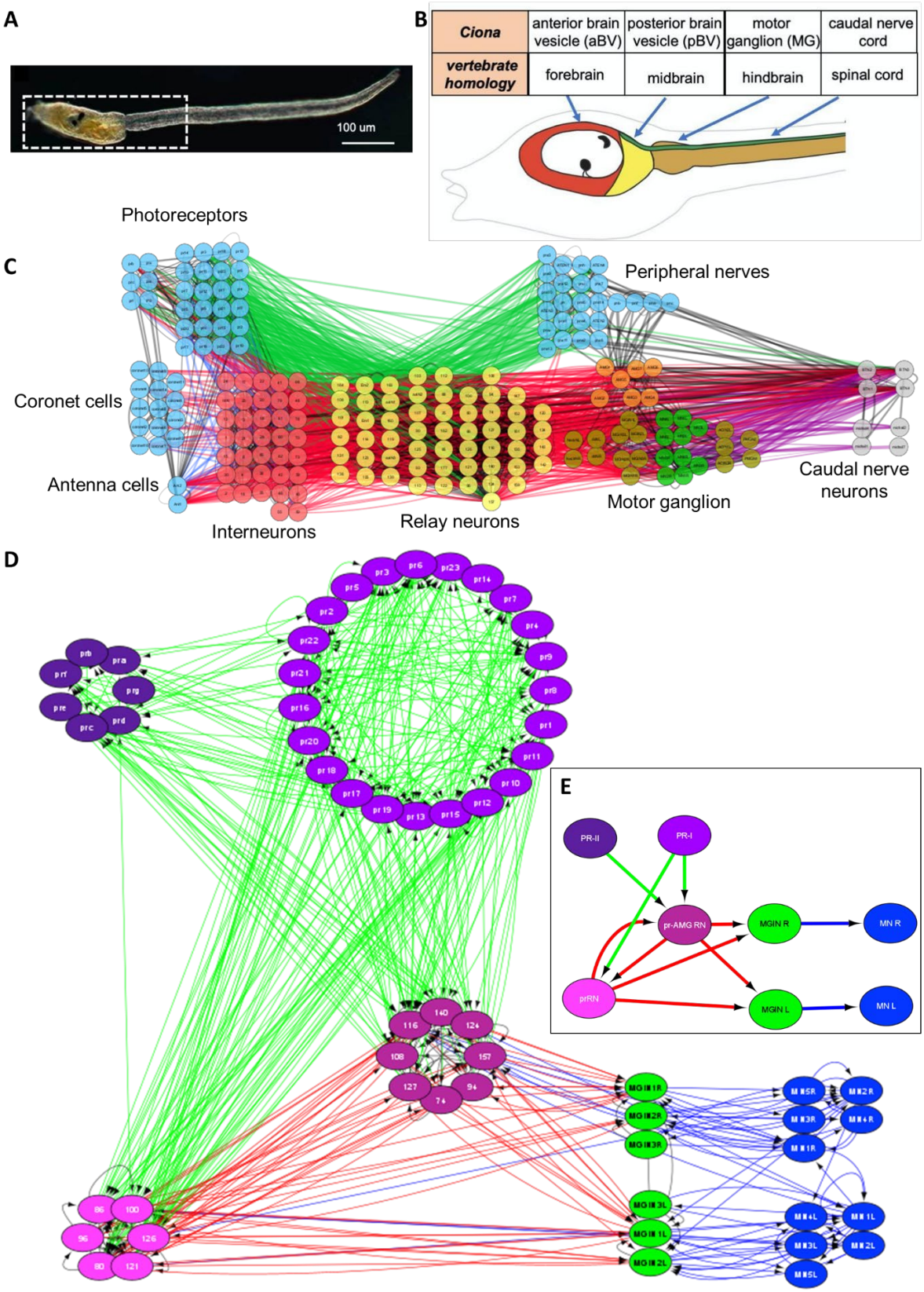
A
100 um
B
Ciona
anterior brain vesicle (aBV)
posterior brain vesicle (pBV)
motor ganglion (MG)
caudal nerve cord
vertebrate homology
forebrain
midbrain
hindbrain
spinal cord
C
Photoreceptors
Peripheral nerves
Coronet cells
Antenna cells
Interneurons
Relay neurons
Motor ganglion
Caudal nerve neurons
D
E
PR-II
PR-I
pr-AMG RN
MGIN R
MN R
prRN
MGIN L
MN L

Figure 1. (A) *Ciona* larva. Box indicates the region shown in B. (B) Major subdivisions in the *Ciona* larval central nervous system and their putative vertebrate homologs. (C) The connectome of the *Ciona* larva. Nodes represent neurons and the lines represent synaptic connection. (D) The minimal visuomotor circuit. Neurons are color coded according to class according to (Ryan et al., 2016). (E) Simplified circuit from D with neurons of same class grouped together. PR-I, group I photoreceptors; PR-II, group II photoreceptors; prRN, photoreceptor relay neurons; pr-AMG RN, photoreceptor-ascending motor ganglion neuron relay neuron; MGIN, motor ganglion paired descending interneuron; MN, motor neuron.

2. PARALLEL VISUAL CIRCUITRY IN A BASAL CHORDATE

Matthew J. Kourakis*, Cezar Borba*, Angela Zhang, Erin Newman-Smith, Priscilla Salas, B. Manjunath, and William C. Smith. 2019. "Parallel Visual Circuitry in a Basal Chordate". *eLife*, 8, e44753. https://doi.org/10.7554/eLife.44753.001

*contributed equally

2.1 Abstract

A common CNS architecture is observed in all chordates, from vertebrates to basal chordates like the ascidian *Ciona. Ciona* stands apart among chordates in having a complete larval connectome. Starting with visuomotor circuits predicted by the *Ciona* connectome, we used expression maps of neurotransmitter use with behavioral assays to identify two parallel visuomotor circuits that are responsive to different components of visual stimuli. The first circuit is characterized by glutamatergic photoreceptors and responds to the direction of light. These photoreceptors project to cholinergic motor neurons, via two tiers of cholinergic interneurons. The second circuit responds to changes in ambient light and mediates an escape response. This circuit uses GABAergic photoreceptors which project to GABAergic interneurons, and then to cholinergic interneurons. Our observations on the behavior of larvae either treated with a GABA receptor antagonist or carrying a mutation that eliminates photoreceptors indicate the second circuit is disinhibitory.

2.2 Introduction

Ascidians, including members of the widely-studied *Ciona* genus, have a biphasic life cycle. At the start of their life, most ascidians spend their first few days as free-swimming

tadpole larvae. It is at the larval stage that ascidians display unmistakable chordate traits, including a prominent notochord running the length of a muscular tail and a dorsal central nervous system (CNS). Ascidian morphology abruptly changes when the larvae attach via their adhesive palps and undergo metamorphosis, the product of which is a sessile filter-feeding juvenile with little resemblance to the larva (Satoh, 1994). Largely because of their conserved chordate body plan, ascidian embryos and larvae have been subjects of extensive investigation (Satoh, 2014). Ascidian larvae are small in comparison to vertebrate larvae, with the *Ciona* larva measuring only about 1 mm in length, with a total of ~2,600 cells (Satoh, 2014). Accordingly, the larval *Ciona* CNS is equally simple, having ~170 neurons (Ryan et al., 2016). Despite this simplicity, *Ciona* larvae display a range of integrated behaviors, including negative gravitaxis and phototaxis, and a response to dimming ambient light, all mediated by central sensory neurons. Also well documented is a mechanosensory/touch response, and possibly chemosensation, mediated by peripheral sensory neurons (Ryan et al., 2018). Anatomically, the *Ciona* larval CNS is comprised anteriorly of the *brain vesicle* (BV; also known as the *sensory vesicle*), a region homologous to the vertebrate forebrain and midbrain, followed by the *neck* region, a homolog of the vertebrate midbrain/hindbrain junction (Figure 2.1). Immediately posterior to the neck is the *motor ganglion* (MG; also known as the *visceral ganglion*). The MG is thought to be homologous to the vertebrate hindbrain and/or spinal cord, and contains ten motor neurons (MN) as well as a number of interneurons – including the two *descending decussating neurons* (ddN) which have been equated with vertebrate Mauthner cells which mediate the startle response (Ryan et al., 2017). With the completion of a synaptic connectome from one larva, the *Ciona* larval nervous system is now one of the best described, with the connectome

providing a detailed and quantitative connectivity matrix of the 6618 chemical and 1206 electrical CNS synapses (Ryan et al., 2016).

The *Ciona* visual system is the best characterized of the larval sensory systems (Kusakabe and Tsuda, 2007; Oonuma et al., 2016). The larval photoreceptors are ciliary, like those of vertebrates, and the photoreceptor opsins and visual cycle systems are, likewise, similar to those found in the vertebrate retina (Kusakabe and Tsuda, 2007; Kusakabe et al., 2001). The primary photoreceptive organ of *Ciona* is the ocellus, which consists of two groups of photoreceptors, three lens cells, and one pigment cell. The first group of photoreceptors (called here, PR-I) is comprised of 23 cells and clustered around the ocellus pigment cell (Figure 2.1). The opsin-containing outer segments of the PR-Is project into the cup shaped pigment cell, making this group sensitive to the direction of incident light and thereby mediating negative phototaxis (Horie et al., 2008a; Salas et al., 2018). The second group of ocellus photoreceptors (PR-II, Figure 2.1) is comprised of seven cells and is adjacent and anterior to the PR-Is and is not associated with the pigment cell. The PR-II cluster mediates the light dimming response, likely with a contribution from the PR-Is, by evoking highly tortuous and leftward-biased swims (Salas et al., 2018). There is a third set of six photoreceptors (PR-IIIs) distal to the ocellus of unknown function, although they are not involved in phototaxis or the dimming response (Horie et al., 2008a), nor do they make extensive connections to interneurons, as do the PR-I and -IIs (Ryan et al., 2016).

The relationship between the ascidian ocellus and visual systems in other chordates is not fully resolved. Vertebrates are characterized by the presence of paired lateral (*i.e.*, retinal) eyes, as well as an unpaired medial/pineal eye (Lamb et al., 2007). The cephalochordate *Amphioxus* by contrast, has four distinct photoreceptive organs (Pergner and Kozmik, 2017).

The amphioxus *frontal eye* has been proposed as homologous to the vertebrate lateral eyes, while the *lamellar body* is thought to be homologous to the vertebrate pineal organ (Pergner and Kozmik, 2017; Vopalensky et al., 2012). The other two amphioxus photoreceptor types, the *dorsal ocelli* and the *Joseph cells*, are thought, based on a number of criteria, including their rhabdomeric morphology- which differs from the ciliary morphology of vertebrate and ascidian photoreceptors- to be vestiges of a more primitive photoreceptive system. Based on various criteria the ascidian ocellus has been proposed as having homology to either the medial or the retinal eyes (Kusakabe et al., 2001; Lamb et al., 2007).

The *Ciona* larval connectome predicts the neural circuity linking photoreceptors to motor activation (Ryan et al., 2016). Figure 2.1 shows the simplified minimal visuomotor circuit in which neurons of the same type are clustered (*e.g.*, photoreceptors) and the number of neurons of each type is indicated in parentheses. The full connectivity for the visuomotor circuit showing all neurons along with chemical and gap junction/electrical synapses (and their relative strengths) is shown in Figure 2.1.1 and 2.1.2, respectively [derived from data tables in (Ryan et al., 2016)]. As shown in Figure 2.1.2, gap junctions are few and relatively small in the BV and become more prominent in the MG.

The minimal circuit shows the PR-I and -II photoreceptors synapsing primarily onto two classes of relay neurons (RNs) in the posterior BV (pBV). The six *photoreceptor RNs* (prRN) receive input exclusively from the PR-I photoreceptors and then project posteriorly to the paired right/left *MG interneurons* (three on each side; MGIN Figure 2.1 and Figure 2.1.1). A second cluster of eight RNs, the *photoreceptor ascending MG RNs* (pr-AMG RN) are postsynaptic to both the PR-I and PR-II photoreceptors, and are so-named because they, unlike the prRNs, receive input from the *ascending MG peripheral interneurons* (AMG

neurons; not shown in Figure 2.1). There are also extensive synaptic connections between the pr-AMG RNs and the prRNs. Like the prRNs, the pr-AMG RNs project posteriorly to the left and right MGINs. The MGINs in turn synapse onto the paired right and left motor neurons (five on each side). The *Ciona* connectome thus predicts a complete visuomotor circuit from photoreceptors to muscle target cells, and provides a valuable comparative model to their chordate cousins, the vertebrates and cephalochordates (Nilsson, 2009; Suzuki et al., 2015; Vopalensky et al., 2012), as well as to other well-described but much more distantly related models such as *Drosophila* and *Platynereis* (Eichler et al., 2017; Larderet et al., 2017; Randel et al., 2014).

In the current study, we report that the *Ciona* PR-I and PR-II visual circuits operate by very different logic. We find that the PR-I circuit is an excitatory relay from glutamatergic photoreceptors signaling to AMPA receptors on cholinergic prRNs. On the other hand, the PR-II circuit initiates with GABAergic photoreceptors synapsing onto GABAergic pr-AMG RNs. Both the sequential array of GABAergic neurons in this pathway and the behavior of larvae treated with GABA inhibitors, or carrying a mutation that misspecifies the anterior BV, support a model in which this circuit is disinhibitory.

2.3 Materials & Methods

2.3.1 Animals

Ciona robusta (a.k.a., *Ciona intestinalis* type A) were collected from the Santa Barbara Yacht harbor or were obtained from M-REP (Carlsbad). *Ciona intestinalis* (type B) were obtained from Marine Biological Laboratory (Woods Hole). The mutant *frimousse* (*frm*) and the pVGAT > kaede stable transgenic line (National Bioresource Project, Japan) were cultured at the UC Santa Barbara Marine Lab, as described previously (Veeman et al.,

2011). Larvae were obtained by mixing dissected gametes of 3 adults and cultured in natural seawater at 18˚C. Homozygous *frm* larvae were produced by natural spawning of heterozygote *frm* adults.

2.3.2 Transgene Constructs

pOpsin1 > RFP. Starting with the plasmid pSP-Ci-opsin 1 (2Kb)>kaede (Takeo Horie and Takehiro Kusakabe, unpublished), the kaede reading frame was replaced with a synthesized RFP (GeneBlock; IDT). *pVGAT > H2B::RFP*. The promoter region of VGAT was amplified from genomic DNA using primers containing adaptors for Gateway cloning attB3 and attB5 sites (ataaagtaggctatttaaacaaccagattgcttctgtct and caaaagttgggt tgaggtcgaacgttccg) (Yoshida et al., 2004). This was cloned into pDONR-221-P3-P5 and recombined with an entry clone containing H2B::RFP (Roure et al., 2007).

2.3.3 Transgenesis

2.3.3.1 Microinjection

Fertilized one-cell *Ciona intestinalis* (type B) embryos were microinjected through the chorion, as described previously for *C. savignyi* (Deschet et al., 2003).

2.3.3.2 Electroporation

Unfertilized *Ciona robusta* eggs were dechorionated using 0.1% trypsin in 10 mM TAPS pH 8.2 in filtered sea water. Eggs were then fertilized and electroporated (Zeller, 2018) with 40 µg each of pVACHT >CFP (Horie et al., 2011) and pVGAT >H2B::RFP. Embryos were cultured at 18˚C in filtered sea water with antibiotics until 18 hpf. Larvae were live-mounted for microscopy.

2.3.4 Hybridization chain reaction (HCR) *in situ*

Ciona intestinalis-type B were used for *in situ* studies and staged to match the animals used in the connectome study (Ryan et al., 2016). Optimized HCR *in situ* probes for each target transcript were obtained from Molecular Technologies. For detection of GABAergic/glycinergic cells, probes were made to the vesicular GABA transporter gene; for glutamatergic cells, probes were made to the vesicular glutamate transporter for cholinergic cells, probes were made to the vesicular acetylcholine transporter. The sequences from which the HCR probe sets were chosen were assembled from scaffold reads available through the Aniseed website (aniseed.cnrs.fr), and are shown in Supplementary file 1 (Kourakis et al., 2019). The *in situ* protocol followed the previously published *Ciona in situ* hybridization protocol (Corbo et al., 1997) until the prehybridization step. At this point, the protocol follows the published HCR protocol (Choi et al., 2018), with the following exception: during the amplification stage, incubation with hairpins is performed for 3 days instead of 12–16 hr.

HCR *in situ* stained larvae were cleared with Slowfade Gold with DAPI (Invitrogen) and imaged on a Leica SP8 resonant scanning confocal microscope. Imaris v. 9.1 (Bitplane) was used to visualize embryos and assign centroids to nuclei using the 'add new spots' function, followed by manual correction when necessary. Nuclei were assigned using the maximum intensity projection, cropped to the area of interest. Volume rendering of *in situ* patterns was also done using Imaris v. 9.1.

2.3.5 Cell registration

A rotation matrix was calculated based on the 3-dimensional vectors between the anchor cells (ddN and/or antenna cells) and the center of the target cells (photoreceptors or relay neurons) using the HCR *in situ* (target set) and connectome cell centroids (source set). The source set was then rotated to an approximate orientation to the target set. Next, the

Coherent Point Drift Algorithm was used to calculate an affine transformation matrix between the source set and the target set of cells (Myronenko and Song, 2010). This algorithm models the source set as a Gaussian Mixture Model (GMM), and the target set is treated as observations from the GMM. The transformation matrix is calculated to maximize the Maximum A Posteriori estimation that the observed point cloud is drawn from the GMM. A nearest neighbor mapping based on Euclidean distance is then used to find the closest corresponding point in the target cell set for each cell in the transformed source cell set. The implementation used was adapted from the pure Python implementation https://github.com/siavashk/pycpd. The maximum number of iterations was set to 1000 and the maximum root mean squared error for convergence was set to 0.001. The code for the registration is available as supplementary material [Source codes 1-3; (Kourakis et al., 2019)].

2.3.5.1 Confusion Matrix

Each dataset containing NT information was registered to every other dataset of the same type using the algorithm detailed above. The EM-registration based cell assignments of each cell in both sets is then compared to each other to see if they agree (Stehman, 1997). The confusion matrix shows the number of times a cell assignment in one dataset corresponds with each other cell assignment in another dataset.

2.3.6 Behavioral Assays

For time-lapse videos the inverted lid of a 60 mm petri dish was first coated with a thin layer of 1% agarose. Larvae were then added to the inverted lid with filtered sea water containing 0.1% BSA with streptomycin and kanamycin each at 20 µg/ml. Finally, the dish was covered with a square of glass leaving no air at the top interface. Stock solutions of

perampanel were dissolved in methanol and diluted to final concentrations of either 5 µm (Santa Cruz Biotech) or 15 µM (Adooq Bioscience) in filtered sea water/BSA/antibiotics. Picrotoxin (Tocris) was also diluted in methanol and used at a final concentration of 1 mM. Control samples received methanol alone.

Time-lapse images were collected using a Hamamatsu Orca-ER camera fitted on a Navitar 7000 macro zoom lens. Programmable 700 nm and 505 nm LED lamps were used to illuminate the larvae (Mightex). All light intensity readings were taken with an Extech Instruments light meter.

2.3.6.1 Dimming-response

All larvae used were between 25 and 28 hpf (18˚C). For image capture, the larvae were illuminated with the 700 nm LED lamp and the camera was fitted with a red filter to block the 505 nm light. The videos were recorded at five fps. In the assays, larvae were first recorded for 10 s with the 505 nm LED light mounted above the dish at 600 lux and then dimmed to specific values while image capture continued for another 3 min. Larvae were allowed to recover for 5 min before being assayed again.

2.3.6.2 Phototaxis

All larvae used were approximately 25 hpf (18˚C). The 505 nm LED light was mounted to one side to the petri dish at approximately 3000 lux. Images were captured at one frame per minute for five hours, with the exception of 30 s capture session at 8.9 fps to assay swimming behavior.

2.3.6.3 Spontaneous Swims

All larvae used were between 26 and 28 hpf. The plates were illuminated with only a 700 nm LED light in order to record dark conditions. The videos were recorded at about 8.9 fps for one minute.

2.3.7 Behavioral data analysis

2.3.7.1 Dim-response criteria

Responses to light dimming were counted if: (1) the larva was stationary at the time of the light dimming, and (2) it swam for longer than 3 s. Three seconds was determined by measuring the duration of tail flicks as previously described (Salas et al., 2018). Larvae that bumped or brushed against other larvae or the dish edges were not counted.

2.3.7.2 Tracking and quantification

Larval swims were tracked using a custom MATLAB script named Estimators of Locomotion Iterations for Animal Experiments (ELIANE). Before uploading to ELIANE, time-lapse images were first processed with Fiji (ImageJ) by subtracting a minimum Z-projection to all the frames and then inverting black and white. ELIANE takes the processed time-lapse images and first creates a background image by averaging the pixels from all the frames. Next, it goes to the initial frame, subtracts the background image, and stores all remaining objects found in the specified region of interest (ROI) as initial objects. Then, analyzing one-by-one the initial objects, it goes frame-by-frame subtracting the background image and analyzing all objects to determine the new position of the object by comparing the Euclidean distances of it to all other objects in that frame. If the object had moved unrealistically fast (>6.5 mm/s), moved outside the ROI, or did not move after a set time (1 min), the object was not analyzed. This MATLAB script can be found in the Supplemental Materials [Source code 4; (Kourakis et al., 2019)].

The spontaneous swims in the *frimousse* experiment were quantified manually.

2.3.7.3 Sampling

Assessment of larval swim parameters were performed using three independent assays. For the spontaneous swims, which were quantified manually, 25 larvae were selected randomly, starting from the center of the plate going outward, only using the ones that could be tracked for the entire minute recording session.

2.3.7.4 Tests of significance

Dimming response significance and swim frequency were calculated using the Wilcoxon rank-sum test; spontaneous swim time significance was calculated using the Student's *t*-test; and the variance of spontaneous swimming significance was calculated using the F-test.

2.4 Results

2.4.1 Glutamatergic and GABAergic photoreceptors

The *Ciona* connectome provides a detailed description of chemical synapse connectivity but it provides no information on neurotransmitter (NT) use. While the expression of genes in the *Ciona* CNS and PNS that mark NT use [*e.g.,* vesicular glutamate transporter (VGLUT), vesicular GABA transporter (VGAT), tyrosine hydroxylase (TH), and vesicular acetylcholine transporter (VACHT) for glutamatergic, GABAergic/glycinergic, dopaminergic and cholinergic neurons, respectively] has been extensively reported (Brown et al., 2005; Horie et al., 2008b; Moret et al., 2005a; Pennati et al., 2007; Takamura et al., 2010), finding exact matches of expression patterns to neurons, or groups of neurons, in the connectome is not always possible. For example, the ocellus is reported to have widespread VGLUT expression, indicating that the *Ciona* photoreceptors, like those of vertebrates are

glutamatergic (Horie et al., 2008b). However, the expression domains of both VGAT and glutamic acid decarboxylase (GAD) are suggestive of a subpopulation of GABAergic/glycinergic photoreceptors (Yoshida et al., 2004; Zega et al., 2008), although the identities of these cells within the ocellus is not known. To investigate this further, fertilized eggs from a stable transgenic *Ciona* line expressing *kaede* fluorescent protein under the VGAT promoter (pVGAT > kaede) (Horie et al., 2011) were microinjected with a pOpsin1 > red fluorescent protein (RFP) construct (Kusakabe et al., 2001, 2004) (Figure 2.2A n = 5 larvae observed). We observed a subset of photoreceptors co-expressing the two fluorescent markers both at the anterior and ventral sides of the ocellus (white and orange arrowheads, respectively). In the field of view shown in Figure 2.2A, the eminens cells is also evident due to its expression of VGAT (white arrow), in agreement with earlier reports of GAD expression (Takamura et al., 2010). To investigate BV VGLUT and VGAT expression in greater detail, we used Hybridization Chain Reaction *in situ* (HCR *in situ*) (Choi et al., 2018) (Figure 2.2B). In agreement with previous reports (Horie et al., 2008b), we observed VGLUT expression in the ocellus (blue arrowhead), the two otolith antenna cells (AC), and in epidermal sensory neurons (red arrowheads). Consistent with the above transgenic data, VGAT was expressed in two separate clusters within the ocellus (white and orange arrowheads), as well as in a separate group of BV neurons outside the ocellus corresponding to previously described VGAT-positive neurons that project axons to the MG (Yoshida et al., 2004) (labeled in Figure 2.2B as RNs, see next section). The anterior VGAT-expressing photoreceptor cluster consisted of 7 cells (±1 cell, n = 17 larvae), while the posterior group consisted of two cells (n = 20 larvae). We also observed a subset of the VGAT-expressing cells in both the anterior and posterior clusters that also expressed VGLUT (Figure 2.2C and

D). In the anterior cluster, we observed that the 2 cells (±1; n = 4 VGAT/ VGLUT double *in situ* larvae) at the anterior edge exclusively expressed VGAT (white arrowheads in Figure 2.2C), while the four cells immediately posterior to these cells co-expressed VGAT and VGLUT. In the posterior cluster we observed in all samples (n = 5) that one of two cells co-expressed VGAT and VGLUT, while the other only expressed VGAT (Figure 2.2C, orange arrowheads).

Given the cellular anatomy of the *Ciona* ocellus, with seven PR-IIs anterior and 23 PR-Is posterior (Horie et al., 2008a; Ryan et al., 2016), and our transgenic and HCR *in situ* results, we assign the PR-IIs as being VGAT-positive, with a subset co-expressing VGLUT (Figure 2.2D). The anterior/ventral location of the two VGAT-only PR-IIs suggest that they are PR-b and -e (Figure 2.2C and D). By contrast, the majority of the PR-Is are exclusively glutamatergic with the exception of two ventral cells, one co-expressing VGAT and VGLUT and the other expressing only VGAT. While the identities of the PR-II subpopulations were evident from the ocellus anatomy, the identities of the two VGAT-expressing PR-Is were initially less clear. To get a better indication of the identities of these two cells we performed a registration of cell centroids from multiple *in situ* datasets (n = 11) with the centroids from the connectome serial section electron microscopy (ssEM) dataset. This registration would only be meaningful if there is strong stereotypy in the number and position of the neurons among *Ciona* larvae. The ocellus photoreceptor somata and their outer segments are known to be arranged in rows, suggesting an ordered cellular architecture (Horie et al., 2008a; Ryan et al., 2016). Moreover, we reasoned that stereotypy in the ocellus, if present, should be evident when registering VGAT- and VGLUT-expressing cells, both across multiple *in situ*-stained larvae, and individually to the ssEM photoreceptor centroids. Convergence of NT

type with registered photoreceptors (both between HCR *in situ* samples and between these and the ssEM sample) would be taken as evidence of stereotypy, and of the validity of making NT use predictions.

For photoreceptor registration, DAPI-stained ocellus nuclei from VGAT and VGLUT *in situ* labeled larvae were segmented from 3D image stacks to serve as cell centroids (nuclei are indicated in Figure 2.2C as red spheres). Based on the *in situ* signal, each centroid was designated as VGAT or VGLUT, or both. Finally, the antenna cell and ddN nuclei in the image stacks were segmented to serve as anchor points for registration. Registration of the segmented HCR *in situ* nuclei to each other and to the connectome PR-I nuclei was done according to (Myronenko and Song, 2010). Briefly, rotation and affine transformations were applied to each set of *in situ* nuclei coordinates to register them individually to the connectome cell nuclei coordinates. The results are presented as a heat map showing for each PR-I the relative frequencies it registered with an *in situ* centroid of each NT type (Figure 2.2E). To assess the validity of registration, a confusion matrix was constructed (Stehman, 1997) (Figure 2.2F). In this analysis, each set of HCR *in situ* centroids was registered to all other HCR *in situ* datasets and to the connectome centroids. The confusion matrix shows the number of times a registration of the HCR *in situ* centroid to a connectome centroid corresponds with the registration of another HCR *in situ* dataset. The higher the values along the diagonal of the matrix, the more the datasets agree with each other when registered to the connectome centroids. From the matrix we observed strong overall support for the registration, although with variable confidence for each photoreceptor. The heat map indicates that among the PR-Is, PR-9 is likely to be exclusively VGAT-positive, while PR-10 is likely to be both VGAT- and VGLUT-positive. The confusion matrix gives high

confidence to this assignment, particularly for PR-9. Although PR-9 and PR-10 appear to stand out from the other PR-Is in their NT use, the connectivity of these two photoreceptors in the visuomotor pathway does not appear to be qualitatively different than the other PR-Is (Figure 2.2.1). Finally, the heat map confirms that the other PR-Is are exclusively VGLUT, however with lower confidence for PR-16, which failed to register well.

2.4.2 Posterior brain vesicle relay neurons are mixed VGAT- and VACHT-expressing

Sensory input from the photoreceptors, antenna cells, coronet cells, bipolar tail neurons and a subset of peripheral neurons is directed to a cluster of ~30 RNs in the pBV. These RNs in turn extend axons through the neck to the MG. Among this cluster are the six prRNs and eight pr-AMG RNs [Figure 2.1; (Ryan et al., 2016)]. Previous *in situ* hybridization studies identified VGAT- and VACHT- expressing neurons in the appropriate place in the BV to be RNs (Yoshida et al., 2004). Moreover, these neurons project axons posteriorly to the MG, a defining characteristic of the pBV RNs. BV neurons expressing other major NTs, including glutamate, dopamine, and serotonin, are neither in the correct brain region to be RNs, nor do they project from the BV to the MG [(Horie et al., 2008b; Moret et al., 2005a; Pennati et al., 2007), and our observations]. By HCR *in situ* we observed that the pBV RNs cluster in two distinct groups along the anterior/posterior axis, with the anterior cluster expressing VACHT, and the posterior group expressing VGAT (Figure 2.3A). We observed an average of 16 (±1.6, n = 9 larvae) VGAT-positive neurons and 11 (±1, n = 8 larvae) VACHT-positive neurons.

Unlike the ocellus, the pBV RN cluster does not have obvious anatomical features, although the various classes of RNs are clustered, with, for example, the antenna cell RNs (AntRN) being posterior to the photoreceptor RNs [Figure 2.3.1, (Ryan et al., 2016)].

However, given the diversity of RN types in the pBV it is unlikely that the expression domains of VGAT and VACHT precisely correspond to the clusters of RN classes. In order to make predictions of NT use in the RNs, we used the same registration approach as with the photoreceptors (n = 7 VGAT/VACHT double *in situ* datasets, Figure 2.3.1). The confusion matrix for the RNs shows a lower level of convergence than for the PR-Is, suggesting that the cellular anatomy of the RN cluster is less structured than the ocellus (Figure 2.3B; Figure 2.3.1). However, the confusion matrix also shows that the RNs are most often confused for other RNs of the same class (white boxes in Figure 2.3B). This is most evident when the registration is performed not with single cells, but with pooled RNs of each class (Figure 2.3C) and is presumably a reflection of the clustering of RN classes in the pBV. Thus, we can have higher confidence in the NT use by RN class than we can have in individual neuron identities. For example, the connectome shows the AntRNs are clustered at the rear of the BV [Figure 2.3.1; (Ryan et al., 2016)], as are the VGAT expressing neurons (Figure 2.3A; Figure 2.3.1). Accordingly, the registration predicts that eight of the ten AntRNs are VGAT positive (Figure 2.3C). For the present study, which focuses on the visuomotor pathway, the registration predicts that five of the eight pr-AMG RNs are VGAT expressing, two are VACHT expressing, and one (pr-AMG RN 157) cannot be resolved (no dual VGAT/VACHT expression was observed in the *in situs*). On the other hand, the registration predicts that the six prRNs are evenly mixed between VGAT and VACHT expression. These predictions provide starting points for experimental validation detailed below.

2.4.3 The motor ganglion contains a mixture of cholinergic and GABAergic neurons

The MG contains five left/right pairs of motor neurons, as well as several classes of interneurons, including six MGINs, seven AMGs, two ddNs, and two posterior MG

interneurons (Ryan et al., 2016). Also described in the MG are two left/right pairs of decussating VGAT-positive neurons (Horie et al., 2009; Nishino et al., 2010). These are likely the same decussating MG neurons as described in the connectome, although the names are slightly different [*anterior caudal inhibitory neurons* (Horie et al., 2009) versus *ascending contralateral inhibitory neurons* (Ryan et al., 2016), both abbreviated as ACIN]. However, the connectome reports only three ACINs, with the anterior ACIN not paired. It was speculated that this was an anomalous feature of the particular larva used for the ssEM. Supporting this, a second larva being analyzed by ssEM for connectomics shows two pairs of ACINs (K. Ryan, personal communication).

Like the ocellus, the MG has a well-defined anterior-to-posterior and dorsal-to-ventral cellular anatomy [Figure 2.4A and B; (Ryan et al., 2016, 2018)]. Neurotransmitter use by some MG neurons is already documented, including the motor neurons, which are cholinergic (Takamura et al., 2002, 2010), and the ACINs which are glycinergic (Nishino et al., 2010). By HCR *in situ*, we observed VGAT- and VACHT-positive neurons in the MG (Figure 2.4B), but no VGLUT- or TH-positive cells (data not shown). These results are consistent with previous studies (Horie et al., 2008b; Moret et al., 2005a). Likewise, it was reported that no serotonergic cells were present in the MG (Pennati et al., 2007). As with the RNs, the VGAT- and VACHT-expressing neurons in the MG are segregated anatomically. We also found a population of 6–7 cells between the AMGs and the MNs (asterisks in Figure 2.4A) that were not annotated in the connectome as neurons and that failed to label with any of our NT markers. We hypothesize that these are ependymal cells, which are abundant in the nerve cord immediately caudal to this region.

Because of the highly structured MG cellular anatomy, we can identify the various MG cell types in the *in situ* data. The anterior group of VGAT-positive cells is clustered dorsally in the MG, and correspond to AMGs [Figure 2.4C, D, and E; (Ryan et al., 2017)]. In a dorsal view of the MG (Figure 2.4F, G, and H) a ring of VGAT-positive cells was observed with a non-VGAT expressing cell in the center (asterisk, Figure 2.4F and G). The VGAT-expressing cells appear to be AMGs 1, 2, 3, 4, 6, and 7, while the central cell, which is instead positive for VACHT, appears to be AMG5. The connectome shows that AMG5 differs in its connectivity from the other AMGs. Significantly, AMG5 is the principle synaptic input for PNS neurons. It then synapses to the other AMGs, which in turn project their axons to other cells in the MG, including MGINs and MNs, as well as to the pr-AMG RNs in the BV. In the posterior of the MG, we observed two pairs of VGAT-positive neurons, as described previously (Horie et al., 2009). Finally, in the ventral MG we observed a continuous block of VACHT expression that encompasses the anterior three pairs of MNs, the ddNs, and the MGINs. Similar *in situ* patterns were observed in most larvae (Figure 2.4.1), although the positions of the ACINs were offset in several (see larvae 5 and 6 in Figure 2.4.1), and one larva was observed to be missing both one motor neuron and one ACIN (larva 7 in Figure 2.4.1), suggesting that MG variants, such as was observed in the animal used in the connectome study, may be relatively common.

2.4.4 Parallel visuomotor circuits

Our results indicate that the PR-Is, with the exception of two cells, are glutamatergic, while the PR-IIs are a mixture of GABAergic and GABA/glutamatergic. The *Ciona* genome contains a single glutamate AMPA receptor (AMPAR) (Okamura et al., 2005) that is expressed in larvae in the two antenna cells, and in a small cluster of neurons in the pBV

(Hirai et al., 2017). Published results show that most of the pBV group of AMPAR-positive neurons are clustered at the ends of Arrestin-labeled photoreceptor axons, and that they extend their axons to the MG, suggesting they are photoreceptor RNs [see Figure 2B" in (Hirai et al., 2017)]. We find that this pBV group is composed of ~6 cells (Figure 2.5.1). To investigate this further, we co-expressed an pAMPAR >GFP construct (Hirai et al., 2017) with pVACHT >CFP and pVGAT >nuclear RFP constructs. We observed co-expression of the AMPAR reporter in a subset of the VACHT-positive RNs, but never in the VGAT-expressing RNs (Figure 2.5A).

To assess the function of the AMPAR-positive cells in *Ciona* visuomotor behaviors, we used the non-competitive AMPAR antagonist perampanel (Hanada et al., 2011). For the assay, larvae were treated at 25 hr post fertilization (hpf) with perampanel in sea water and compared to vehicle-treated control larvae for both negative phototaxis and response to light dimming. The negative phototaxis assay consisted of placing the larvae in a 10 cm petri dish of sea water with a 505 nm LED lamp placed to one side [described by us previously (Salas et al., 2018)]. Images were collected at 1 min intervals over 5 hr to assess for taxis [Video 1 in (Kourakis et al., 2019)]. Figure 2.5B and C show representative frames from the time-lapse capture at the start and at 60 min for control and perampanel-treated larvae, respectively. In the control sample, the larvae at 60 min were observed to cluster at the side of the petri dish away from the light (distal side; red arrows in Figure 2.5B). By contrast, no taxis was observed in the perampanel treated larvae (Figure 2.5C). Combined results from three independent assays (n = 129–365 larvae per group) are shown in Figure 2.5D and presented as the percent of larvae found on distal third of the petri dish. For control larvae

~70% swam to the distal third within 1 hr, while the perampanel-treated larvae remained evenly distributed across the dish.

The inability of the perampanel-treated larvae to undergo phototaxis was not the result of an inability to swim, as seen in Video 2 in (Kourakis et al., 2019) which was taken at 8.9 fps, with and without perampanel. Moreover, we observed that perampanel treatment had no effect on the light dimming response [Video 3 in (Kourakis et al., 2019)]. Figure 2.6A and B show 5 s projection images from Video 3 immediately before and after dimming. In these images, swims appear as lines, and the responses in control and perampanel-treated larvae appear qualitatively similar. To quantitatively compare dimming response, control and perampanel-treated larvae were exposed to a range of dimming intensities from 2 to 60-fold and the percentage of larvae responding was measured and presented as a percentage in Figure 2.6C (results are from three independent assays, with 46–139 larvae per group). The percentage responding at all intensities was very similar for both groups, and pair-wise comparisons at each fold change failed to show significance. In addition, no differences were measured in the velocity or duration of swims in pair-wise comparisons of control and perampanel-treated larvae at any fold-dimming (data not shown). We conclude that there is no change in sensitivity to dimming caused by perampanel treatment, while phototaxis was completely disrupted. Finally, we also observed that the touch response was not inhibited by perampanel (data not shown), despite the presence of VGLUT-positive epidermal sensory neurons (Horie et al., 2008b). This would appear to agree with the observation that primary RNs for the PNS, the eminens cells and the AMGs, do not express the AMPAR [(Hirai et al., 2017); and our observations]. In addition to the AMPAR, the *Ciona* genome contains several

other glutamate receptors including one kainate and one NMDA (Okamura et al., 2005), although their expression has not been characterized.

In summary, we are able to separate the phototaxis and dimming behaviors pharmacologically. Moreover, we can identify the VACHT/AMPAR-positive RNs as essential for an excitatory PR-I circuit that involves presynaptic glutamatergic PR-Is and postsynaptic cholinergic MGINs. The number and location of the VACHT/AMPAR-positive RNs, the circuit logic, and our behavioral observations are all consistent with these being prRNs.

2.4.5 A disinhibitory circuit

Of equal significance to our observation that navigation is inhibited by perampanel, is our observation that the dimming response, which is mediated by the PR-IIs (Salas et al., 2018), is not inhibited by perampanel (Figure 2.6). Our expression studies show that the PR-IIs are comprised of a mixture of VGAT- and VGAT/VGLUT-expressing photoreceptors. Although it is formally possible that PR-IIs signal exclusively via glutamate in an excitatory circuit via a non-AMPA glutamate receptor on their RNs, our observations that several of the PR-IIs are VGAT-only, as are the majority of the pr-AMG RNs, suggests an alternative disinhibitory circuitry logic. This circuit would consist of the inhibitory PR-IIs synapsing to the pr-AMG RNs to reduce their inhibition on the cholinergic MGINs.

Implicit in the disinhibitory model is an autonomous level of motor activity in larvae that could be inhibited by the GABAergic pr-AMG RNs, and that this inhibition is released upon stimulation of the GABAergic PR-IIs. We investigated this possibility by two approaches. In the first approach, we inhibited GABAergic receptors with picrotoxin (Olsen, 2014), which should inhibit signals from the GABAergic photoreceptors and the pr-AMG

RNs (and most likely the AntRNs), as well as PNS relay neurons, including the eminens cells and the AMGs. The ACINs, which are essential for the central pattern generator (Nishino et al., 2010), are glycinergic and should not be inhibited by picrotoxin. In the second approach, we took advantage of a previously described *Ciona* mutant, *frimousse (frm)* (Deschet and Smith, 2004; Hackley et al., 2013). In homozygous *frm* larvae, the anterior BV is transfated to epidermis due to a null mutation in a neurula stage-specific connexin gene (Hackley et al., 2013). *Frm* larvae thus lack the ocellus pigment cell and photoreceptors, as well as the otolith, although the motor ganglion appears intact (Deschet and Smith, 2004; Hackley et al., 2013).

2.4.6 Pharmacological GABA receptor inhibition increases spontaneous swims, but decreases dimming response

We first assessed the effects of picrotoxin on spontaneous swimming. As reported previously, when observed under far-red illumination [*i.e.*, outside of the larval response range (Nakagawa et al., 1999)] *Ciona* larvae display spontaneous swims consisting primarily of short 'tail flicks', with very few sustained swims (Salas et al., 2018). In these conditions, we observed that the frequency of spontaneous swims in the picrotoxin-treated group increased significantly when compared to vehicle-treated [Figure 2.7A; Video 4 in (Kourakis et al., 2019); $p=2.2x10^{-16}$, n = 75 for both]. For this assay, the swimming activity of the larvae was recorded in 1 min videos at 8.9 fps. Each circle in Figure 2.7A corresponds to a single larva tracked over one minute, and the number of swim bouts for each larva during the 1 min is plotted along with the average (red circle) and standard deviation (S.D.). In comparing the duration of the spontaneous swims of the two groups (picrotoxin- and vehicle-treated) we observed an interesting distribution (Figure 2.7B). Overall, the swims for the

picrotoxin group were shorter ($p=8.8x10^{-12}$, n = 184 and 542 for control and picrotoxin respectively), although the picrotoxin group showed more variation, with a number of long-swimming outliers.

In the above assays, behavioral responses were measured within ~20 min of adding picrotoxin (or vehicle only). We observed that longer exposure to picrotoxin (>1 hr) resulted in the nearly complete inhibition of spontaneous and induced swimming behavior, presumably due to overactivation at excitatory synapses following removal of inhibitory input. However, this could be reversed by washing out the picrotoxin (data not shown). This inhibitory effect was evident in assessing negative phototaxis behavior of picrotoxin-treated larvae. While these assays are typically conducted over several hours (*e.g.*, Figure 2.5D), this was not possible with the picrotoxin-treated larvae. Nevertheless, the picrotoxin-treated larvae did show negative phototaxis when measured at 1 hr, although the response was dampened in comparison to controls [Figure 2.7C; $p=8.7x10^{-4}$ and p=0.03 for control and picrotoxin respectively, n = 137–487; also see Video 5 in (Kourakis et al., 2019)].

When assessed for the dimming response, the picrotoxin-treated larvae showed a large decrease in evoked sustained swims (defined as lasting longer than 10 s) [Figure 2.7D; Video 6 in (Kourakis et al., 2019)]. Instead, we observed a preponderance of very short swims that likely reflect the elevated rate of spontaneous tail-flick swims in the larvae. Nevertheless, there remained a number of sustained swims in the picrotoxin-treated larvae. While it is possible that these were due to incomplete inhibition by picrotoxin, we feel it was more likely due to a small contribution from the PR-Is to the dimming response, as we have speculated previously (Salas et al., 2018). In support of this, we observed that treatment of larvae with picrotoxin and perampanel completely eliminated the evoked sustained swims.

We documented that swims evoked by the PR-Is have lower tortuosity (*i.e.*, are straighter) than those evoked by the PR-IIs (Salas et al., 2018). Consistent with this, we found the tortuosity of the sustained swims from the picrotoxin-treated larvae had lower tortuosity than those of the vehicle-treated controls (Figure 2.7E; n = 19 and 60, respectively; p=0.003).

2.4.7 *Frimousse* mutants have increased spontaneous swim frequency

We found that observation of larvae homozygous for the *frm* mutation also supported the disinhibitory mechanism. As would be predicted due to their loss of photoreceptors (Hackley et al., 2013), *frm* larvae showed no response to light (our unpublished observation). Despite the defects in the anterior BV, the MG is intact in *frm* larvae as assessed by both gene expression and morphology [(Deschet and Smith, 2004) and Figure 2.8A]. Moreover, not only can *frm* larvae swim, they show increased frequency of spontaneous swims compared to wild type larvae (Figure 2.8B) when assessed using the same parameters as for the picrotoxin-treated larvae (n = 75 for both; $p<5x10^{-16}$). Although the frequency of swims was higher in *frm* larvae, the average swim time was not significantly different between the two (Figure 2.8C; n = 260 and 608, respectively). However, as with the picrotoxin-treated larvae, a handful of very long swims were observed uniquely in the *frm* group (Figure 2.8C). Despite the similarity in the swim times between the *frm* and wild type larvae, the swim characteristics were very different [Video 7 in (Kourakis et al., 2019)], with the swimming of *frm* larvae being much more stereotyped. For example, while average swim times of wild-type and *frm* larvae were very similar (Figure 2.8C), the standard deviations of swim times calculated and plotted for each larva show much lower swim-to-swim variation in the *frm* larvae (Figure 2.8D; $p<5x10^{-15}$). The stereotypy was even more pronounced when the time interval between swims was analyzed (Figure 2.8E). For wild-type larvae, the standard

deviations of interval times showed a wide range of values (*i.e.*, high variability of interval times), while the standard deviations for *frm* larvae were much lower ($p<0.0005$). We did not observe an increase in stereotypic behavior in comparing picrotoxin- to vehicle-treated larvae (data not shown). The behavior of *frm* larvae is characteristic of an oscillator that evokes spontaneous swims with the frequency of ~8/min. Thus, sensory input from the BV appears to suppress this oscillatory behavior, leading to less frequent and more varied swims in wild-type larvae, supporting a disinhibitory circuit. Interestingly, we observed some VGAT and VACHT expression in the remnant of the *frm* BV (Figure 2.8A). While these expressing cells may be RNs, it remains to be determined whether in the absence of sensory input they develop properly, and if they are functional, how their apparent opposing activities might influence spontaneous swimming (albeit elevated).

2.5 Discussion

Figure 2.9 presents a model of the *Ciona* visuomotor circuitry that takes into account the connectome, neurotransmitter use, and behavioral observations. Absent from this model is the detailed and unique connectivity of each neuron in these pathways (Figure 2.1.1), as well as the inputs from other neurons which are not part of the minimal circuit. Nevertheless, we feel that this model will serve as a useful starting point for more detailed analyses of these components. Our findings support a model for two parallel visuomotor pathways, one mediated by the PR-Is and sensitive to the direction of light, and the other mediated by the PR-IIs and sensitive to changes in ambient light. A number of other sensory systems, including mammalian vision and olfaction and *Drosophila* CO_2 detection (Callaway, 2005; Geramita et al., 2016; Lin et al., 2013) similarly split components of sensory information into parallel circuits. The PR-I circuit is a simple excitatory pathway with glutamatergic

photoreceptors projecting to cholinergic prRNs, exciting them via cation-specific ionotropic AMPARs. The prRNs in turn synapse to the cholinergic MGINs, and then these onto the MNs. The fact that glutamate is used by the *Ciona* larvae exclusively in sensory neurons (photoreceptors, antenna cells, and epidermal sensory neurons), coupled with the very limited distribution of AMPARs, allowed us to validate essential components of this circuitry with perampanel. The PR-Is also synapse onto the pr-AMG RNs, which are predicted to be primarily GABAergic. Our observation that AMPAR expression is exclusive to the cholinergic RNs suggests that the response of GABAergic cells to the PR-Is may differ from cholinergic cells, and perhaps plays a role in visual information processing. In fact, the interconnections between the pr-AMG RNs and the AMPAR-expressing prRNs (black arrow Figure 2.9; see also Figure 2.1.1), are suggestive of an incoherent feedforward loop (Alon, 2007). We have already documented that *Ciona* larvae are able to phototax in a wide range of illumination conditions (Salas et al., 2018), and moreover, we have found that *Ciona* larvae show robust fold-change detection (Adler and Alon, 2018) behavior (see chapter 4). Together these observations suggest that the RN cluster plays a role in visual processing, rather than simply passing information to the MG.

Our model for the PR-II mediated dimming/escape behavior is more surprising and includes a novelty – inhibitory photoreceptors. From *in situ* hybridization we observed that some PR-IIs exclusively express VGAT, while other co-express VGAT and VGLUT. The significance of VGAT/VGLUT co-expression in the *Ciona* visuomotor pathway is not yet clear, although similar co-expression is widely observed in mammalian brains (Fattorini et al., 2015; Zander et al., 2010) and invertebrates (Fabian-Fine et al., 2015). It is speculated that co-release of GABA and GLUT may serve to tune excitatory/inhibitory balance. While

the connectome shows that not all of the PR-IIs project to the RNs, with a subset instead forming extensive connections to other PR-Is and PR-IIs, the connectome indicates that several of the VGAT-exclusive PR-IIs do project to the pr-AMG RNs [Figure 2.2E and (Ryan et al., 2016)], consistent with our hypothesis that the PR-II output to the pr-AMG RNs is predominantly inhibitory.

The *Ciona* genome encodes seven ionotropic/Cl^- GABA receptor subunit genes ($GABA_A$) (Okamura et al., 2005), but does not have an ortholog of the cationic EXP-1 GABA receptor (Beg and Jorgensen, 2003), confirmation that the GABAergic synaptic events are most likely inhibitory. In addition, electrophysiological studies done nearly fifty years ago on larvae of the ascidian *Amaroucium constellatum* reported that their photoreceptors, like those of vertebrates, were hyperpolarizing (Gorman et al., 1971). In other words, dimming is likely to result in a release of GABA from the PR-IIs. Although the heterogeneity of ascidian photoreceptors (*e.g.*, PR-I and –II) was not known at the time, both the vertebrate-like ciliary structure shared by all *Ciona* photoreceptors and the structure of *Ciona* opsins appear to rule out the possibility of depolarizing phototransduction (Kusakabe and Tsuda, 2007; Kusakabe et al., 2001). Also in agreement with an inhibitory output from the PR-IIs is our prediction that the majority of the pr-AMG RNs, the exclusive RNs of the PR- IIs, are themselves GABAergic, which would make a disinhibitory circuit most plausible (Figure 2.9). We also show that removal of BV sensory input with the *frm* mutant, or inhibition of GABA receptors with picrotoxin, leads to more frequent spontaneous swims, suggesting that a disinhibitory pathway could lead to stimulation of swimming. Finally, we observed that the AMGs, with the exception of one cell, are GABAergic. The AMGs are one of the primary relay centers for the PNS (Ryan et al., 2018) and project to the MGINs and

MNs. However, the AMGs also project ascending axons to the pr-AMG RNs. It is thought that the convergence of PR-II and AMG inputs at the pr-AMG RNs serves to initiate an integrated escape response (Ryan et al., 2018). Our finding that these two classes of neurons (PR-IIs and AMGs) are likely to have the same input (inhibition) on the pr-AMG RNs further bolsters the integrated response model. Finally, the PR-II mediated dimming response was not inhibited by the AMPAR antagonist perampanel, suggesting the PR-II glutamate release at pr-AMG RNs acts through other receptors, such as the NMDA receptor, and may be more involved in modulating or processing the visual response, and that GABA release may be more important.

Validation of this hypothetical disinhibitory circuit will require analysis of individual neurons in behaving larvae. Although we have been able to get robust GCaMP imagery from the CNSs of transgenic *Ciona* larvae (our unpublished observations), the fact that the excitation and emission spectra of GCaMP (as well as red-shifted calcium indicators) overlap with the behavioral spectrum of *Ciona,* and the inefficacy of GCaMP for visualizing inhibition, led us to abandon this approach. We are currently exploring methods for electrophysiological recording of *Ciona* BV neurons.

2.5.1 Ascidians and the evolution of vertebrate visual systems

The evolutionary relationship between the ascidian ocellus and the visual organs of cephalochordates (*e.g.*, amphioxus) and vertebrates remains unclear (Kusakabe and Tsuda, 2007; Lamb, 2013; Lamb et al., 2007). The observations that the *Ciona* PR-I and PR-II complexes are distinct morphologically, mediate different behaviors, project via distinct visuomotor circuits, and express different NTs, raises the possibility that these two complexes may have independent origins, and thus have different evolutionary relationships

to the photoreceptor organs of other chordates. We speculate that the ascidian PR-I complex is likely to be homologous to the vertebrate lateral eyes and the amphioxus frontal eye, which like the PR-I complex is pigmented and appears to play a role in detecting the direction of light, although not necessarily in taxis (Stokes and Holland, 1995). On the other hand, the pineal eyes of amphibian tadpoles and fish larvae mediate a shadow/dimming response, suggesting homology with the ascidian PR-II photoreceptor complex (Jamieson and Roberts, 2000; Yoshizawa and Jeffery, 2008). Nevertheless, the inhibitory nature of the *Ciona* PR-IIs makes assigning homologies more difficult. It is possible that use of GABA by these photoreceptors is a derived feature of ascidians, as inhibitory photoreceptors have yet to be described elsewhere. Alternatively, in the vertebrate retina GABAergic/glycinergic horizontal and amacrine cells are prevalent, and, moreover, it has been proposed that these cells, as well as ganglion cells, are derived from an ancient photoreceptor (Arendt, 2003; Lamb, 2013). While this may imply an alternative evolutionary origin for the *Ciona* PR-IIs, these observations may simply support the plasticity of NT use in visual systems.

2.5.2 Acknowledgements

We thank Takeo Horie and Takahiro Kusakabe for the opsin1 promoter construct; Yasunori Sasakura for the stable pVGAT >kaede line and pVACHT >CFP plasmid; Haruo Okado for the pAMPAR >GFP construct. Kerrianne Ryan for her helpful discussion and sharing unpublished data. Chelsea Parlett-Pelleriti for her advice on statistical analysis. We acknowledge the use of the NRI-MCDB Microscopy Facility and the Resonant Scanning Confocal supported by NSF MRI grant 1625770. This work supported by an award from NIH (NS103774) to WCS and BM.

2.6 Figures

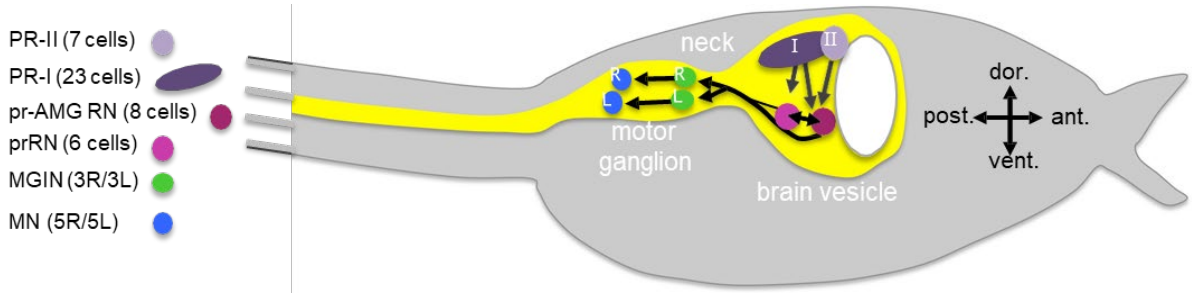

Figure 2.1. Cartoon of a *Ciona* tadpole larva with outline of the central nervous system. The minimal visuomotor circuit is shown with circles representing classes of neurons with the number of cells of each class indicated in the parentheses of the key. Abbreviations: dor., dorsal; vent., ventral; ant., anterior; post., posterior; PR-II, photoreceptor group II; PR-I, photoreceptor group I; pr-AMG RN, photoreceptor ascending motor ganglion relay neuron; prRN, photoreceptor relay neuron; MGIN, motor ganglion interneuron; MN, motor neuron. L, left; R, right. Cell types are color coded according to (Ryan et al., 2016).

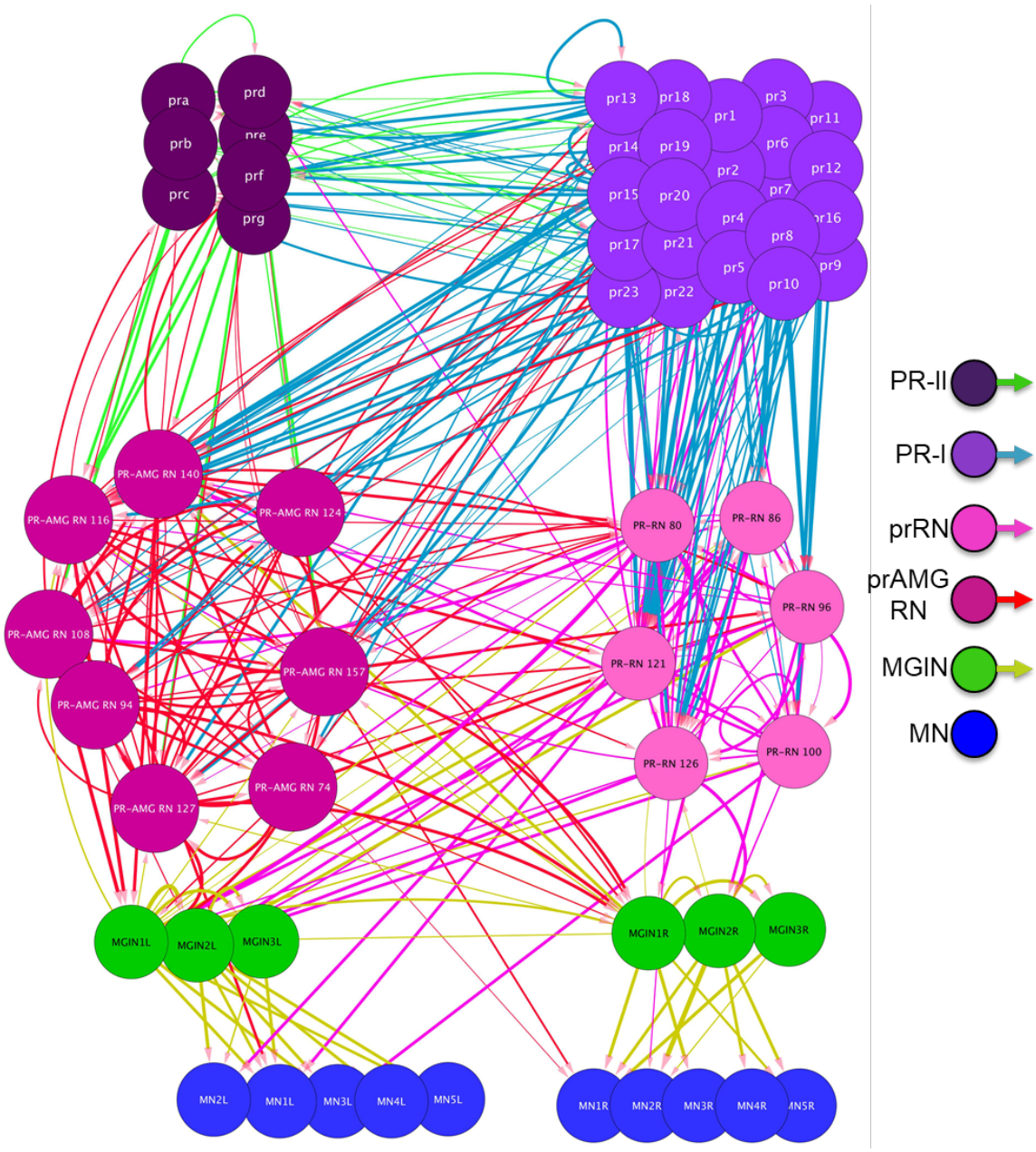

Figure 2.1.1. Chemical synapse connectivity of minimal visuomotor system of *Ciona*. Electrical synapse connectivity of minimal visuomotor system of *Ciona*. Both panels derived from data in (Ryan et al., 2016). Thickness of lines is proportional to synapse strength. Abbreviations: PR-II, photoreceptor group II; PR-I, photoreceptor group I; pr-AMG RN, photoreceptor ascending motor ganglion relay neuron; prRN, photoreceptor relay neuron; MGIN, motor ganglion interneuron. L, left; R, right.

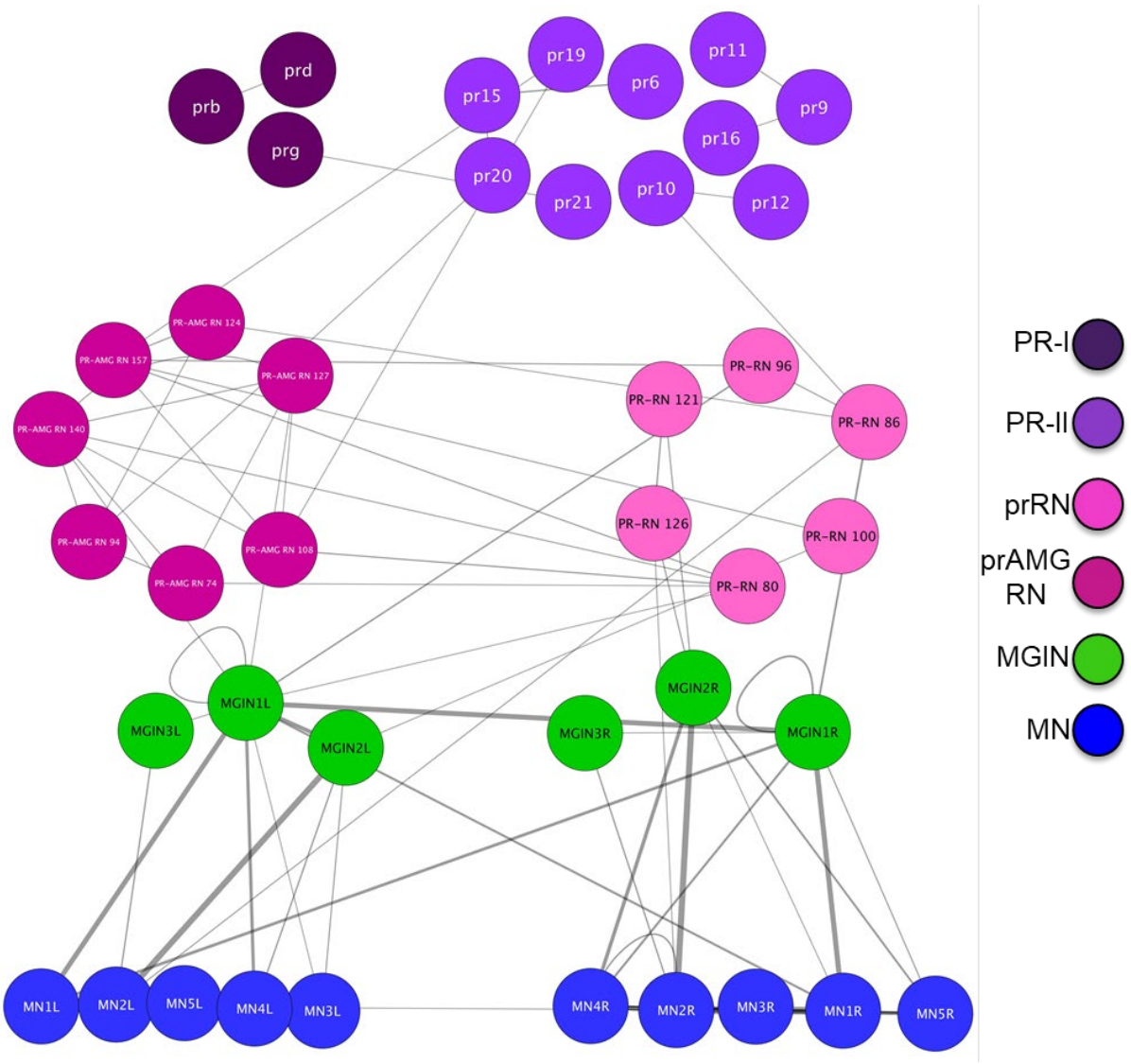

Figure 2.1.2. Electrical synapse connectivity of minimal visuomotor system of *Ciona*.

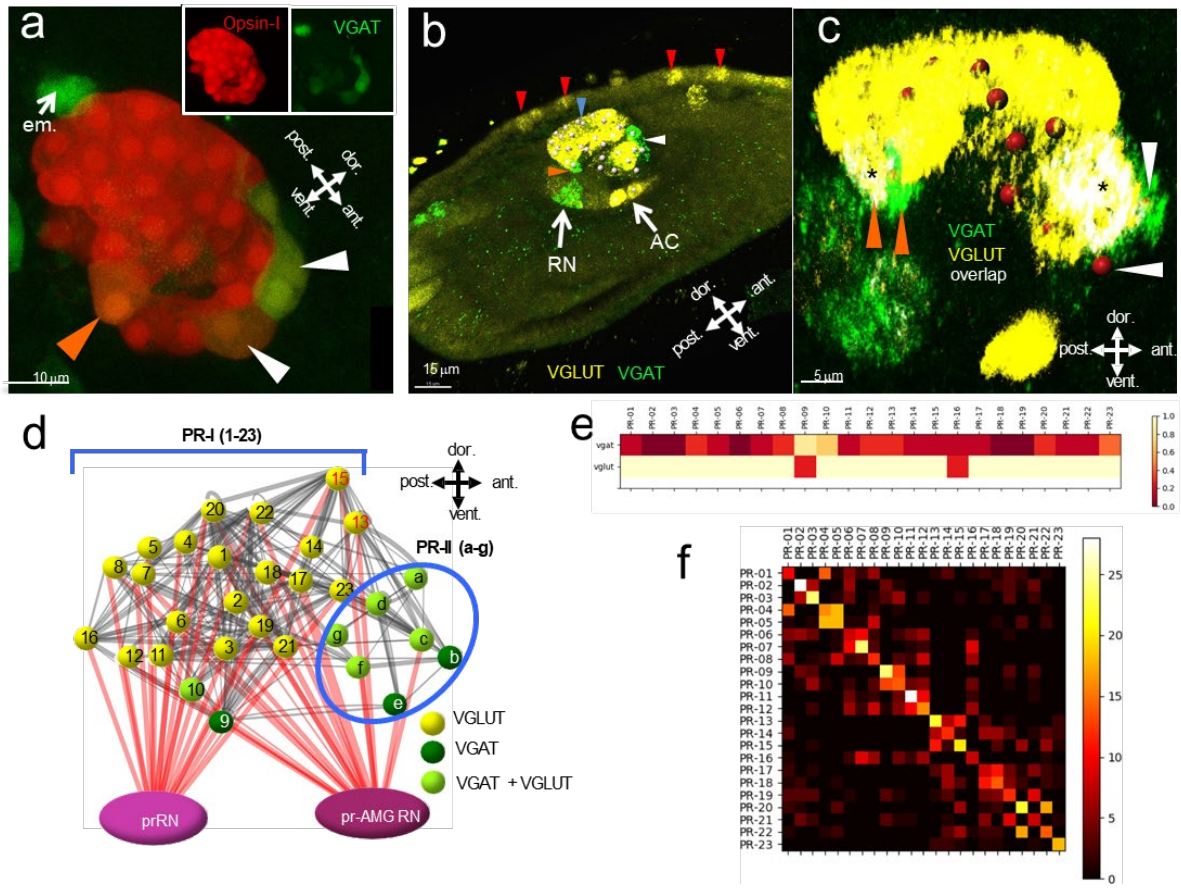

Figure 2.2. Neurotransmitter use in the ocellus. (a) Coexpression of opsin and VGAT reporter constructs in the ocellus (white and orange arrowheads). Insets show expression of Opsin-1 and VGAT individually. (b) Expression of VGLUT and VGAT in the brain vesicle and epidermis by *in situ* hybridization. VGAT was observed in an anterior (white arrowhead) and posterior (orange arrowhead) domain of the ocellus. Blue arrowhead indicates VGLUT expression in the ocellus, and red arrowheads indicate VGLUT-expressing epidermal sensory neurons. (c) Posterior VGAT-expression in the ocellus consists of two cells (orange arrowheads), one exclusively expressing VGAT, and one co-expressing VGAT and VGLUT. Two cells in the anterior exclusively express VGAT (white arrowheads). Nuclei are shown as red spheres. Asterixis indicate overlap of VGAT and VGLUT. (d) Neurotransmitter

predictions color-coded on a schematic diagram of the ocellus photoreceptors. Lines between photoreceptors indicate chemical synaptic connections taken from (Ryan et al., 2016) with red lines indicating projections to the relay neurons. (e) Heat map of neurotransmitter predictions from registration for photoreceptor group I (cells 01–23). Scale assigns color to proportion of iterations predicting VGAT or VGLUT within a particular cell. (f) Confusion matrix of registration of photoreceptor group I cells (cells 01–23). High values (light colors) in the diagonal indicate higher confidence. Abbreviations: dor., dorsal; vent., ventral; ant., anterior; post., posterior; em., eminens cell; RN, relay neuron; AC, antenna cells; pr-AMG RN, photoreceptor ascending motor ganglion relay neuron; prRN, photoreceptor relay neuron; VGAT, vesicular GABA transporter; VGLUT, vesicular glutamate transporter; PR-I, photoreceptor group I (01–23).

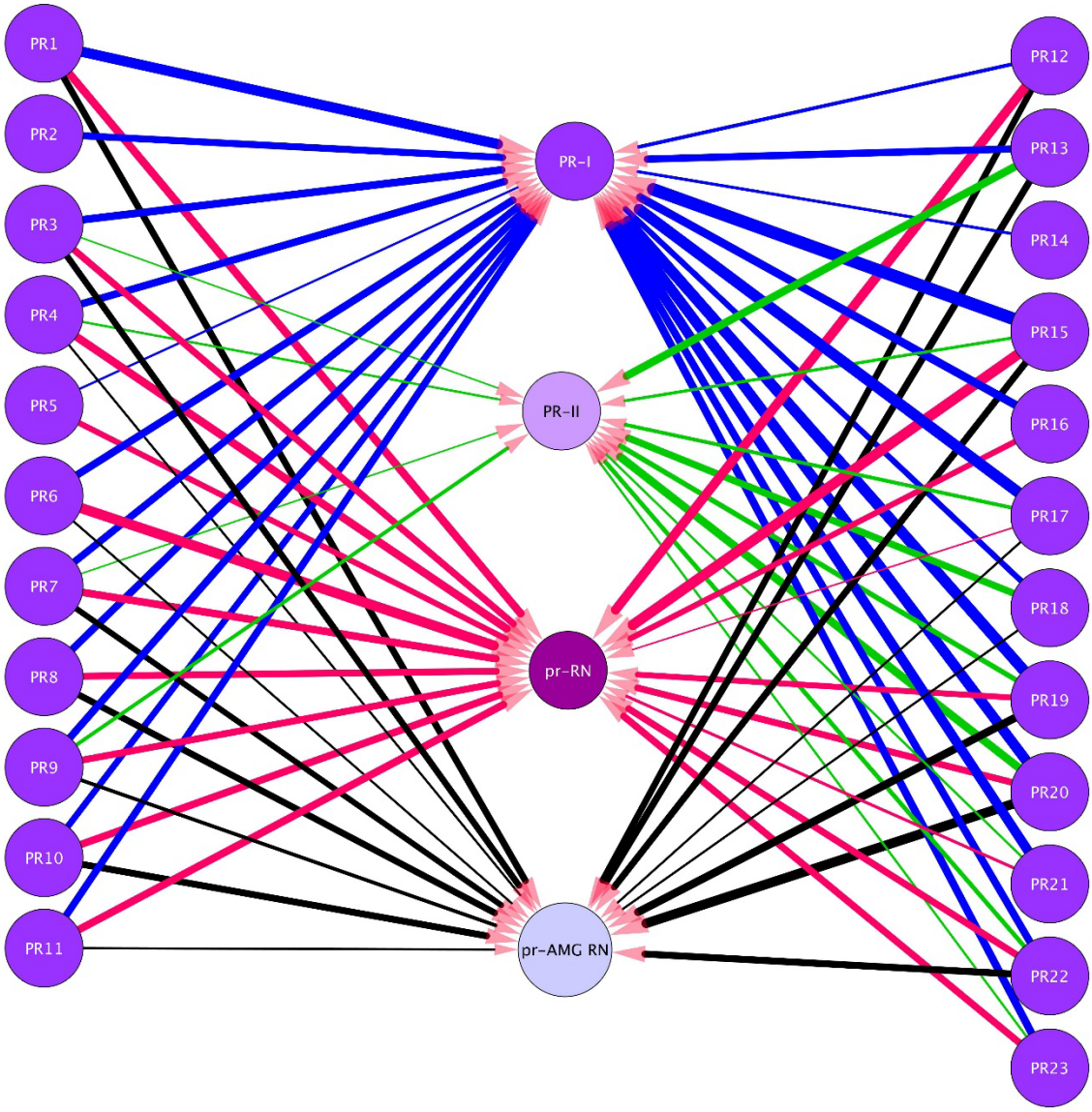

Figure 2.2.1. Neurons in the visuomotor circuit postsynaptic to the Group-I Photoreceptors (PR1-PR23). Lines indicate chemical synapses and their thickness indicates synaptic strength. Data from (Ryan et al., 2016). Abbreviations: PR-I, photoreceptor group I; PR-II, photoreceptor group II; pr-AMG RN, photoreceptor ascending motor ganglion relay neuron; prRN, photoreceptor relay neuron.

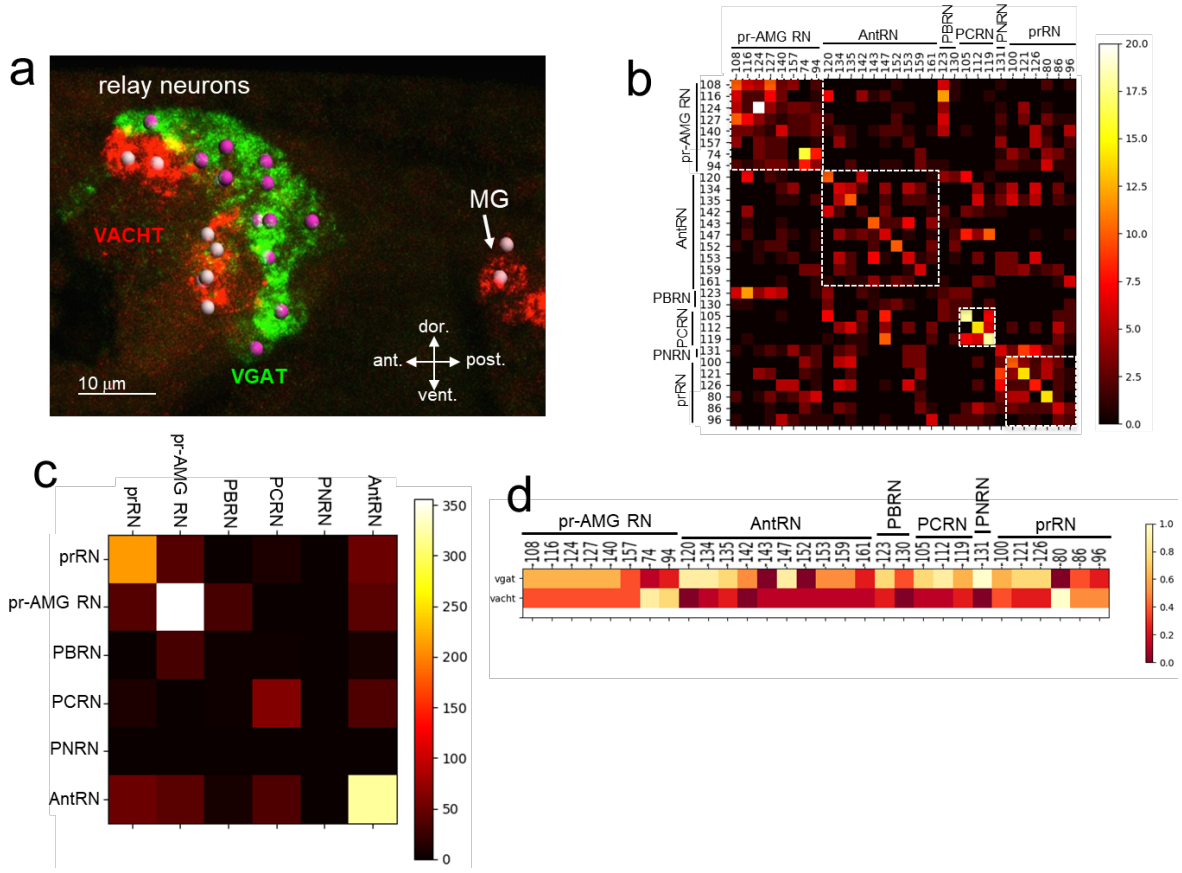

Figure 2.3. Neurotransmitter use in the relay neurons. (a) *In situ* hybridization of VGAT and VACHT to the relay neurons in the brain vesicle. Also visible is the anterior tip of the motor ganglion. Nuclei are shown as spheres. (b) Confusion matrix for relay neuron registration. (c) Confusion matrix for relay neurons grouped by type. (d) Heat map of neurotransmitter predictions from cell registration of relay neurons, with scale showing color by proportion of iterations predicting either VGAT or VACHT. Abbreviations: ant., anterior; post., posterior; dor., dorsal; vent., ventral; MG, motor ganglion; pr-AMG RN, photoreceptor ascending motor ganglion relay neuron; prRN, photoreceptor relay neuron; AntRN, antenna cell relay neuron; PBRN, photoreceptor-bipolar tail neuron relay neuron; PCRN, photoreceptor-coronet relay neuron; PNRN, peripheral relay neuron; VGAT, vesicular GABA transporter; VACHT, vesicular acetylcholine transporter.

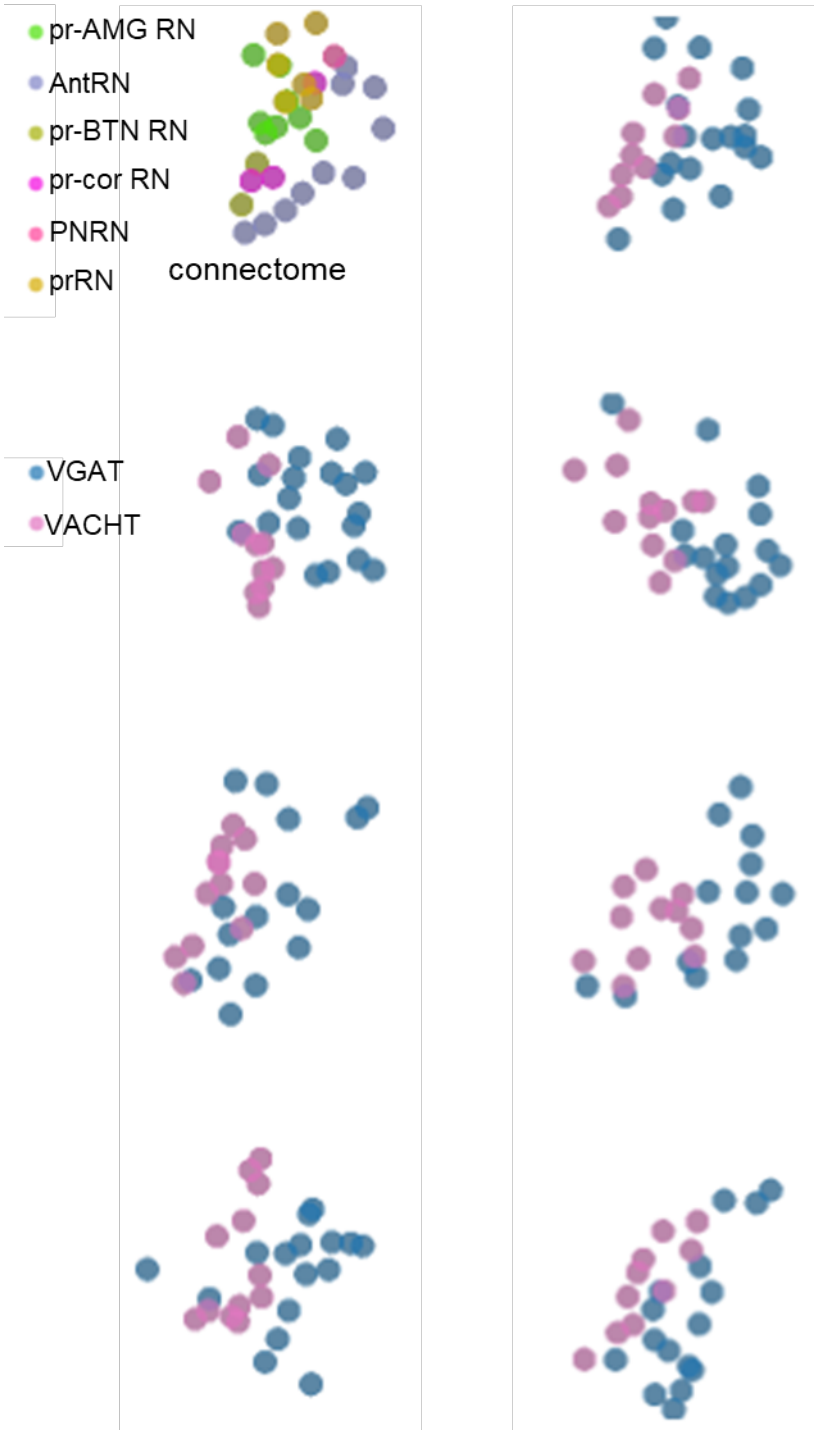

Figure 2.3.1. Relay neuron centroids projected in two dimensions. The top left panel is from the connectome, and the remaining panels show centroids from seven larvae. Anterior is to the left and dorsal is at the top.

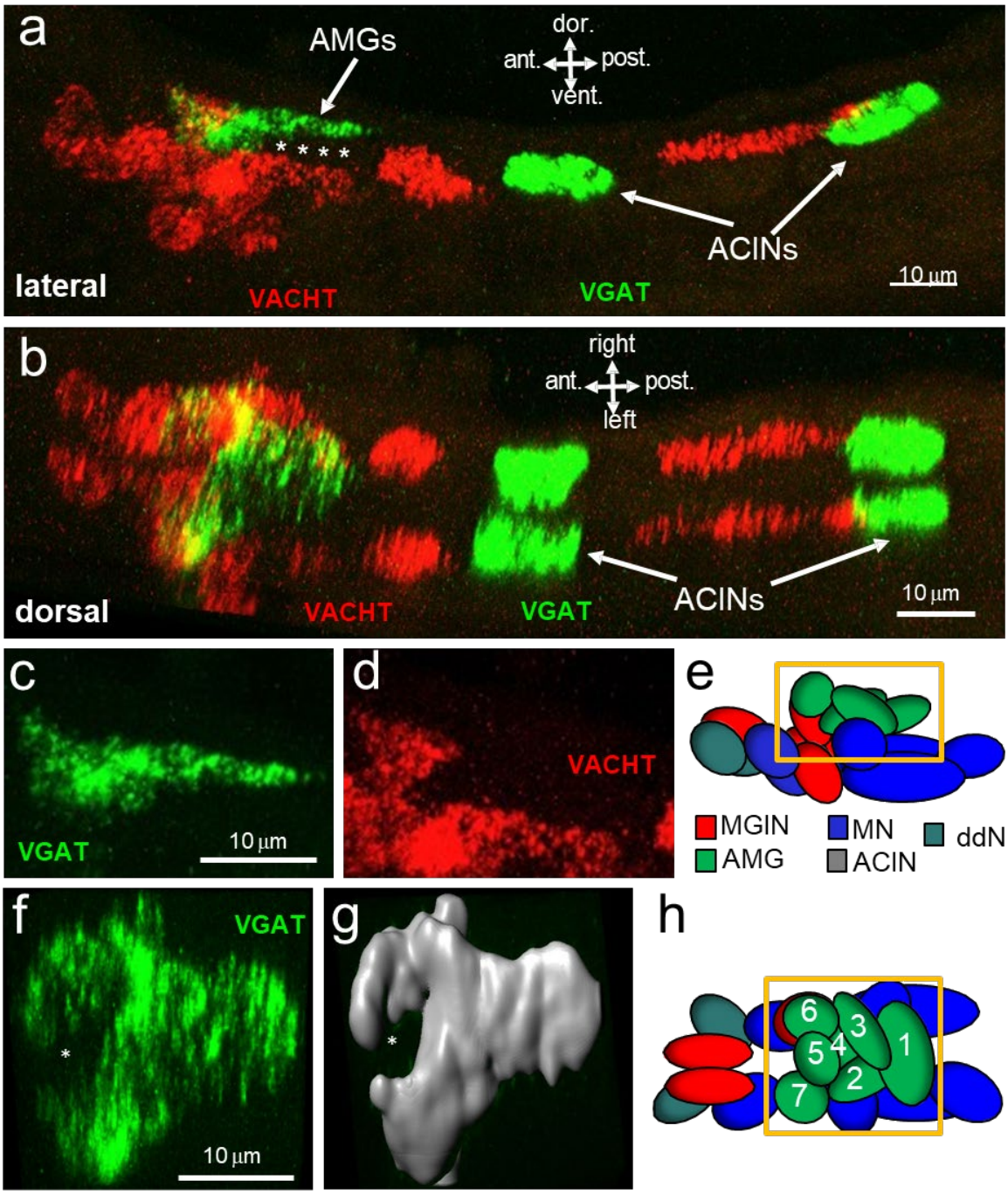

Figure 2.4. Neurotransmitter use in the motor ganglion. (a and b) Expression of VGAT and VACHT by *in situ* hybridization in the motor ganglion, lateral (a) and dorsal (b) views. Asterisks indicate predicted ependymal cells. (c) Lateral view of VGAT expression in the AMGs. (d) shows same view as c, but with VACHT expression. (e) Diagram of neurons in

the motor ganglion [derived from Figure 1 of (Ryan et al., 2017)]. Box indicates approximate positions of panels c and d. Lateral view; anterior is to the left. (f) Dorsal view of VGAT expression in the AMGs. Asterisk indicates central non-VGAT expressing cell. (g) Three-dimensional surface rendering of VGAT expressing cells in the AMGs. (h) Diagram of a dorsal view of the motor ganglion. AMG cells are numbered. Abbreviations: dor., dorsal; vent., ventral; ant., anterior; post., posterior; AMG, ascending motor ganglion neuron; MGIN, motor ganglion interneuron; ddN, descending decussating neurons; ACIN, ascending contralateral inhibitory neurons; MN, motor neuron; VGAT, vesicular GABA transporter; VACHT, vesicular acetylcholine transporter.

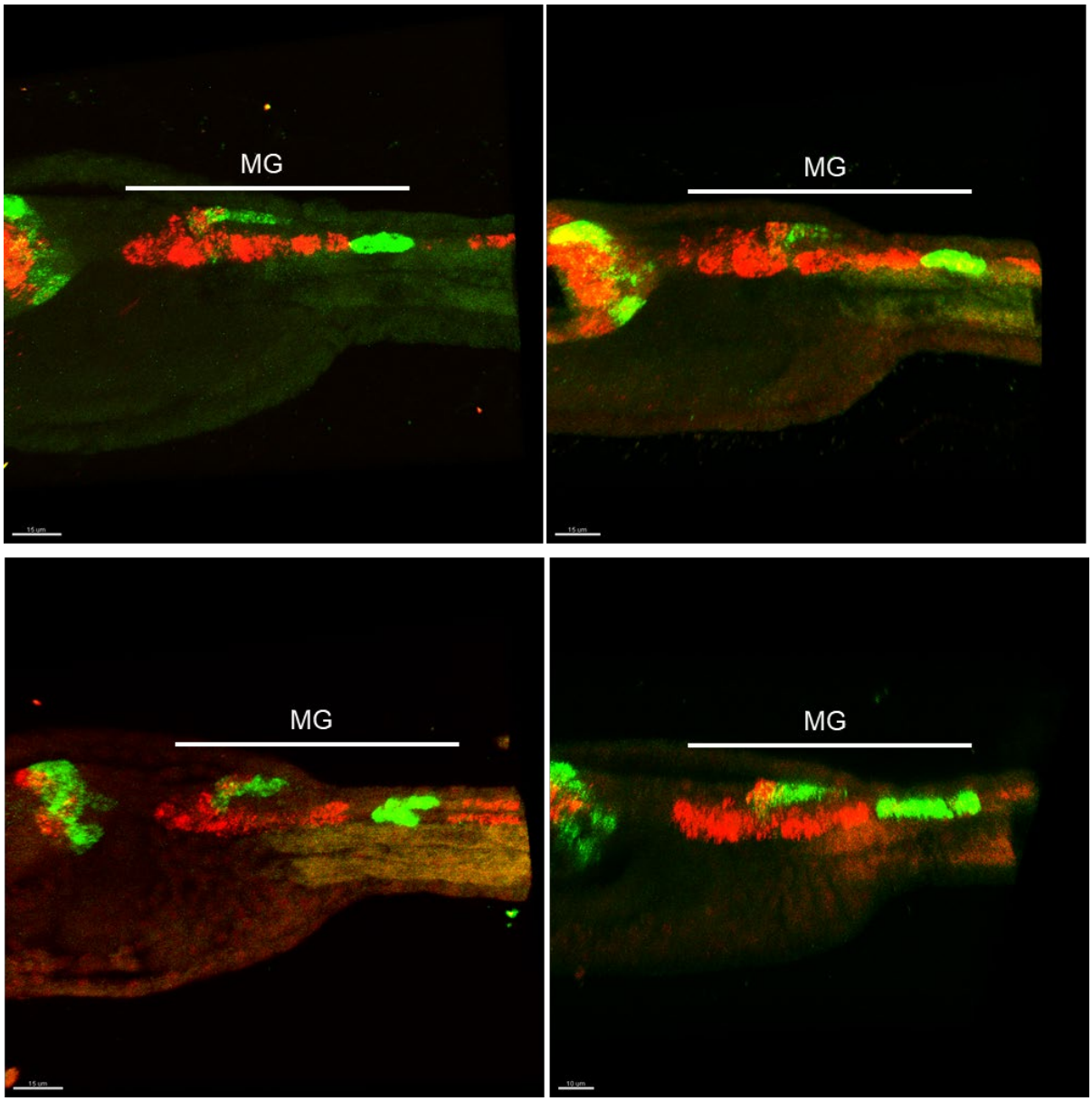

Figure 2.4.1. Representative larvae showing expression pattern for VGAT (green) and VACHT (red) by HCR *in situ*. Top four larvae show the most common expression pattern (also observed in larva shown in Figure 2.4). Larvae 5 and 6 have offset ACINs (arrows). Larva seven is missing both a motor neuron (red asterisk) and an ACIN (green asterisk). Anterior is to the left in all samples.

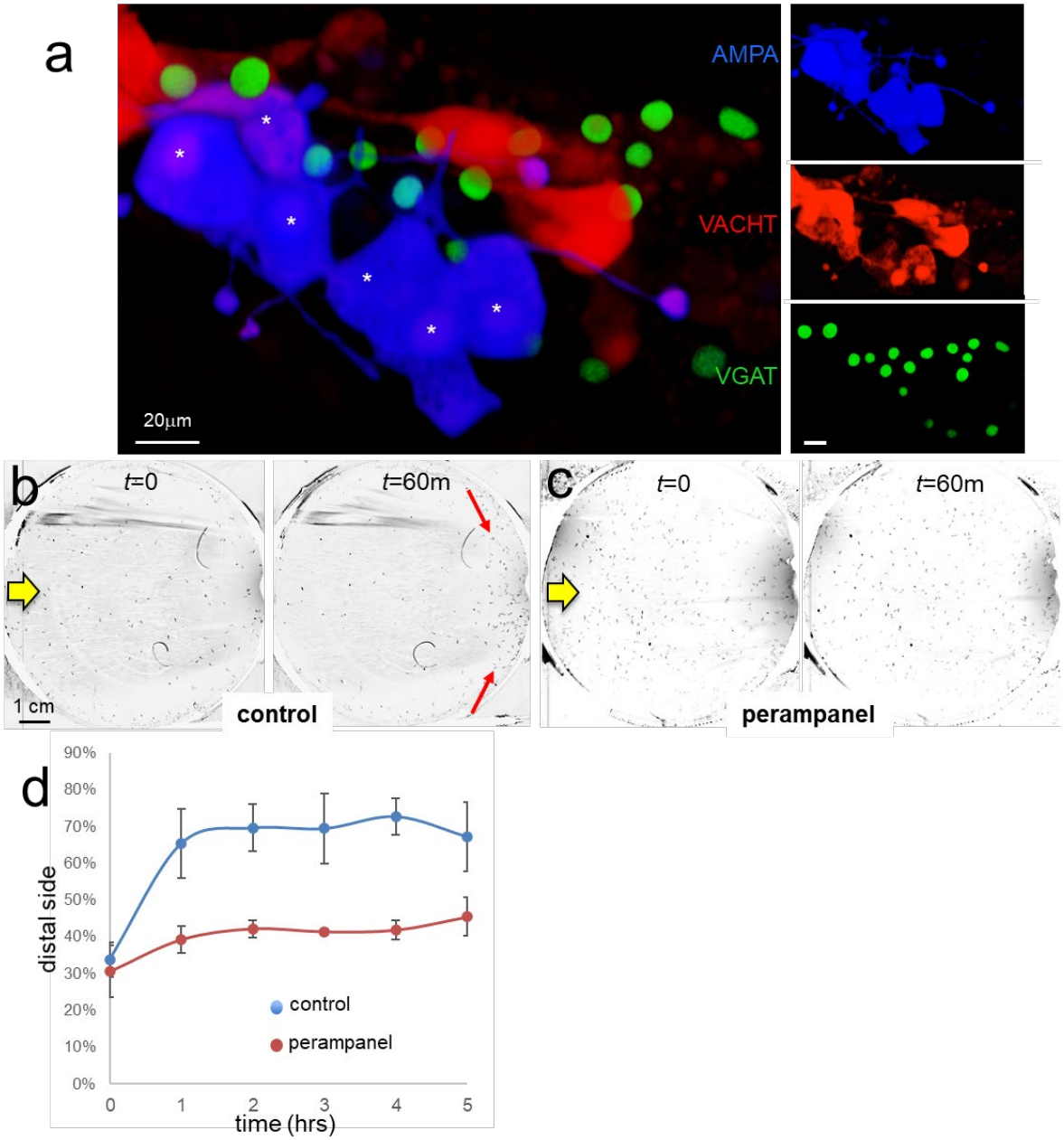

Figure 2.5. AMPA receptors in negative phototaxis. (a) Co-expression of an AMPA-receptor and VACHT expression constructs in the relay neurons (white asterisks). The main panel shows the merge while smaller panels at right show single channels. (b) Negative phototaxis assay in control larvae. Yellow arrow indicates direction of 505 nm light. By 60 min (m) the majority of the larvae have swum to the side of the dish away from the light (red arrow). (c)

Perampanel-treated larvae do not show negative phototaxis. (d) Quantification of negative phototaxis in control and perampanel-treated larvae. Points indicate the averages from three independent assays, ±standard deviation. Y-axis represents the percentage of larvae found on the side away from the light source (distal third). Abbreviations: VGAT, vesicular GABA transporter; VACHT, vesicular acetylcholine transporter.

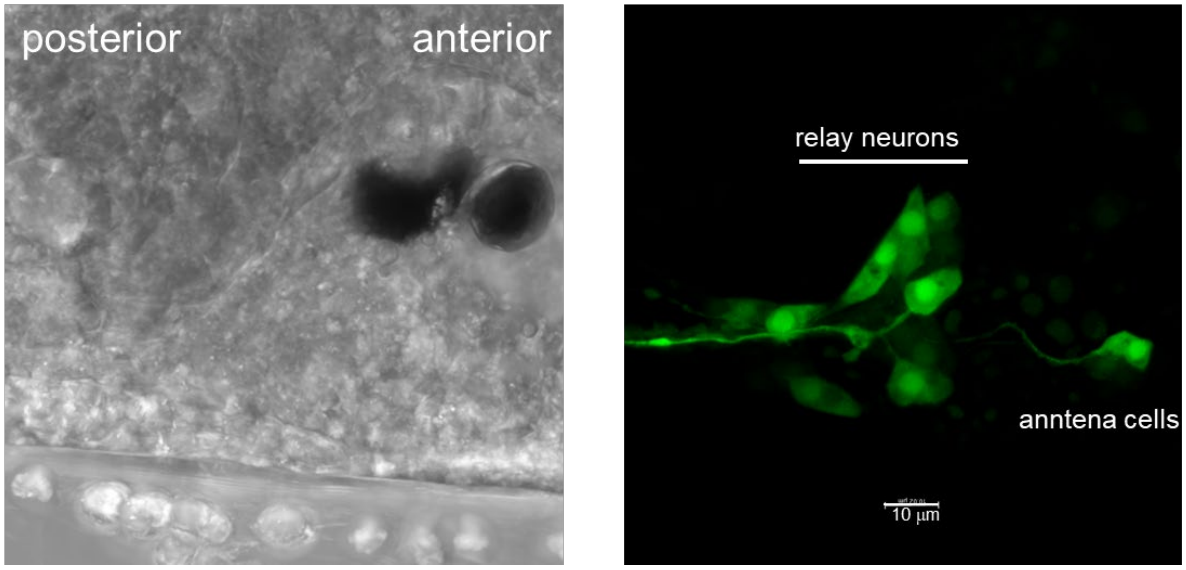

Figure 2.5.1. AMPA-receptor neurons in the *Ciona* brain vesicle identified with an AMPA-receptor promoter construct driving GFP.

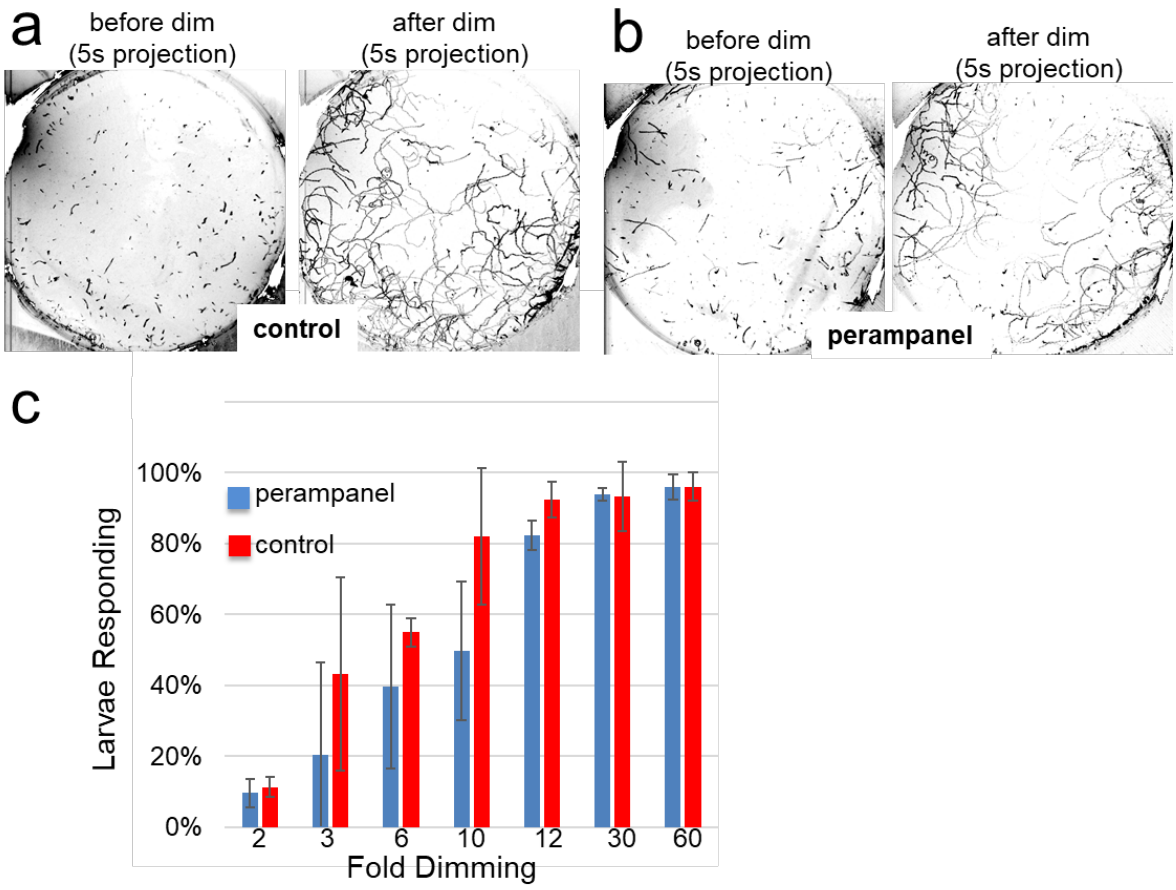

Figure 2.6. Perampanel does not disrupt the light dimming response. (a) Light dimming response in control larvae. Shown are 5 s (s) projections from time-lapse videos in which swims appear as lines. Left panel shows a projection 5 s before dimming, and right panel 5 s after dimming. (b) same as a, but larvae were perampanel-treated. (c) Quantification of light dimming response in control and perampanel treated larvae. Larvae were exposed to dimming of 505 nm light from 2- to 60-fold. Dimming response was scored as percent of larvae responding. Bars show averages of three independent assays ± standard deviation.

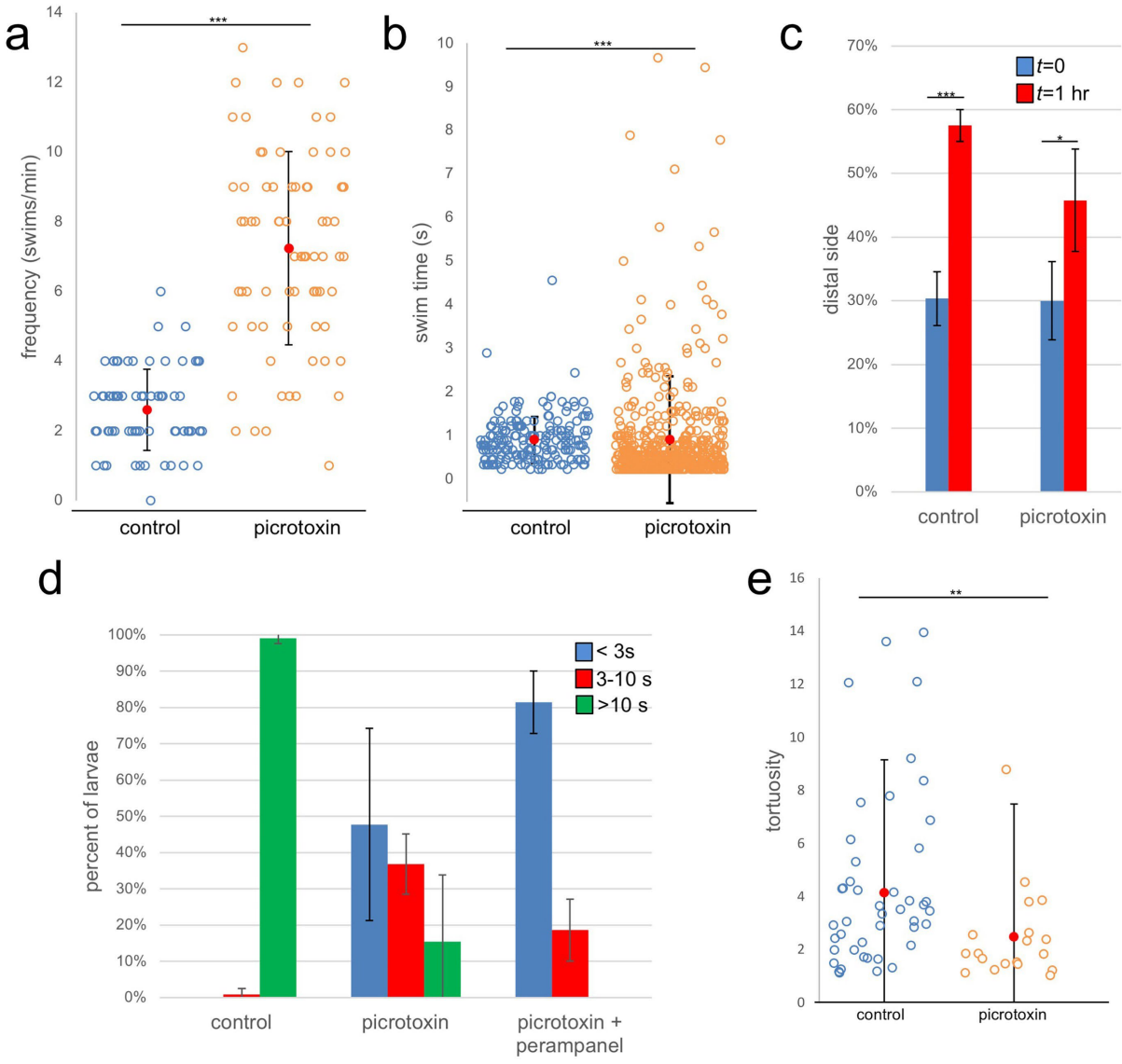

Figure 2.7. Effects of the GABA receptor antagonist picrotoxin on swimming behavior. (a) Frequency of spontaneous swims for control (vehicle only) and picrotoxin-treated larvae in dark conditions (*i.e.*, 700 nm illumination). Each open circle represents a single tracked larva with the number of swim bouts in one minute presented. Also shown are the averages (red circles)±standard deviation. (b) Duration of spontaneous swims in seconds (s). Each circle is one swim bout recorded during a one-minute capture session. (c) Picrotoxin-treated larvae retain negative phototaxis. Bars show the averages of three trails and present the percentage

of larvae in the side of the petri dish opposite the illumination (distal third of dish). (d) Dimming response is diminished in picrotoxin-treated larvae, and further diminished by cotreatment with picrotoxin and perampanel. Shown are the averages of three independent trials (37–99 larvae quantified per trial). Data shows the duration in seconds (s) of swims. (e) Tortuosity of sustained swims (>10 s) for control and picrotoxin-treated larvae. Data is presented as in panel a. *, $p<0.05$; **, $p<0.01$; ***, $p<0.001$.

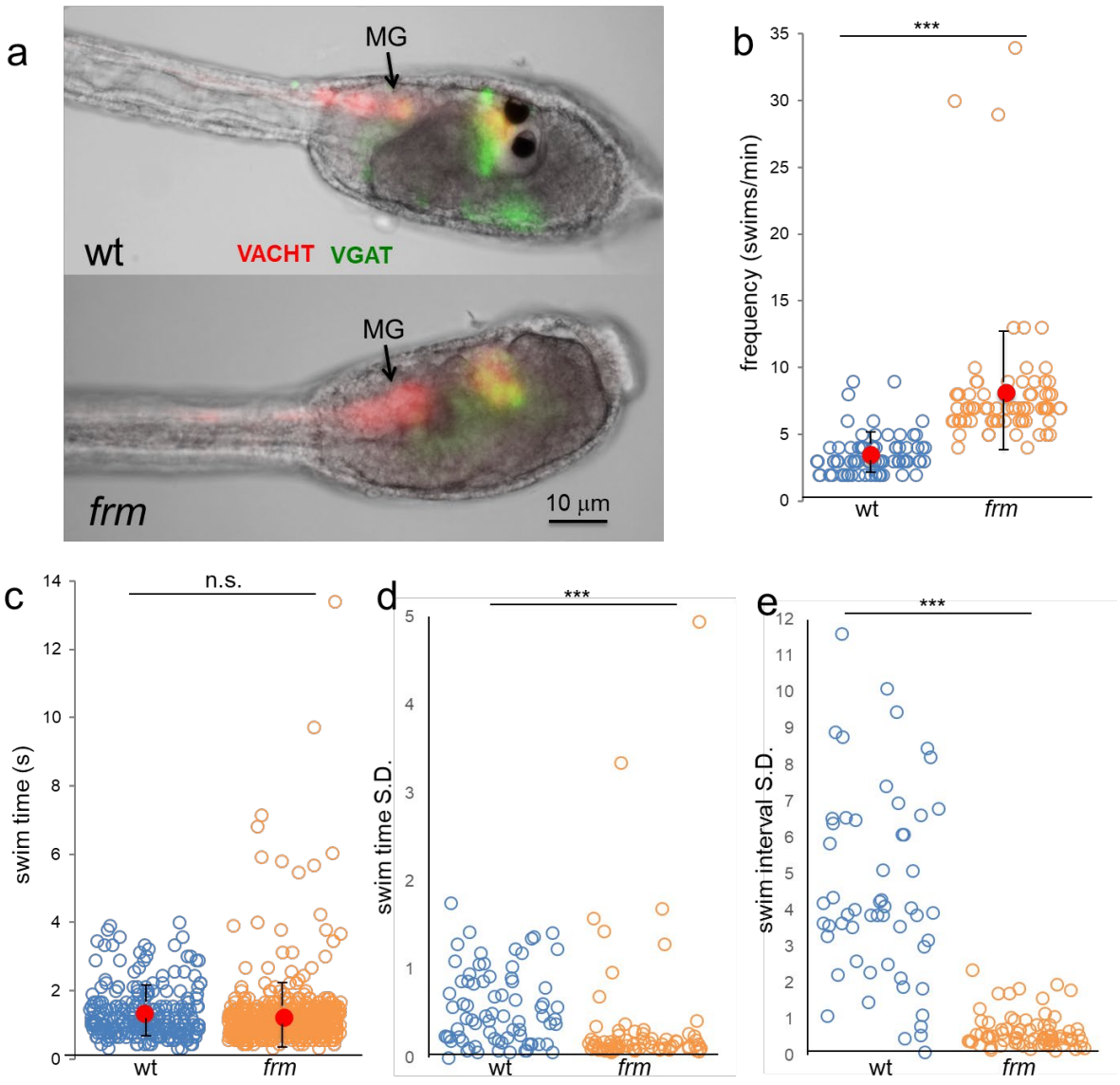

Figure 2.8. Behavior of homozygous *frimousse* (*frm*) larvae. (a) VGAT and VACHT reporter construct expression in wild type (wt) and frm larvae. (b) Frequency of spontaneous swims of wt and frm larvae in dark conditions (i.e., 700 nm illumination). Each open circle represents one tracked larva with the number of swim bouts in one minute presented. Also shown are the averages (red circles) ±standard deviation. (c) Duration of all spontaneous swims in one-minute recording presented in seconds (s) for wt and frm larvae. (d) Standard deviation (S.D.) of the duration of swim bouts over one minute for each individual larva

recorded. (e) S.D. of the interval between swim bouts over one minute for each individual larva recorded. For d and e, larvae with <4 swim bouts were not included in the analysis. ***, $p<0.001$; n.s., not significant.

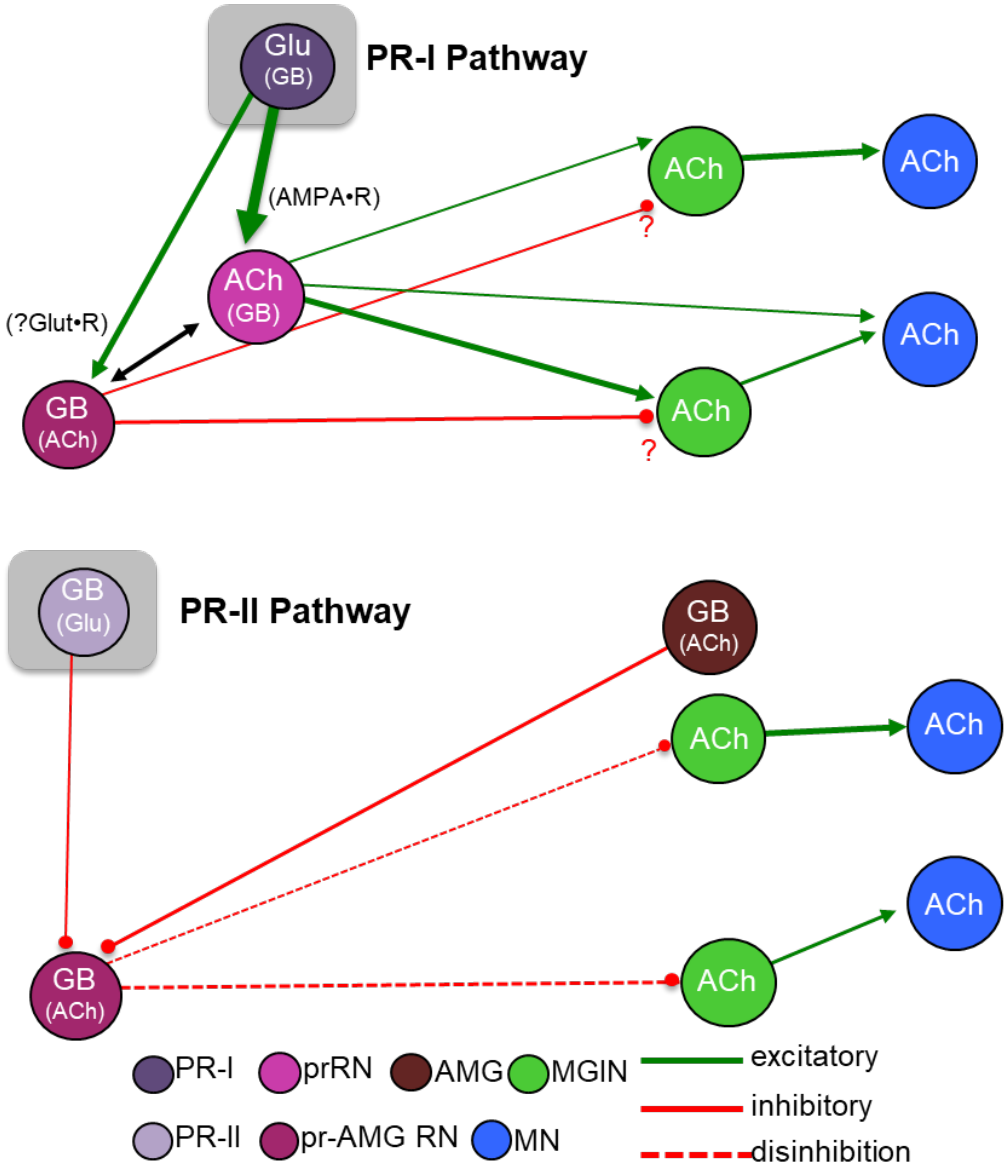

Figure 2.9. Models showing parallel visuomotor pathways for negative phototaxis (top) and light dimming response (bottom). Neurotransmitters in parentheses are thought to play a lesser role in the proposed pathway. Abbreviations: PR-II, photoreceptor group II; PR-I, photoreceptor group I; pr-AMG RN, photoreceptor ascending motor ganglion relay neuron; prRN, photoreceptor relay neuron; MGIN, motor ganglion interneuron; MN, motor neuron; Glu, glutamate; GB, GABA; ACh, acetylcholine. Cell types are color coded according to (Ryan et al., 2016).

3. FOLD CHANGE DETECTION IN VISUAL PROCESSING

Cezar Borba, Matthew J. Kourakis, Shea Schwennicke, Lorena Brasnic, and William C. Smith. 2021. "Fold Change Detection in Visual Processing". *Front. Neural Circuits* 15:705161. https://doi.org/10.3389/fncir.2021.705161

3.1 Abstract

Visual processing transforms the complexities of the visual world into useful information. *Ciona*, an invertebrate chordate and close relative of the vertebrates, has one of the simplest nervous systems known, yet has a range of visuomotor behaviors. This simplicity has facilitated studies linking behavior and neural circuitry. *Ciona* larvae have two distinct visuomotor behaviors – a looming shadow response and negative phototaxis. These are mediated by separate neural circuits that initiate from different clusters of photoreceptors, with both projecting to a CNS structure called the posterior brain vesicle (pBV). We report here that inputs from both circuits are processed to generate fold change detection (FCD) outputs. In FCD, the behavioral response scales with the relative fold change in input, but is invariant to the overall magnitude of the stimulus. Moreover, the two visuomotor behaviors have fundamentally different stimulus/response relationships – indicative of differing circuit strategies, with the looming shadow response showing a power relationship to fold change, while the navigation behavior responds linearly. Pharmacological modulation of the FCD response points to the FCD circuits lying outside of the visual organ (the ocellus), with the pBV being the most likely location. Consistent with these observations, the connectivity and properties of pBV interneurons conform to known FCD circuit motifs, but with different

circuit architectures for the two circuits. The negative phototaxis circuit forms a putative incoherent feedforward loop that involves interconnecting cholinergic and GABAergic interneurons. The looming shadow circuit uses the same cholinergic and GABAergic interneurons, but with different synaptic inputs to create a putative non-linear integral feedback loop. These differing circuit architectures are consistent with the behavioral outputs of the two circuits. Finally, while some reports have highlighted parallels between the pBV and the vertebrate midbrain, suggesting a common origin for the two, others reports have disputed this, suggesting that invertebrate chordates lack a midbrain homolog. The convergence of visual inputs at the pBV, and its putative role in visual processing reported here and in previous publications, lends further support to the proposed common origin of the pBV and the vertebrate midbrain.

3.2 Introduction

The ascidian *Ciona* has served as a valuable model organism both because of its close evolutionary relationship to the vertebrates, and because of its genetic, embryonic, and anatomical simplicity (Lemaire et al., 2008; Satoh, 1994, 2014). Phylogenetically, *Ciona* is a member of the chordate subphylum known as the tunicates. Collectively, the tunicates comprise the closest extant relatives of the vertebrates (Delsuc et al., 2006). The kinship of the tunicates to the vertebrates is evident at all scales – from genomic to anatomical. Particularly striking is the swimming *Ciona* tadpole larva, which highlights both these attributes: vertebrate-like anatomy and simplicity. In common with similarly staged vertebrates, the *Ciona* larva features a notochord running the length of its muscular tail and a dorsal central nervous system (CNS) with a central ventricle. Despite this conserved chordate anatomy, *Ciona* larval organs are composed of very few cells: 40 notochord cells, 36 tail

muscle cells, and ~180 neurons in the CNS (Nicol and Meinertzhagen, 1991; Ryan et al., 2016; Satoh, 1994). The simplicity of the *Ciona* larval CNS has facilitated the generation of a complete synaptic connectome by serial-section electron microscopy (Ryan et al., 2016).

Although small in cell numbers, the *Ciona* larval CNS supports sensory systems that direct a range of complex behaviors. These behaviors include negative gravitaxis, mediated by the otolith organ, mechanosensation, mediated by peripheral touch receptors, and two distinct visuomotor behaviors, mediated by ciliary photoreceptors that cluster into two functional groups in the ocellus organ (Bostwick et al., 2020; Horie et al., 2008a; Kajiwara and Yoshida, 1985; Ryan et al., 2018; Salas et al., 2018; Svane and Young, 1989). Figure 3.1A shows a simplified *Ciona* larva with the visuomotor circuits highlighted. To simplify the diagram, multiple neurons of the same class are grouped together, as are the synaptic connections between them. The first of the two photoreceptor clusters is the PR-I group, which is composed of 23 photoreceptors (Figure 3.1A). All but two of the PR-I photoreceptors are glutamatergic (Figure 3.1B). For the other two PR-I photoreceptors, one is GABAergic, and the other is dual glutamatergic/GABAergic (Kourakis et al., 2019). The PR-I photosensory system mediates negative phototaxis with the aid of an associated pigment cell (*pc* in Figure 3.1) that directionally shades the outer segments of the photoreceptors, allowing larvae to discern the direction of light as they perform casting swims (Salas et al., 2018). The second ocellus photoreceptor cluster, the PR-II group, is composed of seven photoreceptors and is located anterior to the PR-I group [Figure 3.1A; (Horie et al., 2008a)]. The PR-II group does not have an associated pigment cell and evokes swimming in response to changes in ambient light (dimming), most likely as a looming-shadow escape behavior

(Salas et al., 2018). The PR-II group contains a mixture of GABAergic and dual glutamatergic/GABAergic photoreceptors [Figure 3.1B; (Kourakis et al., 2019)].

Both the PR-I and PR-II photoreceptors project directly to relay interneurons in the posterior brain vesicle (pBV) (Figure 3.1A). These relay neurons in turn project primarily to the cholinergic *motor ganglion interneurons* (MGINs) of the motor ganglion (MG) (Figures 3.1A-B). pBV relay neurons with photoreceptor input fall into two main classes. The six *photoreceptor relay neurons* (prRNs) receive input from the PR-I group (Figures 3.1A-B). *In situ* hybridization studies indicate that the prRNs are predominantly cholinergic (Kourakis et al., 2019). The other major class of pBV relay neurons with photoreceptor input are the eight *photoreceptor ascending motor ganglion relay neurons* (pr-AMG RNs; Figures 3.1A-B). The pr-AMG RNs are predominantly GABAergic and receive input from both the PR-I and PR-II groups (Kourakis et al., 2019; Ryan et al., 2016). Thus, the prRNs receive input only from the PR-Is, while the pr-AMG RNs receive input from both photoreceptor groups. Significantly, while both the pr-AMG RNs and the prRNs receive glutamatergic input from the PR-Is, only the cholinergic prRNs express the glutamate AMPA receptor (AMPAR) [Figure 3.1B and (Kourakis et al., 2019)]. Moreover, treatment with the AMPAR antagonist perampanel blocks negative phototaxis while not disrupting the light-dimming response (Kourakis et al., 2019). Thus the minimal circuit for negative phototaxis appears to involve the glutamatergic photoreceptors stimulating the cholinergic prRNs, which then project to the MG to stimulate the cholinergic MGINs. The MGINs then activate the cholinergic motor neurons to evoke swimming (Figures 3.1A-B). The significance of the non-AMPAR glutamatergic input to the pr-AMG RNs is explored in the present study.

The circuit logic for the PR-II mediated dimming response is more complex. GABAergic projections from the PR-IIs are targeted exclusively to the predominantly GABAergic pr-AMG RNs (Figures 3.1B-C). This arrangement led to a disinhibitory model for the light-dimming response (Kourakis et al., 2019). In this model, swimming is actively inhibited by pr-AMG RN input to the MGINs, unless they are themselves inhibited by the GABAergic photoreceptors (Figures 3.1B). Tunicate photoreceptors, like their vertebrate counterparts, are hyperpolarizing (Gorman et al., 1971), and thus dimming is expected to increase their GABA release. Moreover, behavioral analyses with the GABA antagonist picrotoxin, as well as in the mutant *frimousse,* in which the photoreceptors are absent due to a transfating of the anterior brain vesicle (aBV) to epidermis (Hackley et al., 2013), indicate that swimming behavior in the untreated, wild-type larva is constitutively inhibited, consistent with the disinhibition model (Kourakis et al., 2019).

Both *Ciona* visuomotor behaviors are responses to changing illuminations, whether it be decreased ambient illumination for the PR-II circuit, or directional photoreceptor shading in the PR- I circuit. For both visuomotor circuits to function in changing illumination conditions, dynamic visual processing is required. We report here that the *Ciona* larval CNS processes visual inputs to detect fold change (FC) differences. In fold change detection (FCD), the response depends only on the relative change in input, and not on the absolute change (Adler and Alon, 2018). FCD allows a sensory system to give a consistent behavioral response to the same relative change, independent of the ambient conditions, while suppressing noise. Moreover, we present evidence that the circuits for FCD are distinct from the adaptive mechanisms of the photoreceptors, and instead appear to be present in the complex of synaptic connectivity between relay neurons in the pBV. Finally, we note that the

convergence of anatomical, molecular, connectomic, and behavioral data point to the *Ciona* pBV as sharing homology to the vertebrate midbrain, suggesting a common origin of visual processing centers, such as the vertebrate optic tectum (OT) (Knudsen, 2020), and thus this function may predate the split of the tunicates and the vertebrates.

3.3 Materials & Methods

3.3.1 Animals

Wild-type *Ciona robusta* (a.k.a., *Ciona intestinalis* type A) were collected from Santa Barbara Harbor. The animals carrying the mutation *pristine* (Salas et al., 2018) were cultured at the UC Santa Barbara Marine Lab (Veeman et al., 2011). Larvae were obtained by mixing dissected gametes of three adults and then culturing in natural seawater at 18°C. Homozygous *prs* larvae were produced by natural spawning of heterozygous or homozygous *prs* adults. For Figure 3.1C, two stable transgenic lines, vgat > kaede and vacht > CFP [provided by Y. Sasakura], were crossed to yield offspring with labeled GABAergic/glycinergic cells and cholinergic cells, respectively.

3.3.2 Hybridization Chain Reaction (HCR) *in situ* and Immunolabeling

Whole mount fluorescent *in situ* hybridization of embryonic or larval *C. robusta* were performed using the hybridization chain reaction method (v. 3.0, Molecular Instruments; Los Angeles, CA, United States), as previously described (Kourakis et al., 2019). Complementary RNA probe sets were designed to coding regions for the following *Ciona* genes (unique gene identifiers provided in parentheses): *Otx* (NM_001032490.2), *en* (KH2012:KH.C7.431.v1.A.SL1-1), *pax3/7* (KH2012:KH.C10.150.v1.A.SL1-1), *AMPA receptor* (XM_018817034.1), *ADRα2a* (XP_018668148), *VGAT* (NM_001032573.1), and

pitx (KH2012:KH.L153.79.v1.A.SL2-1). In larvae which underwent both *in situ* labeling and immunostaining, the *in situ* hybridization was performed first, followed by the immunolabeling (see below), after a transition from 5X SSCT to PBST.

Larvae for immunostaining were dechorionated at mid-tailbud stage using sodium thioglycolate, as for *in situ* hybridization, so that left-right asymmetric properties of the CNS would not be disrupted (Yoshida and Saiga, 2008). The immunostaining followed previously described procedures for *Ciona* (Newman-Smith et al., 2015). A primary antibody against *C. robusta* arrestin (Horie et al., 2005), raised in rabbit, was used at a dilution of 1:1,000. A secondary antibody, α-rabbit AlexaFluor 594 (Invitrogen; Waltham, MA, United States), was also used at 1:1,000. For vgat > kaede and vacht > CFP larvae, rabbit α-Kaede (MBL; Woburn, MA, United States) and mouse α-GFP (Life Technologies; Carlsbad, CA, United States) antibodies were used at 1:1,000, followed with appropriate AlexaFluor secondaries (Life Technologies), also at 1:1,000 dilution (described above).

Labeled animals (either by *in situ* or immunohistochemistry) were imaged on an Olympus Fluoview 1000 confocal microscope; post-image analysis used Imaris v6.4.0.0 or ImarisViewer v9.5.1 as well as Fiji (ImageJ) v. 2.0.0-rc-69/1.52p. The surface model depicted in Figure 3.1C was generated in Imaris v6.4.0.

3.3.3 Behavioral Assays

All larvae were between 25 and 28 h post fertilization (hpf) (18°C). Larval swimming behaviors were recorded in sea water with 0.1% BSA using 10 cm agarose-coated petri dishes to reduce sticking. Image series were collected using a Hamamatsu Orca-ER camera fitted on a Navitar 7000 macro zoom lens. Programmable 700 and 505 nm LED lamps (Mightex) mounted above the petri dishes were used for dimming response assays as

described previously (Bostwick et al., 2020; Kourakis et al., 2019). The dim response, adaptation, and reaction time movies were recorded at 5, 8.9, and 50 frames per second (fps), respectively. In the standard assay larvae were recorded for 10 s at the initial intensity (lux_0) that was then dimmed (lux_F) to specific values while image capture continued for 2 min. Larvae were allowed to recover for 5 min before being assayed again. All light intensity readings were taken with an Extech Instruments light meter.

3.3.4 Drug Treatments

(*RS*)-AMPA hydrobromide (Tocris; Bristol, United Kingdom) was dissolved in filtered sea water to a stock concentration of 7.5 mM and then diluted to a final concentration of 500 µM. Dexmedetomidine (Tocris) was dissolved in filtered sea water to a stock concentration of 6.75 mM and then diluted to a final concentration of 20 µM. Larvae were incubated with the drug for about 10 min before beginning assays and remained in the drug solution through the entirety of the assay.

3.3.5 Behavioral Quantification

Larvae with short bouts of swimming (<3 s) were not scored (Bostwick et al., 2020; Kourakis et al., 2019). Swim times, speeds, and tortuosities were calculated using the MATLAB script ELIANE (Kourakis et al., 2019). In the test for absolute adaptation (Figure 3.2), to measure the percent of larvae swimming at 1 s time intervals, the ELIANE script was modified to determine if a centroid (i.e., larva) in frame x was in the same position in frame x + 1. The sum of moving centroids was then divided by the total number of centroids. Percent of larvae that responded to dimming stimuli was quantified manually. R-squared values and Bayesian information criterion (BIC) were calculated using the program R. Larvae that had

stuck to the petri dish, or that swam to the edges or into other larvae were not scored. Stuck larvae were defined as those that showed tail beating behavior but did not move during the entire movie.

3.3.6 Statistical Analyses

T-test was used to test significance between percent response (i.e., Figure 3.2D). Wilcoxon rank-sum test was used to pair-wises tests of significance (i.e., wild-type 10-fold vs. wild-type 60-fold). The Kruskal-Wallis test was used for testing significance of whole populations (see *p*-values in Figures 3.2A-C,F). Finally, Friedman's test was used for comparison of larval groups in the fold-change series (i.e., wild-type vs. *prs*, control vs. AMPA).

3.4 Results

3.4.1 Larval Visuomotor Behaviors Display Fold Change Detection

In the first set of experiments, the response of *Ciona* larvae to a light-dimming series from 3-fold (600 lux to 200 lux) to 60- fold (600 lux to 10 lux) was assessed. Several parameters of the dimming-induced swims were measured: the percent of larvae responding to dimming and their reaction time, as well as the duration, speed, and tortuosity of swims. Tortuosity measures the deviation from straight-line swim trajectories (Salas et al., 2018). Movie 1 in (Borba et al., 2021) shows representative responses to 3-, 10-, and 60- fold dims. Of these parameters, induced swim duration showed a positive relation to increased FC (Figure 3.2A), while speed and tortuosity were constant across the series (Figures 3.2B-C; Figure 3.2.1). The percent of larvae responding to dimming also did not track with the FC

series. The percent responding increased initially at the lowest FCs but plateaued at around 10-fold with ~100% of larvae responding (Figure 3.2D).

While the dimming response is an output of the PR- II circuit, the PR-I negative phototaxis circuit depends on larvae detecting changing illumination as they perform casting swims. Although we have reported that *Ciona* larvae are able to successfully navigate in a wide range of ambient lighting conditions (Salas et al., 2018), the phototaxis assay would not permit precise control of the amount of light the PR-I photoreceptors were receiving, making it difficult to assess their responses to FC stimuli. To circumvent this problem, we used the loss-of-pigmentation mutant *pristine* (*prs*) to assess the PR-I photoreceptors, as we have done previously (Kourakis et al., 2019; Salas et al., 2018). In larvae homozygous for *prs*, the PR-I photoreceptors respond to ambient light changes because they are no longer shielded by the pigment cell; in other words, changes in ambient light mimic casting swims (Salas et al., 2018). While both the PR-I and PR-II photoreceptors would be stimulated by dimming in *prs* mutants, there are more PR- I photoreceptors than PR-II (23 versus 7), and the PR-I output appears to predominate (Salas et al., 2018). One way this is evident is that the dimming-evoked swims of *prs* mutants are straight, as are phototaxis swims, rather than highly tortuous, as are dimming-induced swims (Salas et al., 2018). To validate this further, we find that *prs* larvae are more sensitive to dimming at low-light conditions than wild-type larvae (Figure 3.2E), consistent with the behavioral output from *prs* mutants primarily reflecting the output from the PR-I circuit.

When the FC dimming series was performed on *prs* larvae, we again observed a positive relationship of swim time to FC, but with a significantly different shape to the response curve (Figure 3.2F and Figure 3.2.1C; $p = 0.0007$, Friedman's test). Modeling

indicates that a number of different circuit motifs, including the incoherent type-1 feedforward loop (I1FFL) and the non-linear integral feedback loop (NLIFL), can generate FCD outputs (Adler et al., 2017). Moreover, different FCD circuit motifs can generate different response curves (e.g., linear or power), meaning that the response curves can be diagnostic of the underlying circuit architecture (Adler and Alon, 2018). For wild-type *Ciona* larvae, the curve of swim time versus FC was found to best fit a power function, with R^2 = 0.98 (Figure 3.2A). While a log function also fit this curve with R^2 = 0.98, the Bayesian information criterion (BIC, see section "Materials & Methods") for a power relationship had the lower score, indicating a better fit (−13 and 17 for power and log, respectively; R^2 = 0.87 for linear; Figure 3.2.1A). The best fitting model for the *prs* swim time responses was a linear curve having an R^2 value equal to 1.00 (Figure 3.2F). When the *prs* data were fitted to power and log functions, the R^2 values were 0.92 and 0.81, respectively (Figure 3.2.1B). In summary, wild-type and *prs* larvae both show a positive relationship between FC dimming and swim time, although with different response curves, suggesting that different FCD circuits may be responsible.

3.4.2 Validation of FCD Behavior

Fold change detection mechanisms, while incorporating widely observed phenomena such as adaptation and log transformation, have distinct attributes – the most important being scale-invariance (Goentoro et al., 2009; Kamino et al., 2017; Shoval et al., 2010). With scale-invariance the output depends only on the FC, not on the absolute magnitude of the stimulus. We find scale-invariance holds true for the *Ciona* visuomotor response across at least three orders of magnitude. To assess scale-invariance, wild-type and *prs* larvae were exposed to series of 3-, 10-, and 60-fold dims, but from starting intensities of 3000, 300, and 30 lux (e.g.,

the 10-fold dims were 3000 to 300 lux, 300 to 30 lux, and 30 to 3 lux). We observed that the swim time responses of both wild-type and *prs* larvae were not significantly different within a FC, irrespective of the magnitude of illumination, but were significantly increased as FC increased (Figure 3.3A-B and Figure 3.3.1).

Integral to FCD behavior is Weber's law (i.e., the change in stimulus needed to elicit a response is proportional to the absolute value of the original stimulus) (Adler and Alon, 2018). To demonstrate this directly in *Ciona* visuomotor behavior, larvae that were adapted to either 3000 lux or 300 lux were then dimmed by 270 lux (i.e., 2730 or 30 lux, respectively). In those larvae adapted to 3000 lux, we observed no response to the dimming, while in the larvae adapted to 300 lux, we observed vigorous swimming in nearly all larvae (Figure 3.3C). Another property of FCD systems is exact adaptation [i.e., the system returns to the baseline state even when the modulated stimulus persists at the new state (Shoval et al., 2010)]. To investigate this, larvae were initially adapted to 3000 lux, which was then dimmed to 300 lux and held at this level for 2 min. The illumination was then dimmed a second time, to 30 lux [Movie 2 in (Borba et al., 2021)]. Figure 3.3D shows a plot of swimming activity of the larvae as illumination levels change. We observed that the larvae respond robustly to the first 10-fold dim (3000 to 300 lux, yellow boxes in Figure 3.3D), but stop swimming after approximately 30 s. The majority of the larvae were then stationary until the second 10-fold dimming (300 to 30 lux). While a lower percent of larvae responded to the second dim than to the first (87% vs. 64%, Figure 3.3E), no difference in the average swim times of responding larvae was observed (Figure 3.3F). Finally, another predicted property of FCD systems is that the reaction time should be inversely proportional to the FC (Adler and Alon,

2018), which we observed as a power-slope increase in reaction time as the FC decreased (Figure 3.3G and Figure 3.3.1C-D).

3.4.3 Pharmacological Modulation of FCD Circuits

In order to investigate the FCD circuits in the *Ciona* visuomotor system we used pharmacological agents to modulate the response. For the PR-II dimming-response pathway (Figure 3.1B), we had previously shown that the AMPAR antagonist, perampanel, does not disrupt the dimming response but does block PR-I mediated phototaxis (Kourakis et al., 2019). While these results, and the circuit logic of the connectome, indicate that dimming-induced swimming is mediated by GABAergic inhibition of the pr-AMG RNs, there are also extensive synaptic connections between the pr-AMG RNs and the AMPAR-expressing prRNs [Figure 3.1B and (Ryan et al., 2016)]. Synaptic activity between these two classes of interneurons, one primarily excitatory and the other primarily inhibitory, may play a role in FCD. To assess this, we used the AMPAR agonist AMPA, reasoning that while perampanel would simply block glutamatergic input from the PR-Is to the prRNs, and thus should not directly impact the interactions of GABAergic and cholinergic pr-AMG RNs and prRNs (see Figure 3.1B), AMPA, as an agonist, should directly alter the state of the prRNs and could reveal a role in FCD.

We observed that AMPAR is expressed, in addition to the pBV, in the antenna cells and the MG (Figure 3.4A). Significantly, we did not observe expression in the photoreceptors, showing that any observed modulation of FCD behavior was taking place outside of the photoreceptors. Moreover, neither the antenna or MG cells are likely contributors to the FCD processing. Firstly, our previous observations showed that blocking AMPARs with perampanel did not disrupt the antenna cell-mediated gravitaxis at 25 hpf

(Bostwick et al., 2020), and secondly, the MG expression of AMPAR is restricted to the left set of the bilaterally paired MGINs (Kourakis et al., 2021). Thus, while we might expect the AMPA to induce or potentiate swimming (possibly via the MGINs or antenna-cells), we observed no difference in the percentage of control and AMPA-treated (500 μm) larvae responding to a fold-dimming series (Figure 3.4B; Figure 3.4.1). However, a plot of swim time versus FC (Figure 3.4C) shows the slopes of the two curves were significantly different (R^2 of 0.98 for control, and 0.75 for AMPA-treated; $p = 0.0002$, Friedman's test), with AMPA-treated larvae showing much less increase in swim time as the FC series increased. In a second set of experiments in which control and AMPA-treated larvae were assessed against a series of identical FCs but of different magnitudes, the disruption to the FCD mechanism was evident (Figure 3.4D). When the data were grouped according to FC, no significant differences in swim times were found between FCs (Figure 3.4D, left panel), unlike in untreated larvae (Figure 3.3A). However, when the data were grouped by magnitude of the starting illumination, larvae appeared to respond according to the magnitude of illumination, rather than FC (Figure 3.4D, right panel). For example, larvae assessed from a starting illumination of 30 lux had shorter swims than larvae assessed from a starting illumination of 300 lux, independent of the FC. This was true for comparisons across all starting illuminations, with the exception of 300 lux versus 3000 lux.

We assessed a second pharmacological agent, the adrenergic agonist dexmedetomidine, which has previously been shown to modulate the dimming response of *Ciona* (Razy-Krajka et al., 2012), to determine whether it also disrupted FCD. The target of dexmedetomidine, the α2 adrenoreceptor (ADRα2a), was shown with use of a *cis*-regulatory element reporter construct to be expressed in VACHT-positive neurons of the pBV. By *in*

situ hybridization analysis, we confirmed expression in the pBV (Figure 3.4E, left panel), as well as two groups of the neurons in the MG that we have tentatively identified as ddNs and MGINs based on their locations to each other and the AMG cells. We also observed expression in the photoreceptors of the ocellus (Figure 3.4E, right panel). The strongest ADRα2a expression was in the posterior, non-VGAT expressing, photoreceptors, which corresponds to the PR-I group (Kourakis et al., 2019). Consistent with the previous report (Razy-Krajka et al., 2012), we observed that dexmedetomidine treatment decreased swim times in response to dimming for both wild-type (Figure 3.4.2) and *prs* larvae (Figure 3.4F; and Figure 3.4.3). The dimming response in wild-type larvae was greatly reduced by dexmedetomidine, and a response to different FC dimmings was most evident at the highest magnitude illumination level (3000 lux; Figures 3.4.2B-C). By contrast, dexmedetomidine-treated *prs* larvae, despite being significantly inhibited by dexmedetomidine, showed more robust responses at all illumination levels for 10- and 60-fold dimming (Figure 3.4G). At three-fold dimming too few *prs* larvae responded for the analysis (Figure 3.4.3).

In summary, results with dexmedetomidine-treated larvae contrast with those from AMPA-treated larvae. AMPA treatment disrupts FCD, but not the ability of the larvae to respond to dimming. Moreover, AMPA-treated larvae appear to respond to the magnitude of the illumination, not the FC. By contrast dexmedetomidine treatment results in an overall decrease in responsivity to dimming, but we still see evidence of FCD. These results indicate that the FCD element of the *Ciona* visual response circuits can be separated from the detection of illumination. In addition, the fact that the FCD element can be disrupted by AMPA indicates that the synaptic activity of the circuit is essential for FCD, which contrasts

with other characterized FCD mechanisms, in which signal transduction pathways appear sufficient to account for FCD (Adler and Alon, 2018).

3.4.4 Is the pBV a Homolog of the Vertebrate Midbrain?

The pBV is the primary recipient of projections from the ocellus, otolith, and coronet cells, and a subset of peripheral neurons (Ryan et al., 2016). Relay neurons within the pBV then project posteriorly through the neck to the MG. No other region of the *Ciona* CNS has this convergence of sensory inputs and descending interneuron projections. Results presented here, as well as published studies (Bostwick et al., 2020), point to the pBV as a sensory processing and integrating center. Thus, in many ways, the function of the pBV resembles that of the vertebrate midbrain visual processing centers, including the optic tectum (Knudsen, 2020). The resemblance of the pBV to the vertebrate midbrain extends to the *Ciona* CNS anatomy as well. In particular, the pBV is located immediately anterior to the neck region which, based on gene expression and the fact that it forms a constriction in the CNS, is thought to have homology to the vertebrate midbrain-hindbrain junction (Ikuta and Saiga, 2007). Despite these anatomical similarities, it has been widely speculated that tunicates either do not have or have lost a midbrain homolog. These reports are based on the expression patterns of several genes that do not match the expression of their vertebrate orthologs. For example, the gene DMBX, which plays an essential role in vertebrate midbrain development, is not expressed anterior to the MG in *Ciona* (Ikuta and Saiga, 2007; Takahashi and Holland, 2004). In addition, the tunicate *Oikopleura dioica* (Class Larvacea) does not express the genes *engrailed* or *pax2/5/8* anterior to its hindbrain, suggesting that larvaceans lack a midbrain (Cañestro et al., 2005). However, these studies were limited to a few genes, and were performed before the connectivity of the pBV was made apparent by the

publication of the connectome. Moreover, as presented below, a wider view of neural genes shows extensive gene expression conservation between the pBV and the vertebrate midbrain.

The *Ciona* BV is divided into distinct anterior and posterior domains that derive from invariant cell lineages arising at the 8-cell stage, with the anterior BV (aBV) descending from the a-lineage, and the pBV from the A-lineage (Figure 3.5A, red and blue cell centroids, respectively) (Nicol and Meinertzhagen, 1988; Nishida, 1987). Moreover, the distribution of neuron types is sharply demarcated by this boundary, with the relay neurons, which uniquely project from the BV to the MG, being found only in the pBV. The relay neurons are themselves segregated within the pBV, with those receiving photoreceptor input clustered anteriorly (Figure 3.5B). The gene *Otx*, which is expressed in the forebrain and midbrain of vertebrates (Boyl et al., 2001), is expressed in *Ciona* in both the aBV and pBV (Hudson et al., 2003; Ikuta and Saiga, 2007; Imai et al., 2002), while a number of the vertebrate forebrain markers are expressed only in the aBV lineage. This includes the genes *Dmrt1* (Kikkawa et al., 2013; Tresser et al., 2010; Wagner and Levine, 2012), as well as *Lhx5*, *Six3*, and *Gsx2* (Esposito et al., 2017; Mazet et al., 2005; Moret et al., 2005b; Reeves et al., 2017), all of which play essential roles in vertebrate forebrain development (Kirkeby et al., 2012; Lagutin, 2003; Peng, 2006; Toresson et al., 2000). While *Gsx2* is also expressed in the pBV, this is only in later stages of development (tailbud stages). Additional vertebrate forebrain markers expressed exclusively in the aBV lineage include *Lhx2/9*, *Bsx* (or *Bsh*) and *Arx* (or *Aristaless*) (Cao et al., 2019). In vertebrates these genes are reported to play essential roles in cortex development (Marsh et al., 2016; Roy et al., 2014; Schredelseker et al., 2020; Shetty et al., 2013).

By contrast, the pBV expresses a number of genes associated with the vertebrate midbrain. This includes the A-lineage specific marker *FoxB1* (or *Ci-FoxB*) (Moret et al., 2005b; Oonuma et al., 2016), which in vertebrates plays a role in midbrain development (Wehr et al., 1997). The development of the vertebrate optic tectum, a midbrain structure, requires the co-expression of *Pax3*, *Pax7*, *Otx2*, and *En* (Matsunaga et al., 2001; Thompson et al., 2008). The *Ciona engrailed* ortholog is expressed in two domains embryologically: posteriorly in the MG and anteriorly in the pBV (Ikuta and Saiga, 2007; Imai et al., 2002). We observed overlapping expression of *Pax3/7*, *En*, and *Otx2* in the developing pBV of early tailbud embryos (Figure 3.5C, asterisk). Finally, *Pitx* has a well-defined role in vertebrate midbrain development (Luk et al., 2013). We observed *Ciona Pitx* expression at early tailbud stage in a posterior domain that overlaps with pBV *engrailed* expression (Figure 3.5D, asterisk), as well as in an anterior domain that appears to correspond to the aBV expression reported in older embryos and larvae (Christiaen et al., 2002). In addition, diffuse epidermal labeling was observed, as reported previously (Boorman and Shimeld, 2002). The pBV is bounded posteriorly by expression of *Pax2/5/8* in the neck cells, indicating shared homology with the vertebrate MHB [(Ikuta and Saiga, 2007); Figure 3.5A].

These expression pattern results show that the BV has distinct anterior and posterior expression domains, with the anterior domain expressing genes known to be expressed in the developing vertebrate forebrain, and the posterior domain expressing genes associated with the developing vertebrate midbrain. These observations do not agree with previous reports that suggest the entire BV is homologous to the vertebrate forebrain (and that a midbrain homolog is absent). Thus, the convergence of gene expression, anatomical, connectivity and functional data all point to the pBV as sharing a common origin with the vertebrate midbrain.

3.5 Discussion

The behavioral studies presented here demonstrate that *Ciona* larvae transform visual input to detect FCs. The utility of this behavior is clear: in negative phototaxis, larvae discern the direction of light via casting swims, and it is the change in illumination falling on the PR-Is as larvae turn away from the light that is the cue to swim. FCD ensures that the casting mechanism functions in the wide range of ambient light conditions that larvae are likely to encounter, and that the response is invariant to the scale of the input. The function of FCD to the dimming response is similar. In the absence of FCD, the change in illumination caused by the same looming object that appeared to be a threat in one ambient light condition, might not be in another. FCD ensures that the response varies as a function of the relative shading caused by the looming object. Comparison of the response curves of wild-type and *prs* larvae to a FC series indicates that different mechanisms are operable in the two pathways, although it is not known if these stimulus-response relationships are each better suited for the type of behavior being mediated.

A number of cellular signaling systems have been shown to give FCD responses to extracellular cues, including those in bacterial chemotaxis and growth factor signaling in mammalian cells and embryos (Adler and Alon, 2018; Goentoro et al., 2009; Lyashenko et al., 2020; Shoval et al., 2010). Modeling has identified several classes of biological circuits that can generate FCD responses (Adler et al., 2017; Goentoro et al., 2009; Hironaka and Morishita, 2014), although in many examples of FCD the biological circuits remain to be determined. For the FCD responses described here, the combination of the connectomic, behavioral and pharmacological data point to candidate FCD circuits. In particular, the results with the drug AMPA, in which the larvae remain responsive but no longer show FCD,

indicate that neural circuits, and not only intracellular signal transduction pathways can generate FCD responses. Nevertheless, the *Ciona* photoreceptors themselves, because of their presumed adaptive properties, almost certainly play a role in processing the visual inputs by extending the dynamic range. Vertebrate photoreceptors, in particular cones, have properties that might by themselves generate a FCD output, including adaptation and adherence to Weber's Law (Burkhardt, 1994). However, to our knowledge, FCD by vertebrate photoreceptor phototransduction machinery has not been directly assessed, and modeling suggests that adaptation and adherence to Weber's law alone are not sufficient to give FCD (Shoval et al., 2010). Moreover, much of the adaptive properties of the vertebrate visual system arise not only from the transduction mechanism inherent to the photoreceptors, but also from the neural circuitry in the vertebrate retina (Dunn et al., 2007).

While the presence of AMPA receptors in both the pBV and the MG complicates the identification of candidate FCD circuits, the properties of the pBV make it a more likely candidate for containing the FCD circuits. The *Ciona* connectome shows that the pBV is unique among the brain regions in receiving direct input from several sensory systems including the photoresponsive ocellus, the gravity sensitive otolith, the dopaminergic coronet cells, and a subset of the peripheral sensory neurons (Ryan et al., 2016, 2018). Relay neurons from the pBV then project to a common set of six secondary cholinergic interneurons (MGINs) and ten motor neurons in the MG (Figure 3.1A). This circuit architecture of converging sensory inputs implicates the pBV as a site of sensory integration and processing. For example, *Ciona* larvae integrate visual and gravitactic inputs into a single behavior consisting of upward swimming in response to light dimming (Bostwick et al., 2020). The projections from these two sensory systems converge and are interconnected at the pBV.

While the two photoreceptor pathways in *Ciona* appear to operate in parallel, they too converge at the pBV, but with different circuit architectures (Figure 3.1) and logic (Kourakis et al., 2019). Significantly, a closer examination of the interneurons in the pBV which receive input from the two photoreceptor systems suggests circuits that can account for the different stimulus-response curves (Figure 3.2).

Figure 3.6A shows the full PR-I and PR-II visuomotor circuits, as given by the *Ciona* connectome (Ryan et al., 2016) with superimposed putative neurotransmitter types, as deduced by *in situ* hybridization (Kourakis et al., 2019). When the PR-I and PR-II circuits are simplified by combining cell types and synaptic connections, two plausible FCD circuits are evident, with prominent roles played by the pBV relay neurons (Figure 3.6B). The PR-I circuit contains a putative incoherent feedforward loop (IFFL), while the PR-II circuit contains a putative non-linear integral feedback loop (NLIFL). Experimental and modeling studies show that these two circuits will give very different response curves to a FC series (Adler and Alon, 2018). The NLIFL gives a power relationship, as we observed for wild-type larvae (Figure 3.2A). The proposed PR-I IFFL circuit differs from the widely studied type-1 IFFL in having an additional excitatory interaction from the output (y) to the modulator (m) (top, Figure 3.6B). While computer modeling of circuit motifs indicates that this motif should give FCD (Adler et al., 2017), the relationship between FC and output has not been modeled. Nevertheless, the presence of two different FCD motifs in the PR-I and PR-II circuits is consistent with the observed differences in behavioral responses to the FC series. We note that in the two proposed FCD circuits in Figure 3.6B, the RN types exchange roles as output (y) and modulator, suggesting an economy of neuron use.

The proposed NLIFL motif in the PR-II circuit, being disinhibitory, has circuit components that are switched compared to conventional NLIFL motif (bottom, Figure 3.6B). We hypothesize that this circuit would have the same sensory processing function because the key elements are all present, albeit with opposite polarity. In other words, in disinhibitory circuits the inhibition of the output evokes the response (i.e., swimming). In a conventional circuit the modulator inhibits the output. However, in the disinhibitory circuit the modulator activates the output. The result of both is to decrease the response, and the decrease is proportional to the input, which is a key feature of FCD circuits. Consistent with the AMPAR-expressing cholinergic prRNs acting as the modulator in the disinhibitory circuit, addition of AMPA disrupts FCD (Figure 3.4).

Unlike in the pBV, analysis of the MG circuitry did not reveal plausible FCD circuits. The MG is dominated by excitatory cholinergic interneurons and motor neurons, while inhibitory neurons, which would be an essential modulatory element of any likely FCD circuit, are limited to the GABAergic AMG neurons, which receive no descending input, directly or indirectly, from the photoreceptors or the BV, and the glycinergic decussating ACINs, which likely play a role in the central pattern generator, not visual processing (Kourakis et al., 2019; Nishino et al., 2010; Ryan et al., 2016). In addition, the PR-I and PR-II circuits project from the pBV to a common set of MG interneurons, making it unlikely that this brain region would be responsible for the different FC response curves for the PR-I and PR-II circuits.

The homology of the various anterior-to-posterior domains of the tunicate larval CNS to those of their vertebrate counterparts is still a matter of discussion [reviewed in (Hudson, 2016)]. Of particular controversy is the presence of a midbrain homolog, with gene-

expression data used both to argue for (Imai et al., 2002; Wada et al., 1998), and against (Cañestro et al., 2005; Ikuta and Saiga, 2007) homology. It has been proposed that the midbrain is a vertebrate invention (Takahashi and Holland, 2004), although evidence for a midbrain in amphioxus argues against this (Holland, 2015; Lacalli, 2018). Nonetheless, the "neck" region of the *Ciona* CNS has apparent conserved gene expression, and thus presumed homology, to the vertebrate midbrain/hindbrain junction (Imai et al., 2009). However, the Otx-expressing CNS region anterior to the neck (called variously the *sensory vesicle* or the *brain vesicle*), has been equated with either the vertebrate forebrain in its entirely, or with separate forebrain and midbrain domains (Imai et al., 2002, 2009; Wada et al., 1998). Figure 3.5 shows nine orthologs of vertebrate forebrain markers that are expressed in the aBV, but not in the pBV. This is compelling evidence that the entire brain vesicle does not have homology to the forebrain. Thus, the pBV is sandwiched between a region anterior to it that expresses forebrain markers, and a region posterior to it that expresses midbrain/hindbrain junction markers. Figure 3.5 also presents five genes that are expressed in both the vertebrate midbrain and in the posterior brain vesicle of *Ciona*. The *Ciona* connectome provides added perspective to this issue: the pBV, which is distinct from the aBV in a number of ways, including its cell lineage (Cole and Meinertzhagen, 2004), is the principal target of input from the visual system, as is the midbrain, particularly in lower vertebrates (Knudsen, 2020). Like the vertebrate midbrain, the pBV also receives input from other sensory systems, including, in the case of *Ciona*, the otolith and the peripheral nervous system. Moreover, the vertebrate midbrain is an important site of multisensory integration, and recent work from our laboratory has identified the pBV as a likely site for integration of visual and gravitaxis sensory inputs (Bostwick et al., 2020). The results presented here identifying the pBV as a

likely site of FCD in visual processing, further supports the connections between the pBV and the midbrain. The combination of anatomical, gene expression, and connectivity data all point to a common origin for the pBV and the vertebrate midbrain. The alternative, that these similarities are the product of convergence, would appear to be much more unlikely, particularly in light of amphioxus data which show that cephalochordates, the most basal chordate subphylum, and whose divergence preceded the tunicate/vertebrate split, have conserved midbrain visual processing centers (Lacalli, 2006; Suzuki et al., 2015; Takahashi and Holland, 2004). Because cephalochordates, such as amphioxus, are basal to both tunicates and vertebrates, the convergence theory would have to postulate that the apparent homologies observed in both tunicates and cephalochordates arose independently, or that tunicates lost the midbrain homolog, and then independently evolved a brain region with similar gene expression, connectivity and anatomical location to those in vertebrates and cephalochordates.

3.5.1 Acknowledgements

We thank Takehiro Kusakabe for the anti-Arrestin antibody.

3.6 Figures

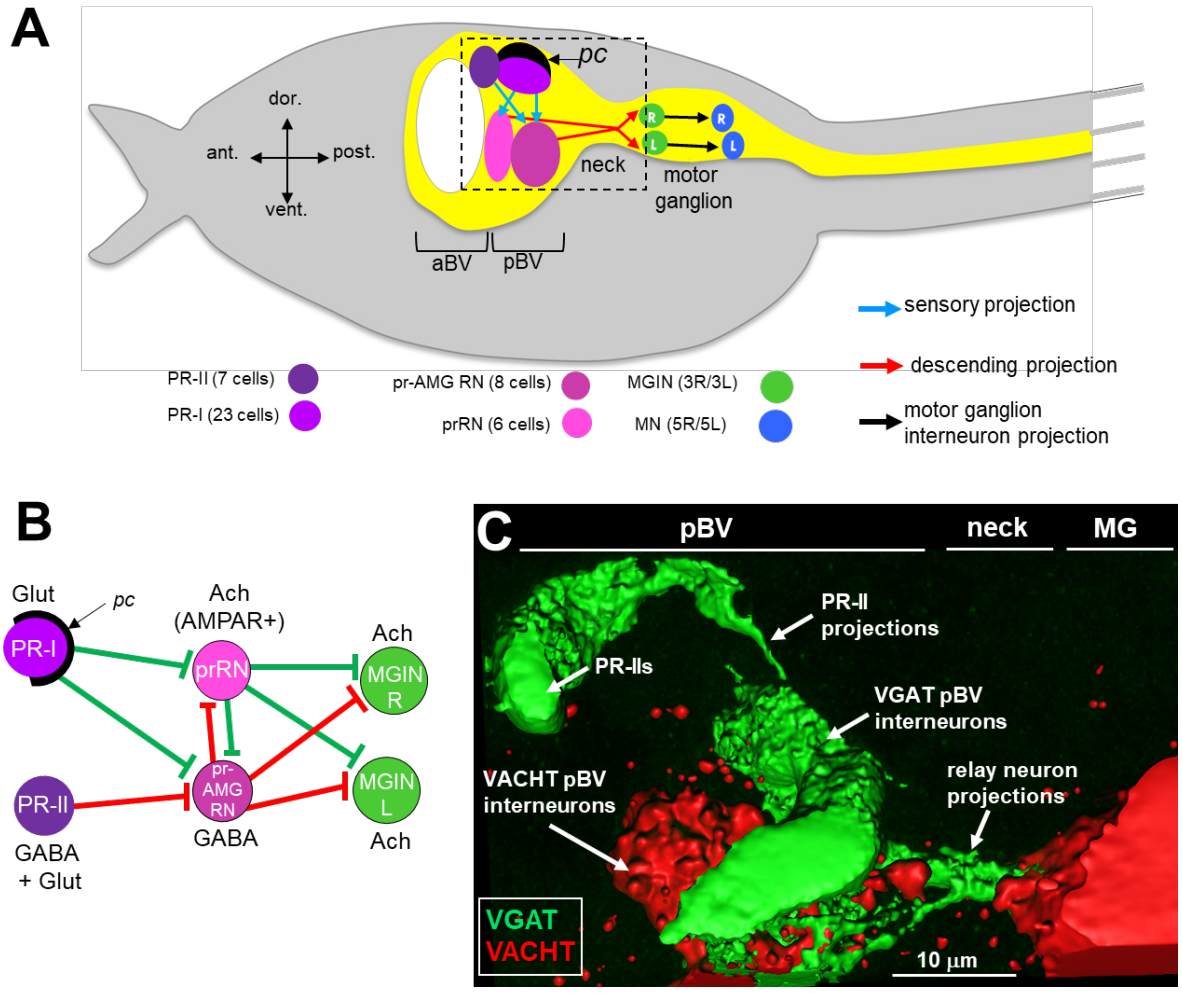

Figure 3.1. Minimal visual circuitry and anatomy. (A) Cartoon of a *Ciona* larva, with emphasis on the anterior (only a small portion of tail is shown at right). Highlighted in the CNS (yellow) are the minimal visuomotor pathways. Cell classes are color coded according to (Ryan and Meinertzhagen, 2019), and the number of cells in each class are indicated in parentheses. (B) Minimal visuomotor circuits. Green lines indicate putative excitatory and red lines putative inhibitory synapses. (C) GABAergic PR-II photoreceptors project to GABAergic relay neurons in the pBV. View corresponds approximately to the dashed box in panel (A). pc, pigment cell; aBV, anterior brain vesicle; pBV, posterior brain vesicle; PR,

photoreceptor; pr-AMG RN, photoreceptor ascending motor ganglion relay neurons; prRN, photoreceptor relay neurons; MGIN, motor ganglion interneurons; MN, motor neurons; L, left; R, right; Glut, glutamate; Ach, acetylcholine; AMPAR, AMPA receptor; MG, motor ganglion; VGAT, Vesicular GABA transporter; VACHT, Vesicular acetylcholine transporter.

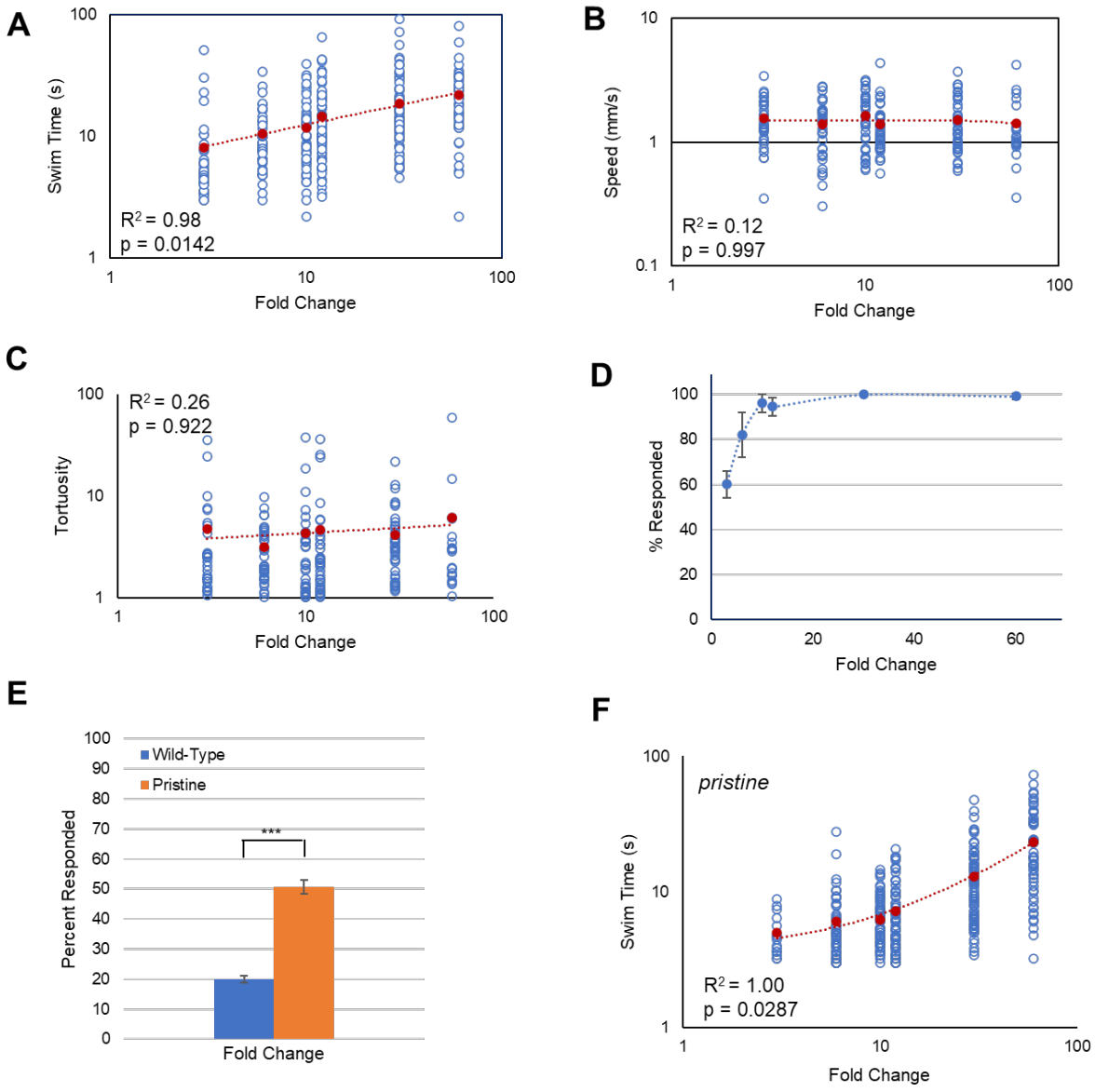

Figure 3.2. Response of *Ciona* larvae to fold change light dims. (A) Larval swim times increase as a power function in response to increased fold change light dimming (3-fold to 60-fold; log/log plot shown). All data points (blue circles) and averages (red circles) are shown [same for panels (B, C, and F)]. See Movie 1 in (Borba et al., 2021) for representative results. (B) Swim speed is constant across fold change dimming series (log/log plot shown). (C) Swim tortuosity is constant across fold change dimming series (log/log plot shown). (D) The percent of larvae responding as a function of fold change dimming. Shown in graph are

the averages from three recordings (± S.D.). (E) Percent of larvae responding to a six-fold dim at low illumination conditions (30 lux to 5 lux). n = 76 and 131, for wild-type and *pristine*, respectively (*** = $p < 0.001$; Wilcoxon Rank-Sum test). (F) Larval swim times of homozygous *pristine* mutants increase as a linear function in response to increased fold change light dimming (3-fold to 60-fold; log/log plot shown). See Figure 3.2.1 for sample sizes, average values, and statistical analyses. All larvae were observed for 2 min after dimming. The p-values shown were determined from a Kruskal-Wallis test.

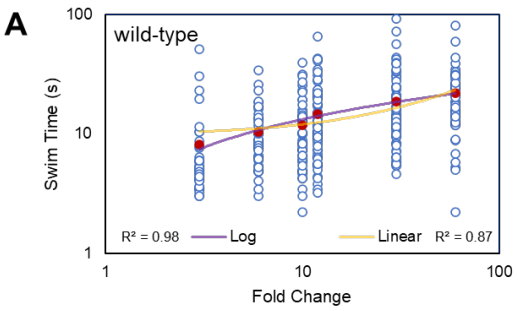

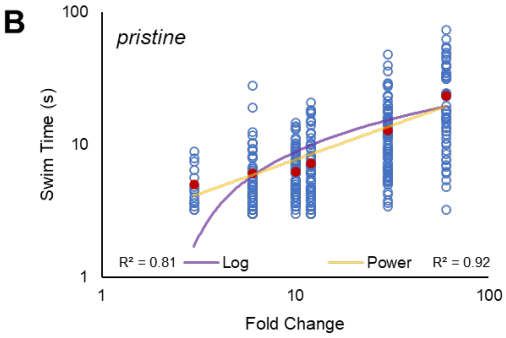

C

Experimental *n*-values

Fold Change	WT Swim Time	*prs* Swim Time	Speed	Tortuosity	% Respond
3	38	15	29	29	127
6	44	56	36	36	102
10	53	70	35	35	105
12	68	72	36	36	125
30	79	90	41	41	132
60	48	56	20	20	143

D

Experiment Averages ± Standard Deviation

Fold Change	WT Swim Time	*prs* Swim Time	Speed	Tortuosity	% Respond
3	8.07±9.15	4.97±1.82	1.56±0.99	4.75±14.69	60.06±5.95
6	10.45±6.30	6.07±4.22	1.40±0.98	3.12±14.27	81.94±9.89
10	11.88±7.95	6.24±2.78	1.65±0.96	4.30±13.85	96.16±4.01
12	14.63±11.38	7.19±4.40	1.41±0.94	4.70±13.48	94.61±4.06
30	18.70±14.80	12.84±8.26	1.51±0.92	4.14±13.15	100.00±0.00
60	21.86±13.98	23.30±15.99	1.42±0.90	6.07±12.82	99.19±1.41

E

Statistical Test *p*-values

WT Swim Times

FC	3	6	10	12	30
6	4.29E-04				
10	2.79E-04	0.2665			
12	1.41E-05	0.0223	0.1093		
30	1.34E-07	1.78E-05	2.67E-04	0.0088	
60	1.77E-07	2.17E-07	2.56E-06	1.18E-04	0.0194

Speed

FC	3	6	10	12	30
6	0.4095				
10	0.8292	0.2206			
12	0.2222	0.7740	0.2385		
30	0.5197	0.7323	0.5048	0.6867	
60	0.1895	0.7517	0.2446	0.5901	0.4024

prs Swim Times

FC	3	6	10	12	30
6	0.2721				
10	0.035	0.0565			
12	0.0464	0.0446	0.3559		
30	1.09E-06	7.99E-12	1.74E-11	1.12E-08	
60	5.89E-08	1.46E-14	8.21E-16	1.04E-13	5.85E-06

% Respond

FC	3	6	10	12	30
6	0.0304				
10	0.0010	0.0823			
12	0.0011	0.1096	0.6618		
30	0.0003	0.0342	0.1729	0.0832	
60	0.0004	0.0404	0.2854	0.1390	0.3739

Tortuosity

FC	3	6	10	12	30
6	0.7665				
10	0.6563	0.5011			
12	0.7365	0.5849	0.9587		
30	0.2379	0.4717	0.1595	0.1269	
60	0.5085	0.9932	0.6058	0.5668	0.6727

Fold-Change	WT vs. PRS
3	0.6642
6	2.05E-06
10	9.94E-07
12	5.14E-08
30	0.0018
60	0.8962

Figure 3.2.1. Expanded data for Figure 3.2. **A**. Plot of data from Figure 3.2A showing other curves tested: log and linear. **B**. Plot of data from Figure 3.2F showing other curves tested: log and power. **C**. Number of larvae (n) assessed in the fold change series (3 - 60, first column) for WT swim time (panel 3.2A), speed (panel 3.2B), tortuosity (panel 3.2C), percent responding (panel 3.2D), and prs swim time (panel 3.2F). **D**. The experimental averages and standard deviations for the assays described in panel A. **E.** Pairwise tests for significance at

each fold-change for swim time (WT and *prs*), speed, percent response and tortuosity (p-values shown; all comparisons by Wilcoxon, except percent response, which was done by T-test). Also shown (bottom right) is a comparison of swim times in WT and *prs* larvae at each fold-change step. p-values for each comparison are listed. WT = wild type; *prs* = *pristine* mutant; FC = fold change.

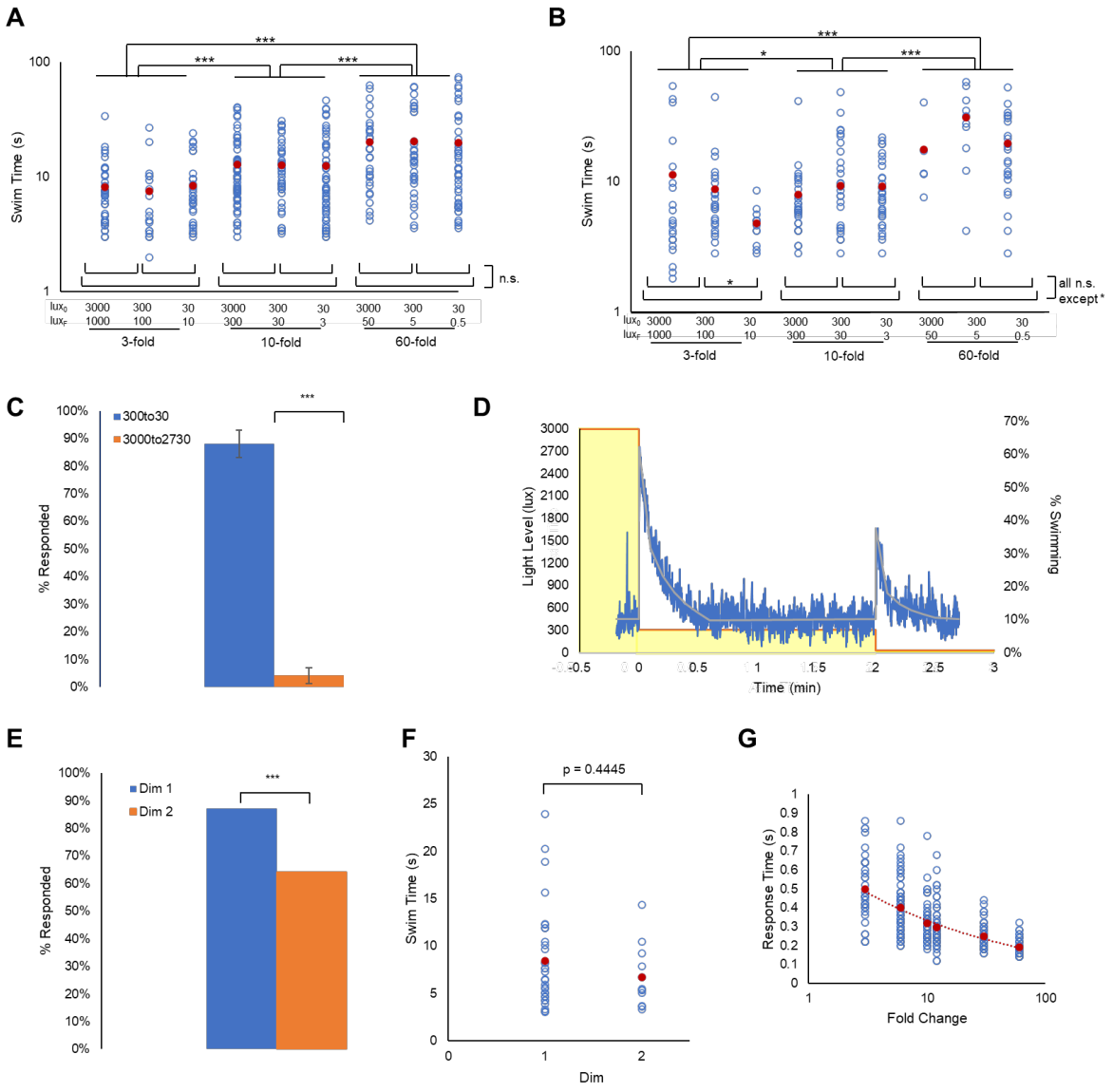

Figure 3.3. *Ciona* fold change detection response. (A) *Ciona* larvae swim times show scale-invariance to light dimming across three orders of magnitude. Lux_0: initial illumination level in lux; Lux_F : illumination after dim in lux (log/log plot shown). (B) Same light-dimming series as in panel A, but with *pristine* mutants (log/log plot shown). (C) The *Ciona* light-dimming response follows Weber's law. Shown are the percent of larvae responding to 270 lux dimming from the initial conditions of 300 lux or 3000 lux (n = 776 and 443; respectively). (D) *Ciona* larvae show absolute adaptation to light-dimming. Larvae were

exposed to two light dimmings separated by 2 min (3000 lux to 300 lux, and 300 lux to 30 lux; yellow boxes). The blue line shows the percent of larvae swimming at 1 s time intervals (n = 91–320). The gray line is the average at each time point. See also Movie 2. (E) For data shown in panel (D), a higher percentage of larvae responded to the 3000 to 300 lux dim (Dim 1) than to the 300 to 30 lux dim (Dim 2). (F) For the experiment shown in panel (D), the swim times induced by the 3000 to 300 lux dim (Dim 1) were not different from the 300 to 30 lux dim (Dim 2). (G) Plot of the reaction time versus fold change. This is defined as the time point at which swimming was first detected following dimming. For panels (A, B, F, and G), all data points (blue circles) and averages (red circles) are shown. See Figure 3.3.1 for full data and statistical analyses. (*** = $p < 0.001$; * = $p < 0.05$; n.s. = not significant).

A *Wild-type*

Fold Change	3-fold			10-fold			60-fold		
Δlux	3000to1000	300to100	30to10	3000to300	300to30	30to3	3000to50	300to5	30to0.5
Average ± SD	8.23±5.89	7.49±6.42	8.35±5.74	12.81±9.41	12.74±7.95	12.56±10.90	20.32±15.43	20.61±16.86	19.92±19.55
n	39	19	34	62	39	54	31	34	43

within fold changes

3-fold	3000to1000	300to100
300to100	0.7327	
30to10	0.3187	0.4726

10-fold	3000to300	300to30
300to30	0.7246	
30to3	0.2942	0.2705

60-fold	3000to50	300to5
300to5	0.2737	
30to0.5	0.8595	0.3729

between fold changes

	3-fold	10-fold
10-fold	1.88E-05	
60-fold	4.36E-11	2.79E-04

B *Pristine*

Fold Change	3-fold			10-fold			60-fold		
Δlux	3000to1000	300to100	30to10	3000to300	300to30	30to3	3000to50	300to5	30to0.5
Average ± SD	11.30±14.91	8.81±8.19	4.78±1.59	8.00±7.09	9.31±7.14	9.25±5.31	17.68±13.26	31.02±17.29	19.65±12.78
n	22	26	12	28	19	34	5	10	23

within fold changes

3-fold	3000to1000	300to100
300to100	0.1818	
30to10	0.6781	0.0142

10-fold	3000to300	300to30
300to30	0.7946	
30to3	0.1788	0.5403

60-fold	3000to50	300to5
300to5	0.1292	
30to0.5	0.7414	0.0685

between fold changes

	3-fold	10-fold
10-fold	0.01977	
60-fold	1.40E-08	1.18E-08

C

Weber's Law			
	300to30	3000to2730	p-value
% Responded	88.04±4.94	4.10±2.82	1.00E-07
n	776	443	

D

Light Adaptation			
	Dim 1	Dim 2	p-value
Swim Time	8.47±5.24	6.72±3.27	0.4445
% Responded	87.25	64.29	2.28E-04
n	102	84	

E Experiment Data for response times

Fold-Change	Average ± SD	n
3	0.50±0.17	39
6	0.40±0.14	65
10	0.32±0.10	64
12	0.30±0.11	55
30	0.25±0.06	52
60	0.19±0.04	49

F Statistical Test p-values for response times

FC	3	6	10	12	30
6	3.80E-03				
10	2.56E-08	1.65E-04			
12	2.45E-08	5.39E-06	0.0701		
30	5.14E-12	2.51E-11	7.00E-06	0.009	
60	1.03E-14	1.91E-17	5.01E-15	2.30E-10	2.28E-07

Figure 3.3.1. Expanded data for Figure 3.3. **A.** Average swim times, standard deviations, and number of larvae analyzed for data presented in Figure 3.3A. **B**. Average swim times, standard deviations, and number of larvae analyzed for data presented in Figure 3.3B. **C**. Data for results plotted in Figure 3.3C. Sample size (n), percent of larvae responding, and test of significance (p-value; T-test) are shown. **D**. Data for results plotted in Figures 3.3E and F. Included in the table are the number of larvae analyzed at each dim, the average swim times

(and standard deviations). Statistical analyses indicate that fewer larvae responded to Dim 2, but the average swim times were not different. **E.** Average response times, standard deviations, and number of larvae analyzed for data presented in Figure 3.3G. **F.** Pairwise statistical analysis of response times for results shown in Figure 3.3G (p-values shown; all comparisons by Wilcoxon).

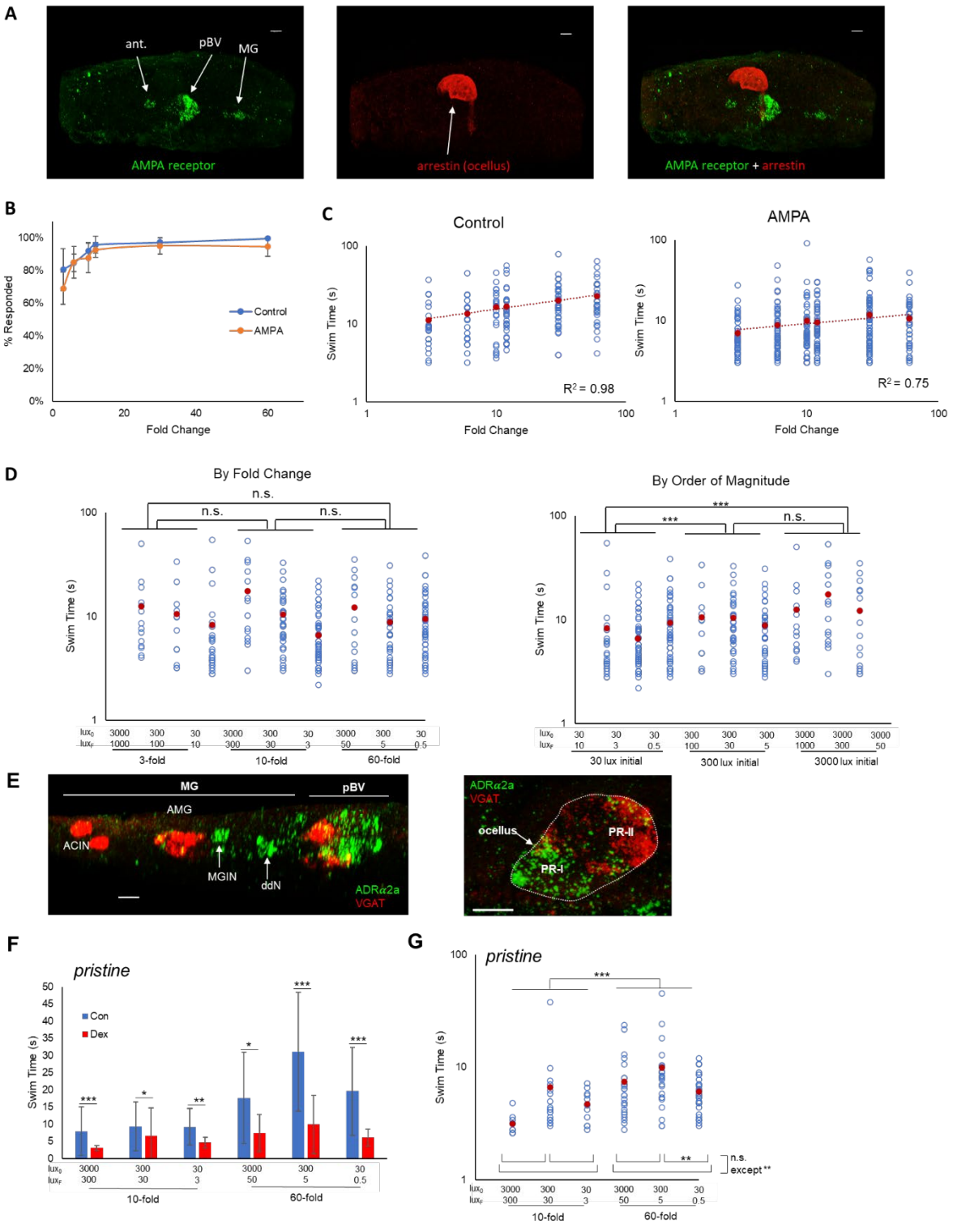

Figure 3.4. Pharmacological modulation of behavioral responses. (A) AMPA receptor expression detected by *in situ* hybridization (green; left panel). Photoreceptors were detected

by immunostaining for Arrestin detected by immunostaining (red; middle panel). Dorsal view, anterior to left. Right panel shows a merged view. Scale bars are 10 mm.(B) Percentage of control and AMPA-treated larvae responding to the indicated fold change light dimmings series. The averages from three recordings are shown (+ S.D.). (C) Swim times of control and AMPA-treated larvae in the indicated fold change dimming series. The R^2 valves for the curves are indicated. (D) AMPA-treated larvae do not show scale-invariance to fold-change dims of different magnitudes (left panel; compare to controls in Figure 3.3A). Right panel shows the same data sorted by magnitude of initial illumination (lux0). (E) *In situ* hybridization for ADRα2a (green) and VGAT (red). Scale bars are 10 μm. (F) Swim times for control ("con"; blue bars) and dexmedetomidine-treated ("dex"; red bars; 20 μM) pristine larvae. Shown are the responses to 10- and 60-fold dimming over three illumination ranges. Error bars represent standard deviations. (G) Dexmedetomidine-treated pristine larvae respond to increased fold change dimming with increased swim times. For panels (C,D,F,G) all data points (blue circles) and averages (red circles) are shown and are plotted log/log. (* = $p < 0.05$; ** = $p < 0.01$; *** = $p < 0.001$; n.s. = not significant; Wilcoxon Rank-Sum test). For full data and statistical analyses see Figures 3.4.1-3. ant., antenna cells; pBV, posterior brain vesicle; MG, motor ganglion; PR, photoreceptor; MGIN, motor ganglion interneurons; VGAT, Vesicular GABA transporter; ddN, descending decussating neuron; AMG, ascending motor ganglion interneuron; ACIN, ascending contralateral inhibitory neurons; ADRα2a, α2 adrenoreceptor.

A **Percent Responding**: Experiment Averages ± Standard Deviation

Fold Change	Control	AMPA
3	69.15±9.69	80.51±12.88
6	85.08±9.64	84.73±5.41
10	87.81±9.20	91.85±4.73
12	92.49±4.57	95.77±5.06
30	95.04±5.07	97.16±1.24
60	94.51±5.94	99.59±0.70

B **Percent Responding**: p-values for pairwise comparisons

Fold Change	Control vs. AMPA
3	0.2890
6	0.9588
10	0.5360
12	0.4517
30	0.5201
60	0.2153

C **Swim Times**: Experiment Averages ± Standard Deviation

	AMPA		Control	
Fold Change	Swim Time	n	Swim Time	n
3	6.97±4.58	47	11.24±8.24	22
6	8.86±7.77	57	13.55±10.29	17
10	9.96±12.82	51	16.44±11	22
12	9.56±7.15	57	16.6±12.69	31
30	11.79±10.63	72	20.04±13.75	37
60	10.58±7.68	36	22.59±13.77	30

D **Swim Times**: Comparisons within treatments (p-values)

AMPA

FC	3	6	10	12	30
6	0.1340				
10	0.0680	0.3932			
12	0.0332	0.2563	0.3343		
30	0.0023	0.0343	0.0620	0.1397	
60	0.0089	0.0801	0.1145	0.1971	0.5570

Control

FC	3	6	10	12	30
6	0.3100				
10	0.0422	0.1977			
12	0.0216	0.1883	0.5144		
30	5.11E-04	0.0181	0.1775	0.0561	
60	1.36E-04	0.0051	0.0515	0.0122	0.1737

E **Swim Times**: Comparisons between treatments (p-values)

AMPA vs Control	
3-fold	0.0074
6-fold	0.0257
10-fold	4.30E-03
12-fold	5.40E-04
30-fold	2.54E-05
60-fold	1.46E-05

F

Fold Change	3-fold			10-fold			60-fold		
Δlux	3000to1000	300to100	30to10	3000to300	300to30	30to3	3000to50	300to5	30to0.5
Average ± SD	12.56±12.18	10.55±9.08	8.31±10.78	17.49±14.76	10.46±7.11	6.60±4.44	12.28±10.59	8.82±6.07	9.43±7.21
n	14	12	27	14	32	54	15	37	45

G

within fold changes

3-fold	3000to1000	300to100
300to100	0.5035	
30to10	0.01491	0.1852

10-fold	3000to300	300to30
300to30	0.1931	
30to3	0.0009099	0.001755

60-fold	3000to50	300to5
300to5	0.785	
30to0.5	0.8376	0.8851

between fold changes

	3-fold	10-fold
10-fold	0.6773	
60-fold	0.4178	0.5278

H

within orders of magnitudes

30lux	30to0.5	30to3
30to3	0.02465	
30to10	0.04918	0.7712

300lux	300to5	300to30
300to30	0.3034	
300to100	0.7891	0.6732

3000lux	3000to50	3000to300
3000to300	0.2384	
3000to1000	0.6004	0.2801

between order of magnitudes

	30lux	**300lux**
300lux	0.006626	
3000lux	0.001368	0.1755

Figure 3.4.1. Expanded data for AMPA treatments shown in Figure 3.4. **A.** Averages of percent of control and AMPA-treated larvae responding to the indicated fold dimming for results plotted in Figure 3.4B. **B**. p-values (T-test) for pairwise comparisons at each fold change for results plotted in Figure 3.4B. **C.** Sample sizes (n), average swim times and standard deviations for data plotted in Figure 3.4C. **D**. Statistical analyses for data plotted in Figure 3.4C. All pairwise comparisons were made within treatments (AMPA or control) for each fold change (FC). p-valves are shown (Wilcoxon). **E.** Comparison of swim times at each fold change between treatments for results plotted in Figure 3.4C. p-valves are shown

(Wilcoxon). **F.** Sample sizes (n), averages and standard deviations for results plotted in Figure 3.4D. **G**. Statistical analyses of swim times of AMPA-treated larvae for data plotted according to fold change (Figure 3.4D; left panel). All tests within a fold change group, and between fold changes, were performed by Wilcoxon (p-values shown). **H.** Statistical analyses of swim times of AMPA-treated larvae for data plotted according to initial light intensity (Figure 3.4D; right panel). The initial light intensity (before dim) and are indicated as 30 lux, 300 lux and 300 lux in the figure. All tests within an initial intensity group, and between initial intensities, were performed by Wilcoxon (p-values shown).

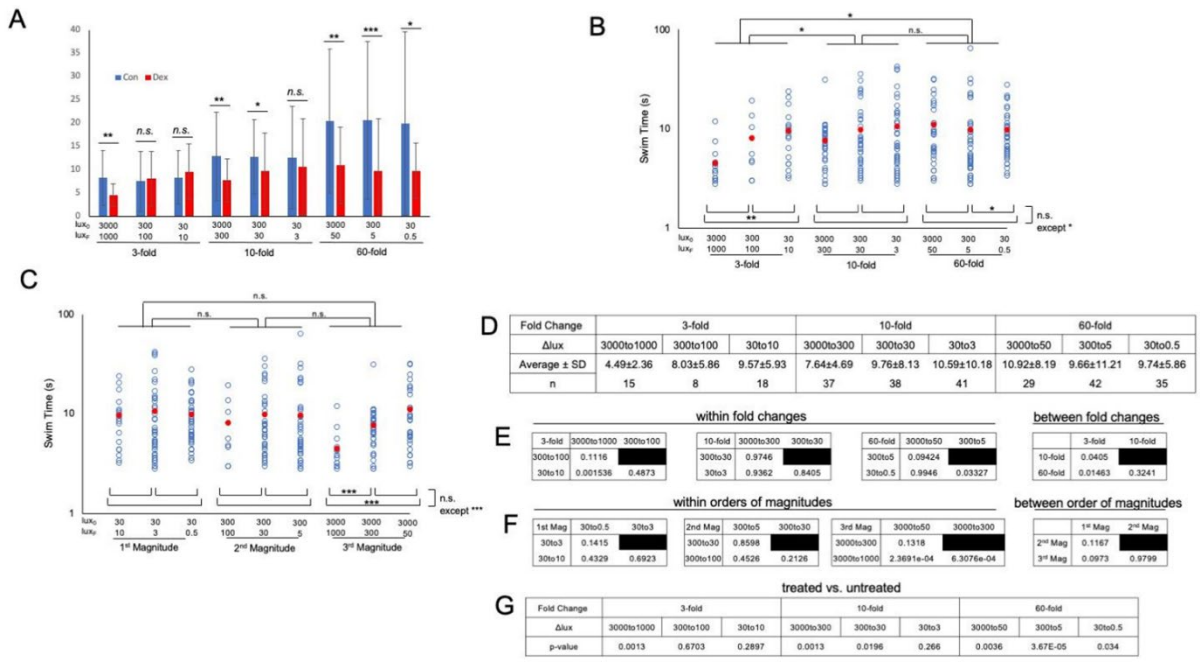

Figure 3.4.2. Dexmedetomidine treatment of wild-type larvae. **A.** Swim times for control (Con) and dexmedetomidine-treated (Dex) larvae following 3-, 10- and 60-fold dimming. The initial (lux_0) and final (lux_F) illumination conditions are indicated. **B**. Response of dexmedetomidine-treated wild-type larvae to fold-change dims of different magnitudes. **C.** Data from panel B sorted by magnitude of initial illumination (lux_0). **D**. Sample sizes (n), averages and standard deviations for results plotted in panels A-C. **E.** Statistical analyses of swim times of dexmedetomidine-treated larvae for data plotted according to fold change (panel B). **F.** Statistical analyses of swim times of dexmedetomidine-treated larvae for data plotted according to initial light intensity (panel C). The initial light intensity (before dim) and are indicated as 30 lux, 300 lux and 300 lux in the figure. **G.** Statistical analyses of swim times of dexmedetomidine-treated larvae versus non-treated for data plotted in panel A. All tests were performed by Wilcoxon (p-values shown). (* = $p < 0.05$; ** = $p < 0.01$; *** = $p < 0.001$; n.s. = not significant). For panels A-C, all data points (blue circles) and averages (red circles) are shown.

A Untreated *prs*

Fold Change	3-fold			10-fold			60-fold		
Δlux	3000to1000	300to100	30to10	3000to300	300to30	30to3	3000to50	300to5	30to0.5
Average ± SD	11.30±14.91	8.81±8.19	4.78±1.59	8.00±7.09	9.31±7.14	9.25±5.31	17.68±13.26	31.02±17.29	19.65±12.78
n	22	26	12	28	19	34	5	10	23

B Dexmedetomidine-treated *prs*

Fold Change	3-fold			10-fold			60-fold		
Δlux	3000to1000	300to100	30to10	3000to300	300to30	30to3	3000to50	300to5	30to0.5
Average ± SD	10.20±8.80	4.20±2.00	9.30±9.19	3.16±0.72	6.67±8.03	4.69±1.52	7.46±5.32	9.97±8.51	6.11±2.39
n	5	4	2	9	18	11	25	26	30

C

within fold changes

10-fold	3000to300	300to30
300to30	0.9988	
30to3	0.9947	0.3849

60-fold	3000to50	300to5
300to5	0.9663	
30to0.5	0.3739	0.0078

between fold changes

10-fold vs. 60-fold
p = 0.00000474

D

treated vs. untreated

Fold Change	10-fold			60-fold		
Δlux	3000to300	300to30	30to3	3000to50	300to5	30to0.5
p-value	0.000104	0.0344	0.0019	0.0122	0.000840	3.95E-06

Figure 3.4.3. Expanded data for Dexmedetomidine treatment of *pristine* larvae in Figure 3.4. **A**. Sample sizes (n), averages and standard deviations for control pristine results shown in Figure 3.4F. **B**. Sample sizes (n), averages and standard deviations for dexmedetomidine-treated pristine results shown in Figure 3.4F and G. **C.** Statistical analyses of swim times of dexmedetomidine-treated pristine larvae for data plotted according to fold change (Figure 3.4G). **D.** Statistical analyses of swim times of dexmedetomidine-treated pristine larvae versus non-treated for data plotted in Figure 3.4F. All tests were performed by Wilcoxon (p-values shown).

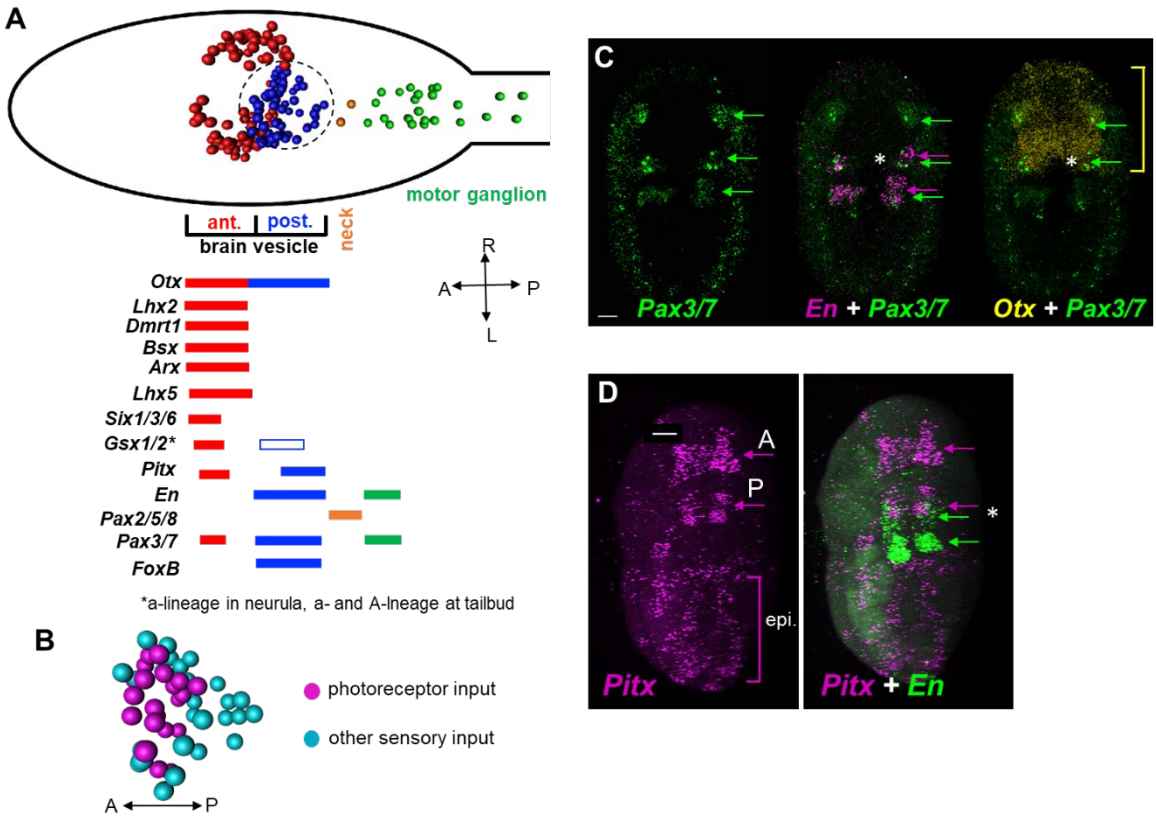

Figure 3.5. Gene expression in the *Ciona* posterior brain vesicle suggests homology with the vertebrate midbrain. (A) Top: Diagram of the *Ciona* larval CNS with the major brain regions indicated in color. The centroids of neurons are shown [from (Ryan et al., 2016)]. Bottom: summary of embryonic gene expression patterns marked by corresponding larval CNS domains. Domains in red show expression for orthologs to vertebrate forebrain markers, blue to midbrain, orange to MHB, and green to spinal cord. (B) Spatial distribution of relay neuron types in the pBV. Region shown corresponds to the circled area in panel (A) (centroids shown). (C) *In situ* hybridization for *Pax3/7*, *En*, and *Otx* in early tailbud *Ciona* embryos. The anterior domain of *En*, which marks the presumptive pBV, overlaps with *Pax3/7* (asterisk middle panel), and *En* (asterisk right panel). Yellow bracket shows anterior-

posterior extent of *Otx* expression. (D) *In situ* hybridization for *Pitx* and *En*. *Pitx* is expressed in anterior and posterior domains in early tailbud embryos. The posterior domain of *Pitx* overlaps with the anterior *En* domain in the pBV (asterisk right panel). Consistent with previous reports, labeling was also observed in the epidermis. Green arrows in panels (C) are indicating domains of *Pax3/7* expression in the developing central nervous system. In panel (D), green arrows indicate domains of *engrailed* expression, and magenta arrows indicate domains of *Pitx* expression the central nervous system. Asterisk indicates overlapping expression of *Pitx* and *engrailed*. A, anterior; P, posterior; epi, epidermis. Anterior is to the left for panel A and D, and to the top for B and C. Scale bars are 10 μm.

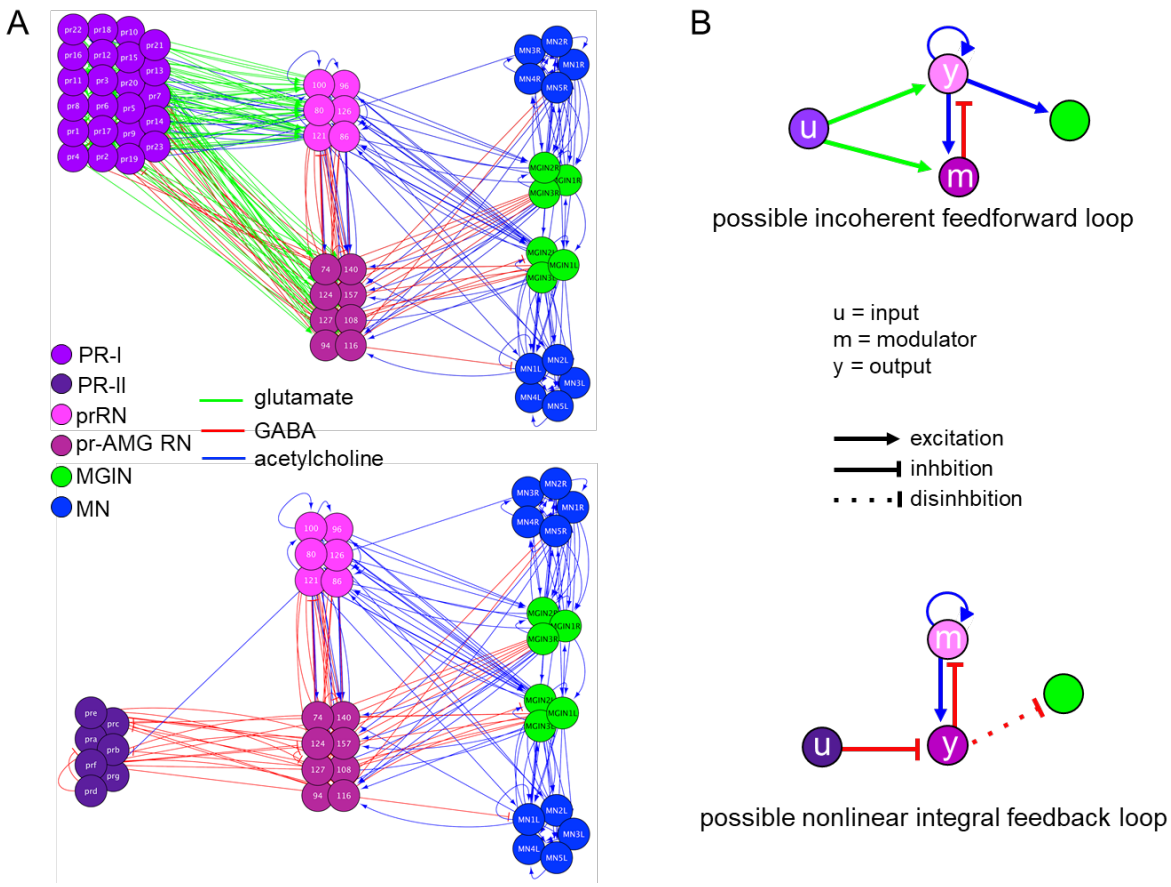

Figure 3.6. Visuomotor circuits and putative fold change detection circuits. (A) Full circuits for the PR-I (top) and PR-II (bottom) pathways from the *Ciona* connectome (Ryan et al., 2016). Neurotransmitter use for synaptic connections (lines) is based on (Kourakis et al., 2019). PR, photoreceptor; prRN, photoreceptor relay neuron; pr-AMG RN, photoreceptor ascending motor ganglion relay neurons; MGIN, motor ganglion interneurons; MN, motor neurons. (B) Simplified circuits for the PR-I (top) and PR-II (bottom) pathways derived by combining like cells and assigning valence of synapses (excitatory or inhibitory) based on consensus for that cell type. Nodes are labeled according to the proposed function (i.e., input modulator, and output). Colors of neuron classes are according to (Ryan and Meinertzhagen, 2019).

4. AN EXPRESSION ATLAS OF GLUTAMATE RECEPTORS IN THE PRIMITIVE CHORDATE *CIONA* SENSORIMOTOR CIRCUIT MODELS

Cezar Borba, Matthew J. Kourakis, Yishen Miao, and William C. Smith.

[Manuscript in progress]

4.1 Introduction

The tadpole larva of the invertebrate chordate *Ciona* is proving itself to be a highly tractable model for sensorimotor circuit analysis. Not only does the *Ciona* larval central nervous system (CNS) contain only ~180 neurons, it is one of the few animals for which a complete synaptic connectome has been generated (Ryan et al., 2016). Moreover, numerous studies have highlighted the conservation between the *Ciona* larval CNS (and those of other *tunicates*- the group of chordates to which *Ciona* belongs), and vertebrate CNSs [reviewed in (Hudson, 2016)]. At the anatomical level, the *Ciona* CNS is subdivided into domains showing homology to the vertebrate forebrain, midbrain, hindbrain, midbrain hindbrain boundary (MHB), and spinal cord (Figure 4.1A). These homology assignments are based on several types of data, including conserved developmental mechanisms, gene expression, anatomy, and most recently, neuron classification and synaptic connectivity (Borba et al., 2021; Hudson, 2016; Ryan et al., 2017; Wada et al., 1998). Early descriptions of larval tunicate nervous systems, often made before the above homologies were clear, lead to the naming of these anatomical domains by names that do not reflect this homology (*e.g.*, *anterior sensory vesicle* or *anterior brain vesicle* for the *Ciona* forebrain homolog, and *visceral* or *motor ganglion* for the hindbrain homolog). For the sake of clarity, and to make

Ciona neurobiology accessible to a broader readership, we will henceforth refer to the *Ciona* CNS anatomical domains according to their vertebrate homologs.

The published *Ciona* connectome has been instrumental in identifying minimal neural circuits that drive a number of larval behaviors, including those for negative phototaxis, light-dimming/escape response, negative gravitaxis, and an escape response mediated by peripheral mechanoreceptors (Borba et al., 2021; Bostwick et al., 2020; Kourakis et al., 2019; Ryan et al., 2016, 2018; Salas et al., 2018). However, the connectome, which was derived by serial-section electron microscopy, provides only a "bare-bones" view of the neural circuitry. Understanding the mechanisms and logic of these circuits requires that "flesh" be added in form of the properties of the individual neurons of these circuits (*e.g.*, neurotransmitter use and neurotransmitter receptor expression). Through analysis of *in situ* hybridization patterns for markers for small-molecule neurotransmitters [*e.g.*, vesicular acetylcholine transporter (VAChT) for cholinergic neurons, vesicular GABA transporter (VGAT) for GABAergic/glycinergic neurons, tyrosine hydroxylase (TH) for catecholaminergic neurons, and tryptophan hydroxylase (TPH) for serotonergic neurons] a detailed picture of the neurotransmitter use in the *Ciona* larval CNS is emerging (Kourakis et al., 2019; Moret et al., 2005b; Pennati et al., 2007). The small number of larval neurons and the largely stereotype expression patterns facilitates the attribution of neurotransmitter use to known neurons identified by the connectome (Kourakis et al., 2019). For example, all vesicular glutamate transporter (VGLUT)-positive neurons in the *Ciona* larva are sensory (*i.e.*, there are no glutamatergic interneurons or efferents). The list of glutamatergic neurons includes the photoreceptors, the gravity-sensitive antennae cells, and the peripheral epidermal sensory neurons (Horie et al., 2008b; Kourakis et al., 2019). TH expression is limited to the

photoreceptor-like coronet cells, and these neurons are presumed to be domainergic - although the *Ciona* genome appears to lack a definitive dopamine receptor (Lemaire et al., 2021; Moret et al., 2005a). Interneurons of the CNS are either $VGAT^{+}$, $VAChT^{+}$, or express none of the markers of small molecule neurotransmitters and are likely peptidergic (Hamada et al., 2011; Kourakis et al., 2019). In the midbrain, VAChT and VGAT are expressed in distinct, non-intermingled, domains, with the VAChT domain anterior to the VGAT domain, while in the hindbrain VAChT expression dominates with VGAT expression limited to six *ascending MG peripheral interneuron* (AMG) neurons in the dorsal midbrain, and the four *ascending contralateral inhibitory neurons* (ACINs) (Kourakis et al., 2019). The spinal cord was initially thought to lack neurons, and to consist of only ependymal cells. However, the connectome revealed the presence of spinal cord neurons, named *midtail neurons*, and seen in Figure 4.1A expressing VACHT (white arrows).

In order to better understand the role of glutamate system in *Ciona* behavior and neural circuitry, and to complement our knowledge of neurotransmitter distribution, we undertook a comprehensive examination of the 3-dimensional expression patterns of the glutamatergic ionotropic receptors (AMPA, NMDA, and kainate) and metabotropic receptors (mGluR) at larval stage using hybridization chain reaction *in situ* (Choi et al., 2018). Additionally, pharmacological antagonists were used to assess the behavioral roles of NMDA receptors (NMDA-R) [the role of AMPA receptors (AMPA-R) in *Ciona* larvae has been assessed previously (Bostwick et al., 2020; Kourakis et al., 2019)]. While the tunicates are the closest extant relatives of the vertebrates, they diverged in a number of important ways from the vertebrates. Significantly, the tunicates split from the vertebrates before two whole-genome duplications occurred in the vertebrate lineage (Dehal and Boore, 2005). The result

being that tunicates have smaller genomes, and in most cases have fewer members of gene families when compared to vertebrates. This relationship is evident in the glutamate receptors. The *Ciona* genome encodes single copies of the AMPA and kainate receptors, as well as single copies of each NMDA receptor subunit (Okamura et al., 2005), and three genes putatively encoding mGlu receptors have been identified in the *Ciona* genome (Kamesh et al., 2008). Thus, the relative genomic simplicity of *Ciona* greatly simplifies the task of generating a comprehensive view of the expression of the glutamine receptors, while the relatively simple behaviors of *Ciona* larvae, and of the circuits driving them, aids in the assessment of the roles of the glutamatergic receptors.

4.2 Materials & Methods

4.2.1 Animals

Adult *Ciona robusta* [also known as Ciona intestinalis type A] were collected at the Santa Barbara Harbor. Gametes were dissected from adults and crossed *in vitro* to generate larvae. All embryos and larvae were cultured at 18°C.

4.2.2 *In situ* hybridization and image collection

Whole mount fluorescent *in situ* hybridization of larval *C. robusta* were performed using the hybridization chain reaction method (v. 3.0, Molecular Instruments; Los Angeles, CA, United States), as previously described (Kourakis et al., 2019). Complementary RNA probe sets were designed to coding regions for the following *Ciona* genes (unique gene identifiers provided in parentheses): AMPA receptor (XM_018817034.1), NMDA receptor (XM_018816819.1), Kainate receptor (XM_026833998.1), metabotropic glutamate receptor 123 (XM_009859697.3), metabotropic glutamate receptor 478 (XM_018816381.1), VGAT

(NM_001032573.1), and VAChT (NM_001032789.1). Larvae for *in situ* hybridization were dechorionated at mid-tailbud stage using sodium thioglycolate/protease E or 0.1% trypsin, so that left-right asymmetric properties of the CNS would not be disrupted, as described previously (Kourakis et al., 2021). Labeled animals were imaged on an Olympus Fluoview 1000 confocal microscope; post-image analysis used Imaris v6.4.0.0 or ImarisViewer v9.5.1 as well as Fiji (ImageJ) v. 2.0.0-rc-69/1.52p.

4.2.3 Registration of *in situ* hybridization patterns to the connectome

An image stack file for the *in situ* HCR results containing VGAT expression was rendered into a 3D object using a custom python code and then loaded into a custom software in Unity. The centroid and volume of neurons from three groups were also rendered in the same space using data from the connectome: PR-I (pr9 and pr10 only), PR-II, eminens cells, and AMG. The expression objects were then overlaid with the neuron centroid representations manually using the matching criteria as follows: in relation to VGAT, the dorsal cap marks the eminens cells, and the two patches, a smaller posterior one and larger anterior one, on the right mark the two photoreceptor groups, PR-I (only pr9 and pr10) and PR-II, respectively, while the patch of VGAT in the motor ganglion represent the AMG. After this alignment is done, expression objects with no consistent landmarks, such as VAChT, are brought into view for analysis. Using common structures and overlaps across different *in situs*, all the expression objects were overlapped in reference to each other. Once the objects are aligned, a collision detector is used to compute the expression objects in contact with all the neurons from the connectome data.

4.2.4. Behavioral Assays

All larvae were between 25 and 28 h post fertilization (hpf) (18°C). Larval swimming behaviors were recorded in seawater using 10 cm agarose-coated petri dishes to reduce sticking. Image series were collected using a Hamamatsu Orca-ER camera fitted on a Navitar 7000 macro zoom lens. Programmable 700 and 505 nm LED lamps (Mightex) mounted above the petri dishes were used for dimming response assays as described previously (Borba et al., 2021; Bostwick et al., 2020; Kourakis et al., 2019). The dim response movies were recorded at 10 frames per second (fps). The larvae were recorded for 10 s at the initial intensity (3 mW/cm^2) that was then dimmed (0.3 mW/cm^2) while image capture continued for 1 min. Larvae were allowed to recover for 5 min before being assessed again. All light intensity readings were taken with an Extech Instruments light meter. For pharmacological experiments, MK801 (Tocris) was dissolved in seawater to a concentration of 500 μM, and the larvae were exposed to the drug for 10 minutes before being assessed.

4.3 Results

4.3.1 Ionotropic glutamate receptors are expressed in broad, partially overlapping domains

The HCR *in situ* hybridization procedure allows for the easy visualization of multiple fluorescently labeled probes in a single sample (Choi et al., 2018). For detection of ionotropic glutamate receptors, *in situ* probes were tested in groups of three. Figure 4.1B shows the expression of VAChT with the AMPA and NMDA receptors in a representative 25 hours post fertilization (hpf) larva. Figure 4.2 shows the expression of VGAT with NMDA and kainate receptors in an identically staged larva. For the NMDA receptor, the *Ciona* homolog of the GluN1 subunit was used, as it is common to all NMDA-R complexes (Paoletti et al., 2013). The VGAT and VAChT probes were included to serve as internal

spatial references for 3-dimensional registration, as their expression domains have been partially described previously (Kourakis et al., 2019). Figures 4.1 and 4.2 show z-projections of 3-dimensional confocal images.

As seen in Figure 4.1B, the AMPA-R expression domain in the fore- and midbrains is more extensive than the NMDA receptor. Expression of AMPA-R in the absence of NMDA-R was observed in the forebrain (white arrowhead), as well as the posterior midbrain (red arrowhead). We also observed a domain in the midbrain expressing NMDA-R, but not AMPA-R (green arrows in Figure 4.1B, lateral view). No expression of either NMDA-R or AMPA-R was observed in the MHB region. By contrast to the fore- and midbrains, the expression of NMDA-R in the hindbrain was more extensive than that of the AMPA-R. With the exception of the seven dorsally located AMG neurons (Ryan et al., 2018), the *Ciona* hindbrain is divided into distinct left and right sides. This is most conspicuous in the five cholinergic motor neurons found on each side which innervate tail muscles on the corresponding side (Ryan et al., 2016). However, this left/right symmetry is also present in the interneurons of the ventral hindbrain. Despite the symmetry of the ventral hindbrain at the level of neurons, we recently reported that AMPA-R is expressed only on the left side [(Kourakis et al., 2021) and blue arrowhead Figure 4.1B, dorsal view]. In contrast, we report here that the NMDA-R is expressed symmetrically on the left and right right sides of the ventral hindbrain (orange arrowhead). Finally, we observed that expression of the kainate receptor was restricted to the MHB, and possibly neurons of the posterior midbrain (Figure 4.2) (see next section for registration of expression patterns to specific neurons). The kainate expression domain appears to be exclusive of the AMPA-R and NMDA-R expression domains.

4.3.2 Mapping of expression patterns and identification of expressing neurons

In previous studies, we have taken advantage of the small number of neurons in the *Ciona* nervous system and the stereotyped cellular anatomy to map *in situ* expression patterns to individual neurons of the *Ciona* connectome, although with varying degrees of confidence (Kourakis et al., 2019). Briefly, 3-dimensional *in situ* image stacks are rendered into 3-dimensional expression objects through a custom Python code that is then loaded into a custom Unity program. Also loaded are the x-, y-, and z-coordinates of centroids of the reconstructed neurons from the connectome. The expression objects are first manually overlayed on the centroids using established landmarks (*e.g.*, photoreceptors). Once the landmarks are aligned to the centroids, (Figure 4.2.1), a custom Unity program was run to detect the overlap of centroids with the expression objects to predict expression in the connectome neurons. An example of the raw results is seen with the expression of VAChT (Figure 4.2.1), which overlaps with the *bipolar interneurons* (BPIN), loops around two *photoreceptor-ascending MG neuron relay neurons* (pr-AMG RNs; 108 and 116) to overlap with the *anaxonal arborizing neurons* (aaINs), and then extends dorsally to the *photoreceptor relay neurons* (prRNs) (Figure 4.2.1; Figure 4.2.2 for neuron color classification).

The Unity program was run for the ionotropic glutamate receptors, as well as VGAT and VAChT to generate expression predictions. The results summarized in Table 4.1 and displayed as 3-dimensional overlays on the centroids in Figures 4.3 and 4.4. Neurons co-expressing AMPA-R and NMDA-R were identified, as well as neurons expressing only single ionotropic receptor types, including kainate receptors. Predicted matches of glutamatergic receptor expression to neurons of the connectome in many cases conform to

expectations from the connectome. For example, the Unity program output predicts that the glutamate receptor-expressing neurons of the forebrain are *peripheral nerve interneurons* (PNINs) (Table 4.1), which receive direct synaptic input from $VGLUT^+$ neurons- in this case from the *rostral trunk epidermal neurons* (RTENs) (Ryan et al., 2018). Thus, our prediction that glutamate receptor positive forebrain neurons are the neurons that receive extensive glutamatergic input supports our approach of mapping 3D *in situ* hybridization patterns to the neurons of the connectome.

4.3.3 NMDA receptors are required for sensorimotor responses

In a previous study we found that the AMPA-R inhibitor perampanel blocked negative phototaxis in *Ciona* larvae, but not their ability to respond to dimming light (Kourakis et al., 2019). This result is consistent with the differential expression of AMPA-R on the primary interneuron targets of the photoreceptors. The prRNs are thought to mediate phototaxis, and express AMPA-R. In contrast, the pr-AMG RNs are thought to mediate the dimming response, and do not express AMPA-R (Table 4.1). We report here that NMDA-Rs are widely expressed in the *Ciona* larval CNS, including in the pr-AMG RNs and the prRNs.

The non-competitive NMDA receptor antagonist MK801 was used to assess the role of NMDA-Rs in visuomotor responses. MK801 shows strong inhibition and specificity in both vertebrates and invertebrates (Vogeler et al., 2021; Wong et al., 1986). We observed that unlike the AMPA-R antagonist perampanel, MK801 completely inhibited the dimming response. In this assay, larval behavior was recorded using far-red illumination (700 nm), while a 505 nm LED lamp was dimmed from 3 to 0.3 mW/cm^2. Figure 4.5 shows a temporal projection of the larvae for the 5 seconds immediately before and after the dim. Before the dim, larvae are mostly stationary, but in response to dimming the control larvae immediately

initiate swimming, which are seen as lines in the time-projection image (see labels in Figure 4.5). In contrast, larvae treated with 0.5 mM MK801 did not respond to dimming (bottom two panels). A similar result was observed in a phototaxis assay. In the phototaxis assay, the larvae are placed in a petri dish with a light of constant intensity at one side and recorded for one hour (Salas et al., 2018). At the end of the assay period, phototaxis is evident by the accumulation of larvae at the side of the petri dish furthest from the light source. Figure 4.6 shows an image of the control and MK108-treated larvae at the start of the phototaxis assay (t=0), in which the larvae can be seen evenly distributed across the petri dishes (left panels). The right panels show a temporal projection of the assay from time points 30 to 60 minutes. The accumulation of larvae at the left side of the petri dish (away from the light) is evident in the control, but not in the MK801-treated sample. Thus, the NMDA-R antagonist MK801 is effective at inhibiting both the dimming response and phototaxis, unlike the AMPA antagonist perampanel, which only inhibits phototaxis. Because of the widespread expression of NMDA-Rs, including the mid- and hindbrain (Table 4.1 and Figure 4.3), it is not possible to attribute the behavioral effects of MK801 to particular neurons of the circuit.

4.3.4 Expression of mGlu receptors is limited to the peripheral nervous system

Analysis of the *Ciona* genome revealed the presence of three putative metabotropic glutamate receptors (mGluR) (Kamesh et al., 2008). Based on their orthologies to vertebrate mGluRs, they were named mGluR123, mGluR478, and mGluR147 (https://www.aniseed.cnrs.fr/). Our examination of a single cell RNAseq dataset (Cao et al., 2019) indicated that only mGluR123 was expressed at high levels at larval stage (Figure 4.7.1). *In situ* hybridization for mGluR123 revealed expression in the epidermal sensory neurons, but no apparent central nervous system expression (Figure 4.7). It appears as though

all epidermal sensory neurons express mGluR123, including the *rostral trunk epidermal neurons* (RTEN), the *anterior* and *posterior rostral trunk epidermal neurons* (aATEN and pATEN, respectively), and the *dorsal* and *ventral caudal epidermal neurons* (DCEN and VCEN, respectively) [Figure 4.7; for a complete description of *Ciona* epidermal sensory neurons refer to (Ryan et al., 2018)]. The centroids for the peripheral sensory neurons were not given by the connectome, so they were not analyzed using our Unity program. Nevertheless, the cells are very distinct and the *in situ* expression pattern can be confidently attributed to these cells. An *in situ* hybridization was also performed for mGlu478 (but not for mGlu147), and no expression was detected.

4.4 Discussion

We present here a comprehensive prediction of glutamate receptor expression in the neurons of the *Ciona* larvae. Also presented is a prediction of the distribution of $VGAT^{+}$ and $VAChT^{+}$ neurons that expands on our previous observations (Kourakis et al., 2019). Finally, we assessed the effects of NMDA-R receptor inhibition in two visuomotor assays and found them to be essential for visuomotor responses. Receptor expression results are presented in Table 4.1 and superimposed on a 3-dimensional depiction of CNS neuron centroids in Figures 4.3 and 4.4. It is important to note that our results are for a specific developmental stage of the larva (~25 hours post-fertilization at 18°C). We have observed changes in *Ciona* larval behavior over time-scales as short as 2-3 hours (Bostwick et al., 2020; Salas et al., 2018), so it is possible that the expression of the glutamate receptors is temporally dynamic within the larva. Nevertheless, in the temporal window that was analyzed here, the distribution of glutamate receptors in the *Ciona* nervous system provides new insights into the neural mechanisms in this simple chordate.

4.4.1 Glutamate receptors in the fore- and midbrain

We previously reported using VGLUT as a marker for glutamatergic neurons and observed expression in sensory neurons (photoreceptors, antenna cells and peripheral sensory neurons), but no expression in interneurons (Kourakis et al., 2019). The expression of AMPA-R and NMDA-R reported here agrees with the synaptic targeting of fore- and midbrain neurons by VGLUT$^+$ sensory neurons. Interestingly, the photoreceptors themselves are mostly glutamatergic, and connectome predicts extensive chemical synapses between the photoreceptors. Despite this we found no evidence of glutamate receptor expression in the photoreceptors. The nature of the apparent chemical synapse between the photoreceptors remains to be determined.

In contrast to the forebrain, which only expresses glutamate receptors in a limited number of neurons, expression of AMPA-R and NMDA-R in the midbrain was much more extensive. The anterior midbrain receives input from the photoreceptors, while the posterior midbrain receives synaptic input from the antennae neurons, which mediate gravitaxis (Ryan et al., 2016). The target of the two VGLUT$^+$ antenna sensory neurons, the VGAT$^+$ *antenna relay neurons* (AntRNs), all express either NMDA-R, AMPA-R, or both (Table 4.1, Figure 4.3 and 4.4). The eleven AntRNs have a surprisingly complex synaptic connectivity, with some receiving input from one antenna neuron, some from the other, and some from both (Ryan et al., 2016). The results here suggesting heterogeneity of glutamate receptor expression only adds to the apparent complexity and calls out for further investigation.

Photoreceptor input to the *Ciona* larval midbrain is even more complex than antenna cell input. The visual organ of *Ciona*, the ocellus, contains two distinct groups of photoreceptor, PR-I and PR-II (Horie et al., 2008a; Kourakis et al., 2019). PR-I consists of 23

photoreceptors (21 VGLUT$^+$, one VGAT$^+$, and one VGLUT$^+$/VGAT$^+$), all of which project their outer segments into the ocellus pigment cell. The direction-dependent shading caused by the pigment cell as the larvae perform short orienting swims provides a cue to the direction of light, and thereby mediates negative phototaxis (Salas et al., 2018). By contrast, the seven PR-II photoreceptors (three VGAT$^+$ and four VGLUT$^+$/VGAT$^+$) are not associated with the pigment cell and are sensitive to light from all directions, and thereby mediate a light-dimming (also known as a looming shadow) escape behavior (Salas et al., 2018). The PR-I photoreceptors project axons to two distinct classes of primary interneurons in the midbrain, the prRNs and the pr-AMG RNs (Ryan et al., 2016). At least four of the six prRNs are predicted to be cholinergic and express both AMPA-R and NMDA-R (Table 4.1 and Figure 4.3 and 4.4). Our model of phototaxis hypothesizes that the cholenergic prRNs relay excitatory input from the VGLUT$^+$ photoreceptors to secondary cholinergic interneurons in the hindbrain, and then to the motor neurons (Kourakis et al., 2019). However, the other midbrain interneuron class targeted by the PR-I photoreceptors, the pr-AMG RNs are predicted to be inhibitory (*i.e.*, VGAT$^+$; Table 4.1 and Figure 4.4). The prediction that PR-I photoreceptors project to both excitatory (prRNs) and inhibitory (pr-AMG RNs) relay neurons initially appears to be difficult to account for within the model. However, our observation here that the pr-AMG RNs express NMDA-Rs, but not AMPA-Rs, provides an explanation. In other words, AMPA-Rs mediate fast excitatory responses while NMDA-Rs have a slower modulatory role. Moreover, we hypothesized that the projection of the PR-I photoreceptors to both excitatory and inhibitory primary interneurons constituted an *incoherent feedforward loop* circuit motif that functions in visual processing to generate the observed fold-change detection behavior in phototaxis (Borba et al., 2021). In fold-change

detection, the response scales with the magnitude of the temporal change in sensory input, not the absolute value of the input (Adler and Alon, 2018). The presence of NMDA-Rs, but not AMPA-Rs, on the pr-AMG RNs fits well with a hypothesized modulatory role in this circuit.

The PR-II photoreceptors project only to the pr-AMG RNs. All of the PR-II photoreceptors are $VGAT^{+}$ (and thus likely inhibitory), with a subset being dual $VGLUT^{+}/VGAT^{+}$. Because their sole synaptic targets, the pr-AMG RNs, also appear to be inhibitory, we hypothesized that the dimming response was mediated by disinhibition, a hypothesis supported by pharmacology (Kourakis et al., 2019). However, the dual release of glutamate and GABA by a subset of the PR-II photoreceptors was not easily accounted for in the disinhibition model. Our finding here that the pr-AMG RNs do not express AMPA-Rs (Table 4.1, Figure 4.3), agrees well with the disinhibition model. In other words, glutamate could serve a modulatory role in the dimming response circuit, perhaps acting via GABA receptors, as has been shown previously (Marsden et al., 2007). Moreover, like the phototaxis behavior, the dimming response shows fold-change detection, although with a different putative circuit motif than in the phototaxis circuit (Borba et al., 2021), and modulation of GABA receptors could serve as the "memory" component of the fold-change detection circuit, as has been described for other systems showing fold-change detection (Lyashenko et al., 2020).

4.4.2 Glutamate receptors in the hindbrain

We previously reported that AMAPA-R transcripts are present asymmetrically in the hindbrain, with expression only obvious on the left side (Kourakis et al., 2021). By contrast, we report here that NMDA-R transcripts were observed equally in the left and right

hindbrain. However, while AMPA-R expression is predicted to be limited to the *motor ganglion paired descending interneurons* (MGINs), NMDA-R is more widely expressed, being observed in the Mauthner cell-like *descending decussating neurons* (ddNs) (Ryan et al., 2017) and the motor neurons (MNs; Table 4.1). The presence of glutamate receptors in the hindbrain initially appears to be paradoxical, as none of the AMPA-R and NMDA-R expressing hindbrain neurons appear to receive direct glutamatergic synaptic input. The primary inputs to the MGINs are from cholinergic and GABAergic relay neurons of the midbrain, (Kourakis et al., 2019; Ryan et al., 2016). While the ddNs only receive strong input from the peripheral nervous system, it is relayed by non-glutamatergic interneurons, such as the Eminens cells (Table 4.1). Dorsal to the MGINs, ddNs and motor neurons of the hindbrain are AMG neurons, which are among the primary synaptic targets of the glutamatergic peripheral sensory neurons (Ryan et al., 2018). Despite this, no glutamate receptor expression was observed in any of the AMG neurons (Table 4.1). However, the connectome predicts extensive electrical synapses between the peripheral sensory neurons and the AMGs, suggesting the transmission to the AMGs is not chemical. Nevertheless, since the peripheral sensory neurons are the only glutamatergic neurons to enter the hindbrain, we speculate that they may signal to the glutamate receptor-expressing hindbrain neurons extrasynaptically, which has been observed for glutamate signaling, and the distance between the peripheral sensory neuron termini and their putative hindbrain targets is well within the diffusion range of glutamate (Pál, 2018). Moreover, we speculated previously that the asymmetric expression of AMPA-R in the MGINs may account for the spiraling behavior of *Ciona* larvae when touched (Kourakis et al., 2021).

4.4.3 Kainate-R and mGluR expression

In addition to investigating the expression of AMPA-R and NMDA-R, we also examined kainate and metabotropic glutamate receptors. Kainate receptors are ionotropic and appear to have functions both pre- and post-synaptically (Contractor et al., 2011). We observed kainate-R expression in a distinct set of neurons in the posterior midbrain and neck (Table 4.1 and Figure 4.3). While we predict that one of the AntRNs is kainate-R^+, the function of the other kainate-R^+ neurons is not known. Of the three predicted mGluR, we only found evidence for expression of one of them (4.7.1), and only in peripheral sensory neurons (Figure 4.7). The function of this mGluR is not known, but we speculate that it may play a role in attenuation of the touch response.

4.5 Figures

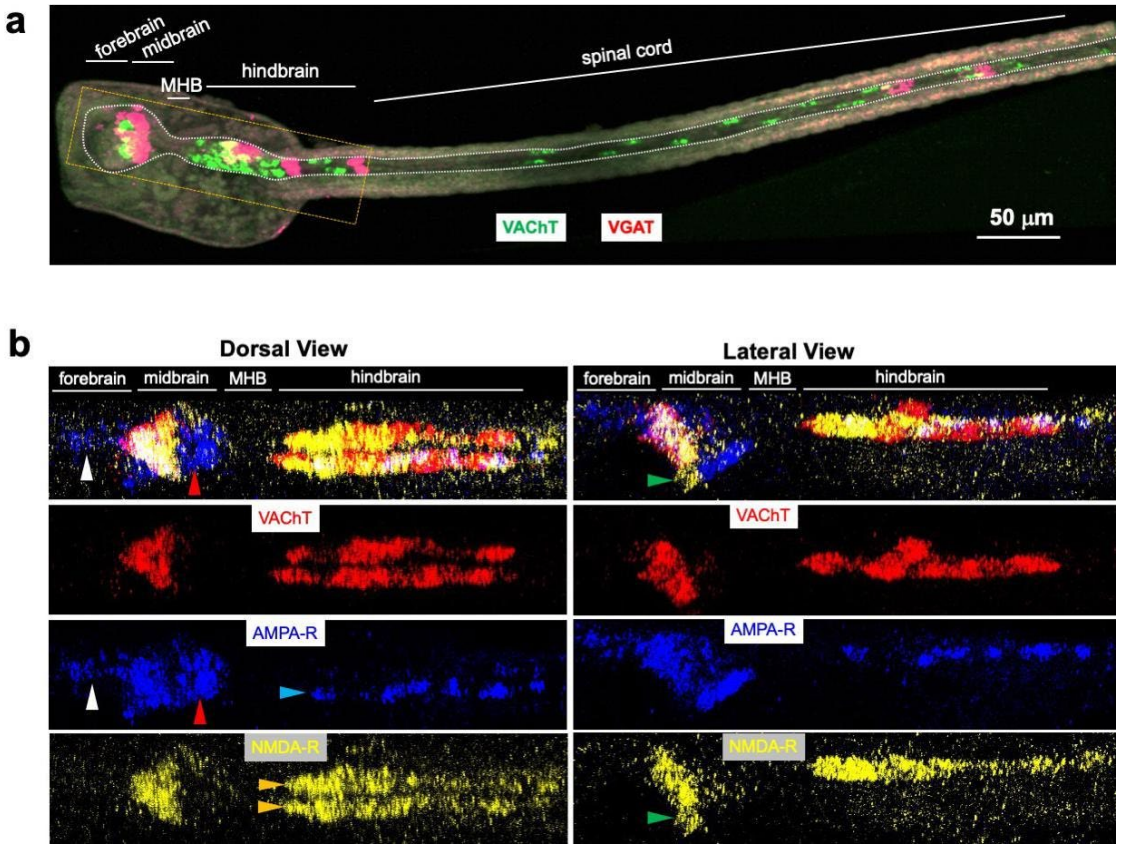

Figure 4.1. *In situ* hybridization of *C. robusta* larvae. (A) *In situ* hybridization of *C. robusta* larva for VAChT and VGAT. The major subdivisions of the central nervous system are labeled according to their vertebrate orthologs. The white line outlines the central nervous system, and the orange box outlines the approximate brain regions shown below in panel b. White arrows indicate midtail neurons. (B) *In situ* hybridization of *C. robusta* larva for VAChT, AMPA-R and NMDA-R. Top panels show dorsal and lateral composite views of the three expression patterns. The three lower right and left panels show the individual images that comprise the composite. White and red arrowheads indicate AMPA-R^+/NMDA-R^- forebrain and posterior midbrain neurons, respectively. Green arrowheads indicate NMDA-R^+/AMPA-R^- neurons. All images are Z-projection images from confocal stacks. Anterior is to the left for all panels.

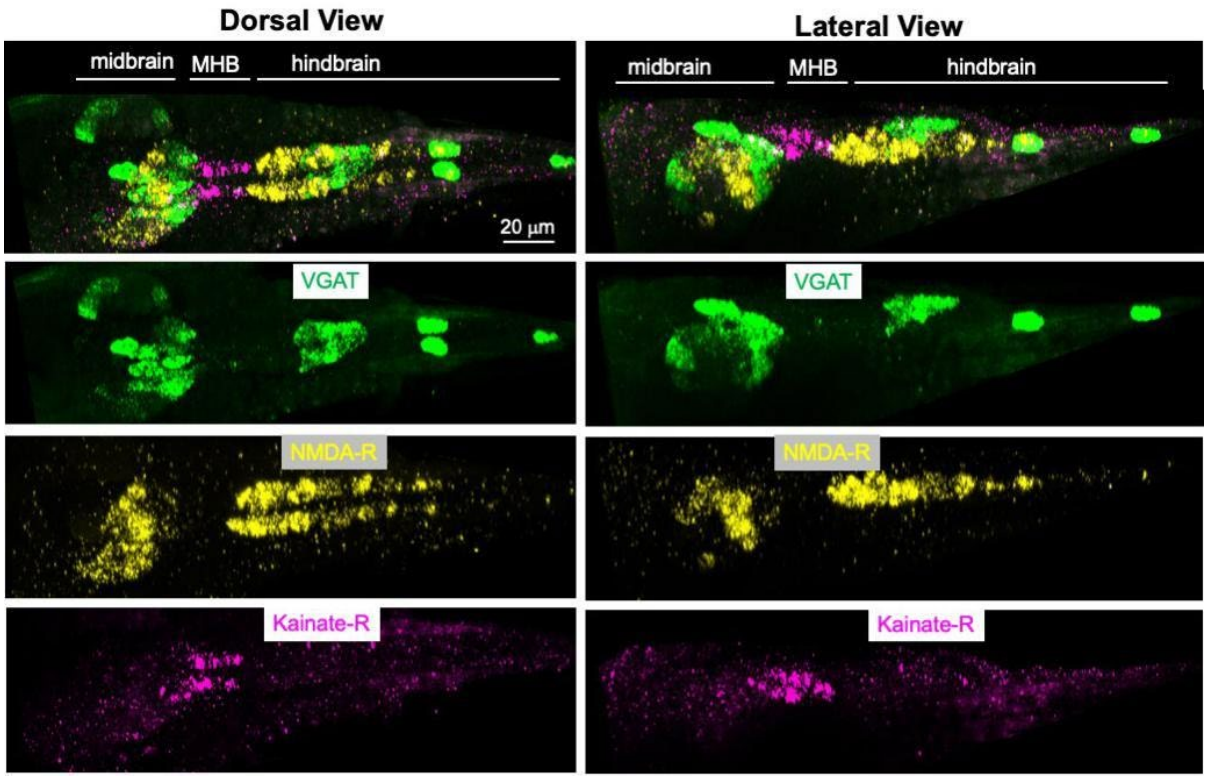

Figure 4.2 *In situ* hybridization of *C. robusta* larva for VGAT, NMDA-R, and Kainate-R. Top panels show dorsal and lateral composite views of the three expression patterns. The three lower right and left panels show the individual images that comprise the composite. White and red arrowheads indicate AMPA-R^+/NMDA-R^- forebrain and posterior midbrain neurons, respectively. Green arrowheads indicate NMDA-R^+/AMPA-R^- neurons. All images are Z-projection images from confocal stacks. Anterior is to the left for all panels. MHB, midbrain hindbrain boundary.

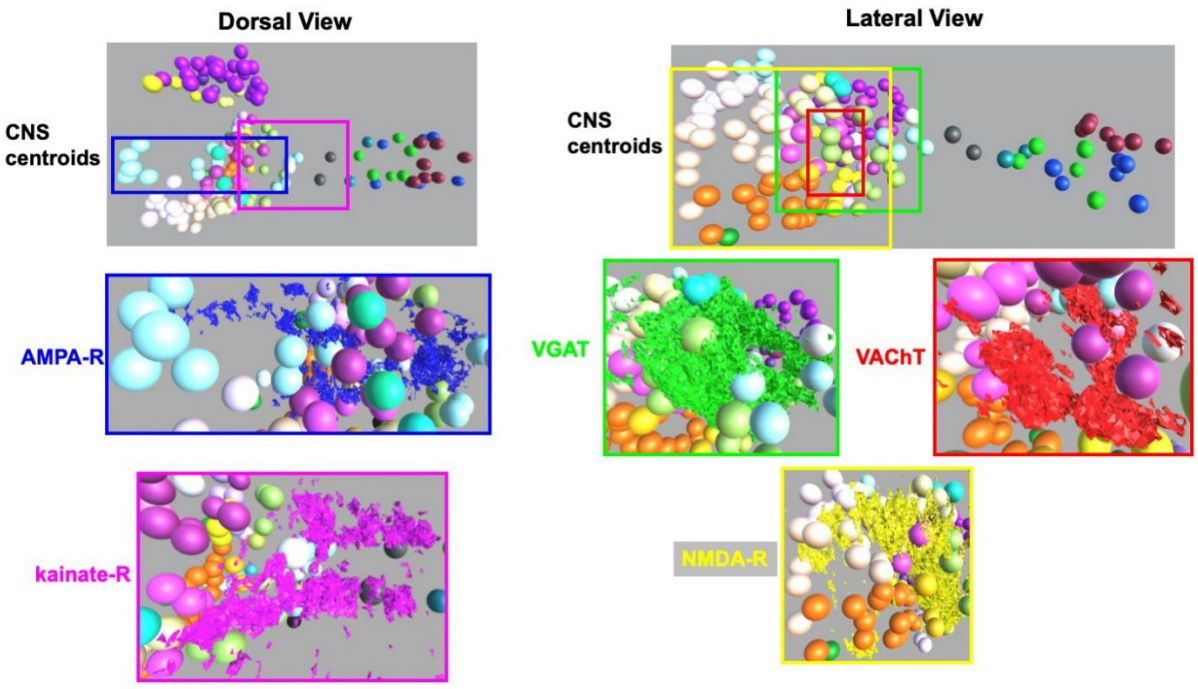

Figure 4.2.1 Mapping of *in situ* hybridization expression patterns to neuron centroids of the connectome. The two top panels show forebrain to hindbrain neuron centroids given by (Ryan et al., 2016), and are colored by neurons class according to (Ryan and Meinertzhagen, 2019), see Figure 4.2.2. The lower panels show registration of *in situ* hybridization signals for the indicated transcripts with the connectome centroids.

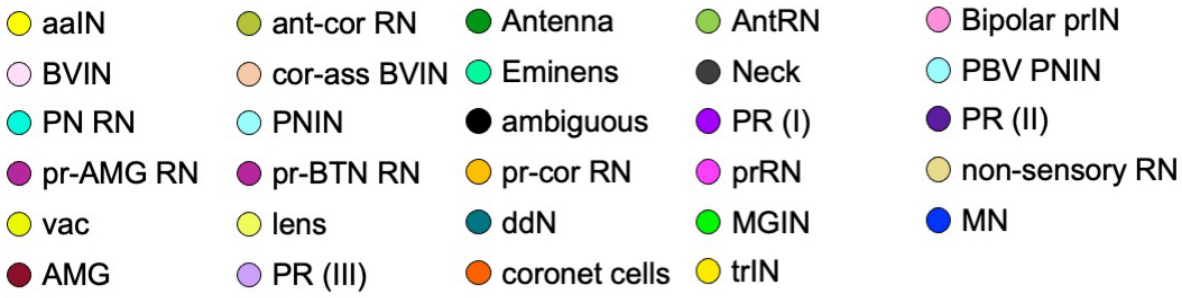

Figure 4.2.2. Key to neuron classification as given by (Ryan and Meinertzhagen, 2019).

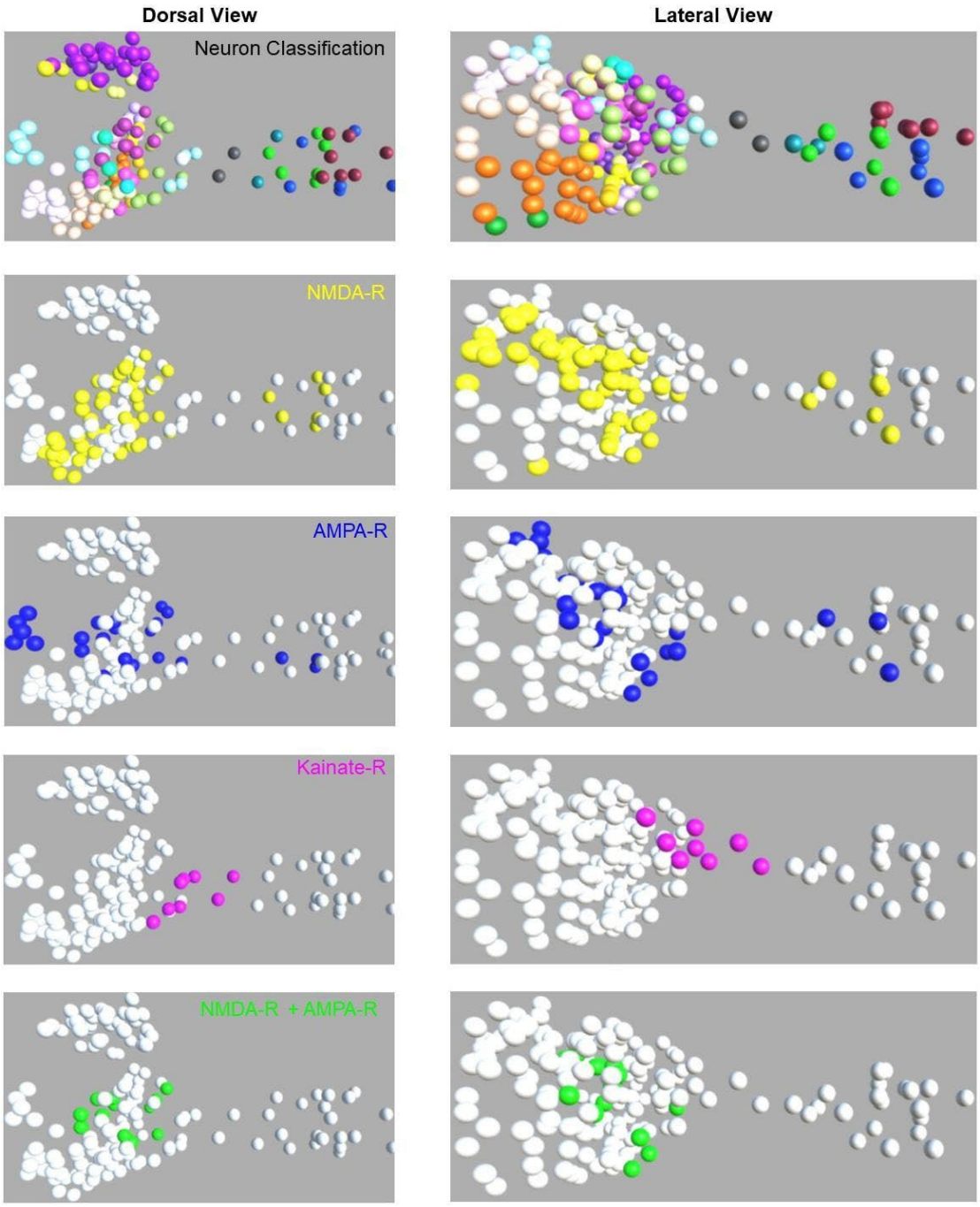

Figure 4.3. Summary of glutamatergic receptor expression. The two top panels show forebrain to hindbrain neuron centroids given by (Ryan et al., 2016) and are colored by neurons class according to (Ryan and Meinertzhagen, 2019), see Figure 4.2.2. The bottom panels show the predicted distribution of AMPA, NMDA and kainate receptors at larval stage.

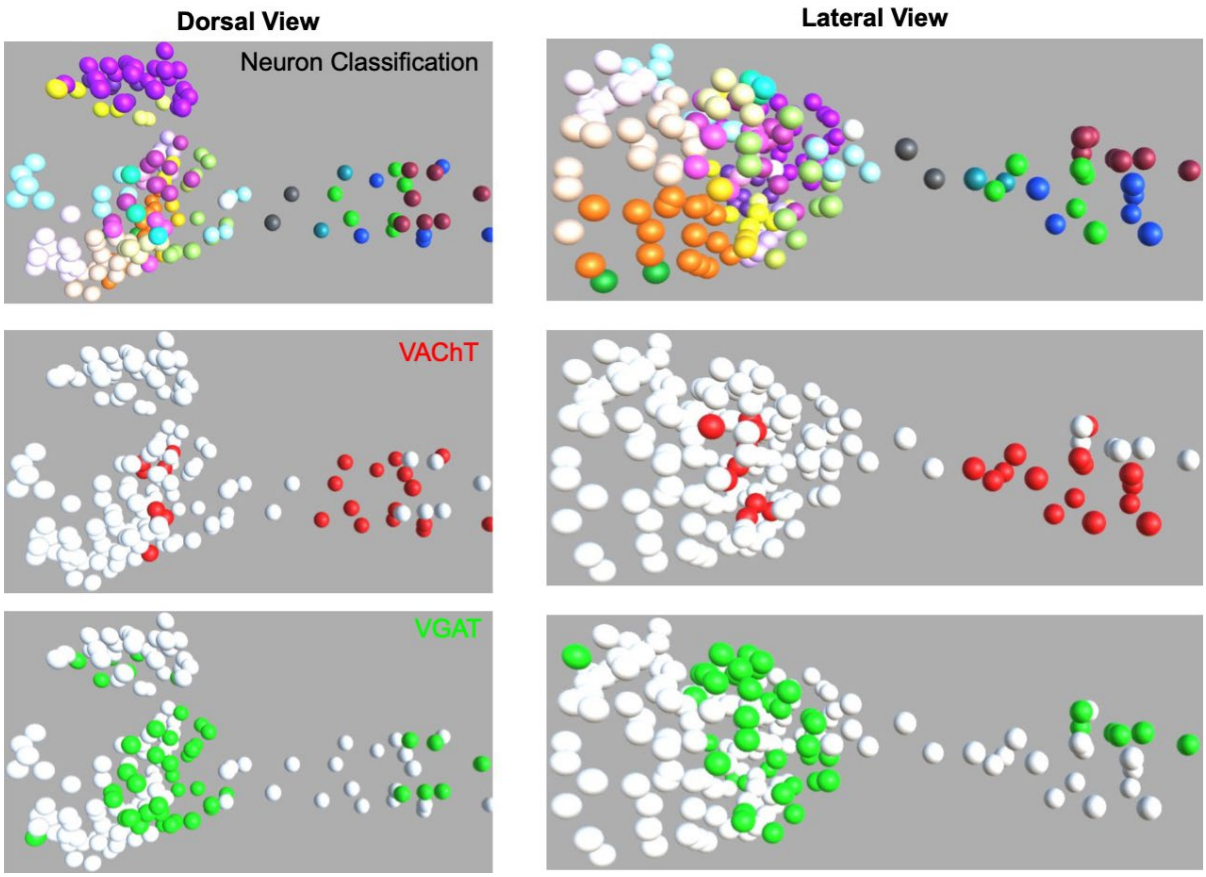

Figure 4.4. Summary of VAChT and VGAT expression. The two top panels show forebrain to hindbrain neuron centroids given by (Ryan et al., 2016), and are colored by neurons class according to (Ryan and Meinertzhagen, 2019), see Figure 4.2.2. The bottom panels show the predicted distribution of VAChT and VGAT at the larval stage.

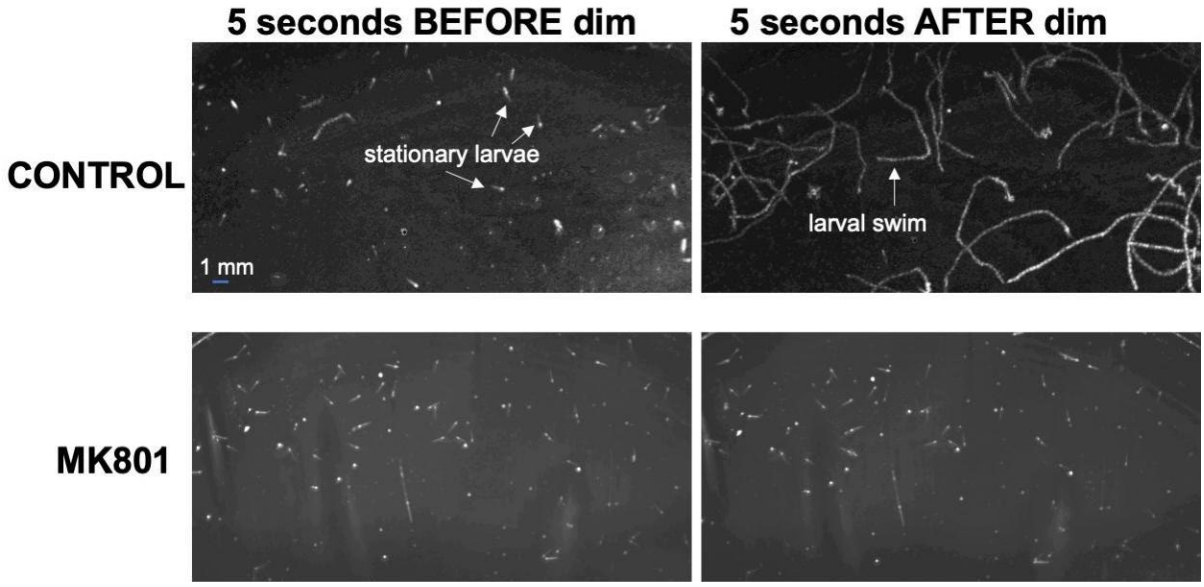

Figure 4.5. MK801 Blocks the dimming response. The left two panels show *Ciona* larvae in a temporal projection of the 5 seconds before light dimming for both control and MK801-treated larvae. Lines represent larval paths in 5 second projection. Most larvae are stationary. In the five seconds following light dimming the CONTROL larvae are observed swimming (white lines), while the MK801-treated larvae do not respond.

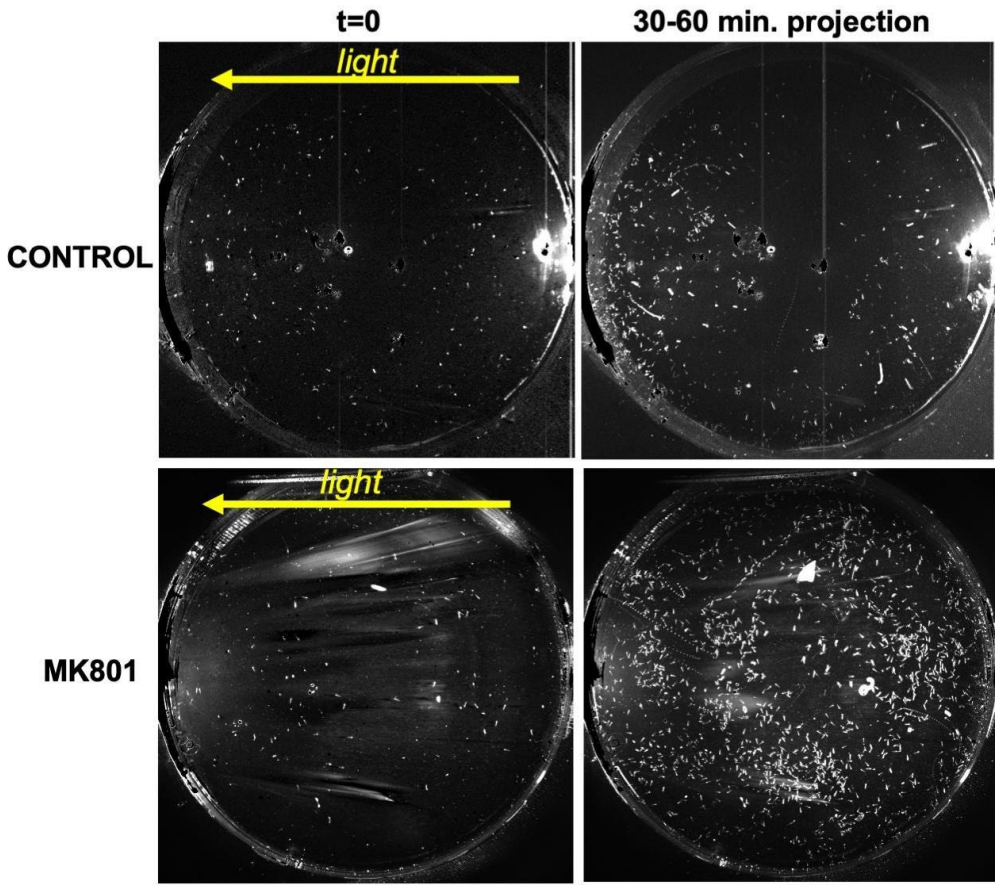

Figure 4.6. MK801 Blocks the dimming response. The left two panels show the first frame of the phototaxis assay with the yellow arrow indicating the direction of the light. The right two panels show temporal projects from 30 minutes to 60 minutes in directional light. Larvae can be seen accumulated on the left in the control and more dispersed in the MK801-treated.

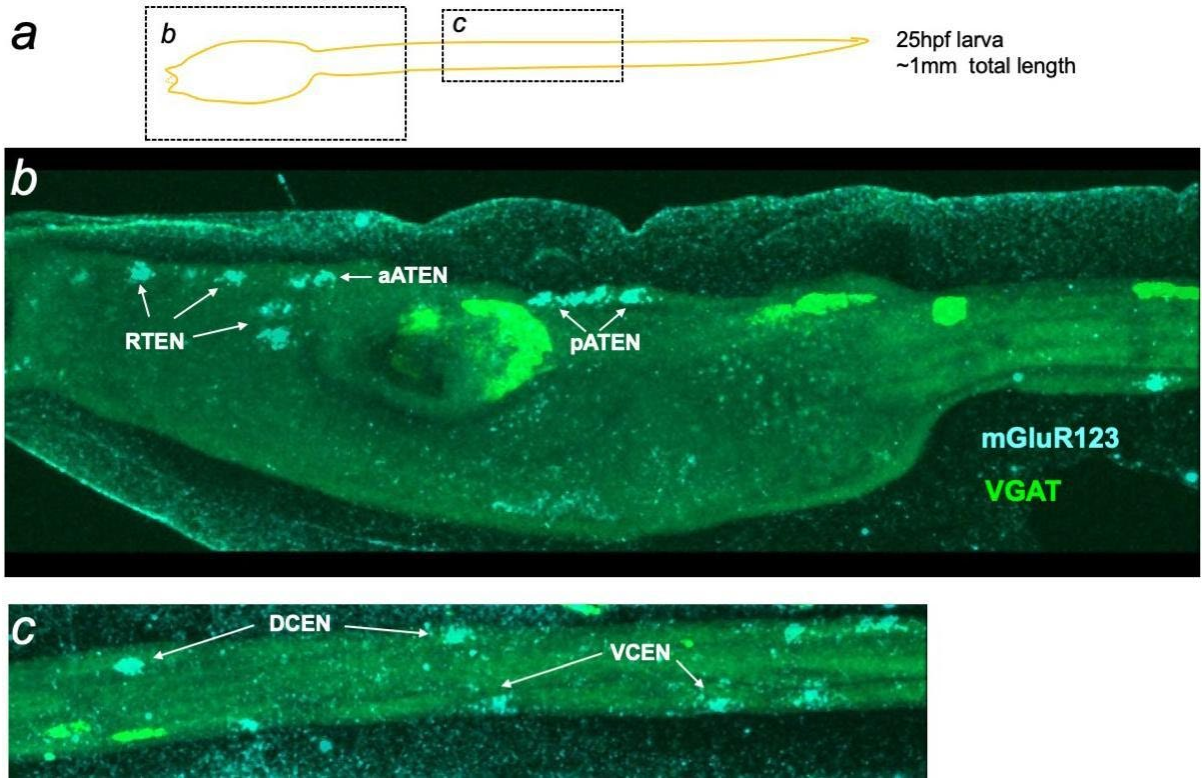

Figure 4.7. Expression of mGluR123 by *in situ* hybridization. (A) Cartoon of *Ciona* larva indicating regions shown in panels B and C. (B) mGluR123 expression in the trunk of a *Ciona* larva. Arrows point to mGluR123-expressing epidermal sensory neurons. Abbreviations: RTEN, rostral trunk epidermal neurons; aATEN, anterior apical trunk epidermal neurons; pATEN posterior apical trunk epidermal neurons. (C) mGluR123 expression in the tail of a *Ciona* larva. Abbreviations: DCEN, dorsal caudal epidermal neurons; VCEN and ventral caudal epidermal neurons.

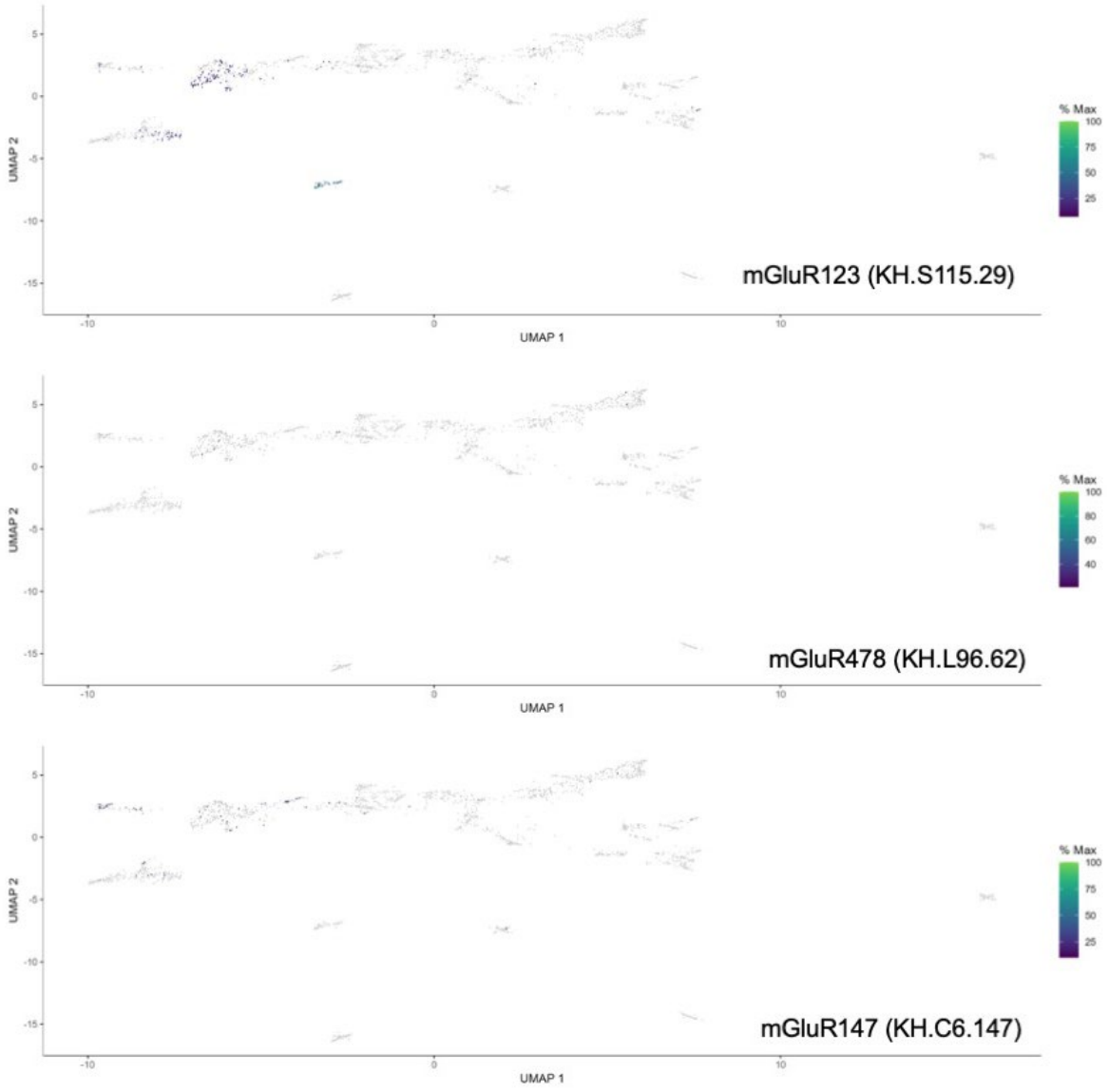

Figure 4.7.1. Clustering of Ciona larval scRNAseq with superimposed expression of mGlu receptors. Dataset from (Cao et al., 2019) and collected using Python.

4.6 Table

Table 4.1. Predicted expression results from Unity software of VGAT, VAChT, AMPA-R, NMDA-R and kainate-R in neurons of the *Ciona* larva as given by the connectome (Ryan et al., 2016).

Cell ID	Cell Type	VGAT+	VAChT	NMDAR+	KainateR+	AMPAR+
95	aaIN	0	+	+	0	0
102	aaIN	0	+	+	0	0
115	aaIN	0	+	+	0	0
ACIN1L	ACIN	+	0	+	0	0
AMG1	AMG	+	0	0	0	0
AMG2	AMG	+	0	0	0	0
AMG3	AMG	+	0	0	0	0
AMG4	AMG	+	0	0	0	0
AMG5	AMG	0	+	0	0	0
AMG6	AMG	+	0	0	0	0
AMG7	AMG	+	0	0	0	0
120	ant-cor RN	+	0	+	0	+
Ant1	Antenna	0	0	0	0	0
Ant2	Antenna	0	0	+	0	0
134	AntRN	+	0	+	0	0
135	AntRN	+	0	+	0	0
142	AntRN	+	0	+	0	+
143	AntRN	+	0	0	0	+
147	AntRN	+	0	+	0	+
152	AntRN	+	0	+	0	+
153	AntRN	+	0	+	0	0
159	AntRN	+	0	0	+	0
161	AntRN	+	0	0	0	+
90	Bipolar prIN	0	+	+	0	+
92	Bipolar prIN	0	+	+	0	+
3	BVIN	0	0	0	0	0
13	BVIN	+	0	0	0	0
16	BVIN	0	0	0	0	0
18	BVIN	0	0	+	0	0
21	BVIN	0	0	0	0	0
22	BVIN	0	0	0	0	0
24	BVIN	0	0	+	0	0
33	BVIN	0	0	+	0	0
41	BVIN	0	0	+	0	0
42	BVIN	0	0	+	0	0
43	BVIN	0	0	+	0	0
46	BVIN	0	0	0	0	0
138	BVIN	0	0	0	0	0
1	cor-ass BVIN	0	0	+	0	0
2	cor-ass BVIN	0	0	+	0	0
15	cor-ass BVIN	0	0	0	0	0
17	cor-ass BVIN	0	0	0	0	0
23	cor-ass BVIN	0	0	+	0	0
38	cor-ass BVIN	0	0	+	0	0
48	cor-ass BVIN	0	0	+	0	0
50	cor-ass BVIN	0	0	+	0	0
55	cor-ass BVIN	0	0	+	0	0
59	cor-ass BVIN	0	0	+	0	0
60	cor-ass BVIN	0	0	0	0	0
62	cor-ass BVIN	0	0	0	0	0

68	cor-ass BVIN	0	0	0	0	0
70	cor-ass BVIN	0	0	+	0	0
73	cor-ass BVIN	0	0	+	0	0
78	cor-ass BVIN	0	0	0	0	0
79	cor-ass BVIN	0	0	+	0	0
coronet 1	Coronet	0	0	0	0	0
coronet 10	Coronet	0	0	0	0	0
coronet 11	Coronet	0	0	0	0	0
coronet 12	Coronet	0	0	0	0	0
coronet 13	Coronet	0	0	0	0	0
coronet 14	Coronet	0	0	0	0	0
coronet 15	Coronet	0	0	0	0	0
coronet 16	Coronet	0	0	0	0	0
coronet 2	Coronet	0	0	0	0	0
coronet 3	Coronet	0	0	0	0	0
coronet 4	Coronet	0	0	0	0	0
coronet 5	Coronet	0	0	0	0	0
coronet 6	Coronet	0	0	0	0	0
coronet 7	Coronet	0	0	0	0	0
coronet 8	Coronet	0	0	0	0	0
coronet 9	Coronet	0	0	0	0	0
ddNL	ddN	0	+	+	0	0
ddNR	ddN	0	+	+	0	0
99	Eminens	+	0	0	0	0
109	Eminens	+	0	0	0	0
MGIN1L	MGIN	0	+	+	0	+
MGIN1R	MGIN	0	+	+	0	0
MGIN2L	MGIN	0	+	+	0	+
MGIN2R	MGIN	0	+	+	0	0
MGIN3L	MGIN	0	+	+	0	+
MGIN3R	MGIN	0	+	+	0	0
MN1L	MN	0	+	+	0	0
MN1R	MN	0	+	+	0	0
MN2L	MN	0	+	+	0	0
MN2R	MN	0	+	+	0	0
MN3L	MN	0	+	+	0	0
MN3R	MN	0	+	+	0	0
MN4L	MN	0	+	+	0	0
MN4R	MN	0	+	+	0	0
MN5L	MN	0	+	+	0	0
MN5R	MN	0	+	+	0	0
165	Neck	0	0	0	+	0
166	Neck	0	0	0	+	0
160	PBV PNIN	+	0	0	+	0
162	PBV PNIN	+	0	0	+	0
163	PBV PNIN	0	0	0	+	0
164	PBV PNIN	0	0	0	+	0
131	PN RN	+	0	0	0	0
4	PNIN	0	0	0	0	+
6	PNIN	0	0	0	0	+
20	PNIN	0	0	0	0	+
25	PNIN	0	0	0	0	+
29	PNIN	0	0	0	0	+
30	PNIN	0	0	0	0	+
61	PNIN	0	0	+	0	+
65	PNIN	0	0	+	0	+
85	PNIN	0	+	+	0	+
88	PNIN	0	+	+	0	+
107	ambiguous cells	0	0	+	0	0
177	ambiguous cells	0	0	0	+	0
pr1	PR (I)	0	0	0	0	0
pr10	PR (I)	+	0	0	0	0

pr11	PR (I)	0	0	0	0	0
pr12	PR (I)	0	0	0	0	0
pr13	PR (I)	0	0	0	0	0
pr14	PR (I)	0	0	0	0	0
pr15	PR (I)	0	0	0	0	0
pr16	PR (I)	0	0	0	0	0
pr17	PR (I)	0	0	0	0	0
pr18	PR (I)	0	0	0	0	0
pr19	PR (I)	0	0	0	0	0
pr2	PR (I)	0	0	0	0	0
pr20	PR (I)	0	0	0	0	0
pr21	PR (I)	0	0	0	0	0
pr22	PR (I)	0	0	0	0	0
pr23	PR (I)	0	0	0	0	0
pr3	PR (I)	0	0	0	0	0
pr4	PR (I)	0	0	0	0	0
pr5	PR (I)	0	0	0	0	0
pr6	PR (I)	0	0	0	0	0
pr7	PR (I)	0	0	0	0	0
pr8	PR (I)	0	0	0	0	0
pr9	PR (I)	+	0	0	0	0
pr-a	PR (II)	+	0	0	0	0
pr-b	PR (II)	+	0	0	0	0
pr-c	PR (II)	+	0	0	0	0
pr-d	PR (II)	+	0	0	0	0
pr-e	PR (II)	+	0	0	0	0
pr-f	PR (II)	+	0	0	0	0
pr-g	PR (II)	+	0	0	0	0
101	PR (III)	0	0	0	0	0
110	PR (III)	0	0	0	0	0
113	PR (III)	0	0	0	0	0
114	PR (III)	0	0	0	0	0
lens6	PR (III)	0	0	0	0	0
lens7	PR (III)	0	0	0	0	0
84	PR (III)	0	0	0	0	0
74	pr-AMG RN	+	0	+	0	0
94	pr-AMG RN	+	0	+	0	0
108	pr-AMG RN	0	0	+	0	0
116	pr-AMG RN	0	0	+	0	0
124	pr-AMG RN	+	0	0	0	0
127	pr-AMG RN	+	0	+	0	0
140	pr-AMG RN	+	0	+	0	0
157	pr-AMG RN	+	0	0	0	0
123	pr-BTN RN	0	+	+	0	0
130	pr-BTN RN	0	0	+	0	0
105	pr-cor RN	0	0	+	0	0
112	pr-cor RN	0	0	+	0	0
119	pr-cor RN	0	0	+	0	0
80	prRN	+	0	0	0	0
86	prRN	0	0	+	0	+
96	prRN	0	+	+	0	+
100	prRN	0	+	+	0	0
121	prRN	0	+	+	0	+
126	prRN	0	+	+	0	+
93	non-sensory RN	+	0	0	0	0
103	non-sensory RN	+	0	0	0	0
106	non-sensory RN	+	0	0	0	0
122	non-sensory RN	+	0	0	0	0
125	non-sensory RN	+	0	0	0	0
trIN	trIN	0	0	0	0	0
vacIN1	vacIN	0	0	0	0	0
vacIN2	vacIN	0	0	0	0	0

5. CONCLUSION

My dissertation studies, which build on earlier work on the *Ciona* connectome, has led to novel models for neural circuits and behavior. The significance of my findings is greater when you take into consideration that the published *Ciona* connectome is the only representative of not only a chordate, but of a deuterostome connectome. My studies with the PR-I and PR-II circuits has led to greater understanding of visual processing mechanisms. These mechanisms can form the basis of investigations of other sensory systems, as well as mechanisms of multisensory integration. For example, my initial studies on the PR-II disinhibitory circuit lead to our modeling in three-dimensional space of gravitaxis as triggered by the dim response (Bostwick et al., 2020). Nevertheless, there are many remaining questions about these parallel visuomotor circuits. I will highlight some of these unknowns below.

Both Group I and II photoreceptors are primarily glutamatergic, but with most of PR-II being dual glutamatergic/GABAergic. Interestingly, while the connectome shows that the photoreceptors are highly interconnected, none of them express glutamate receptors. In chapter 2, I established that the PR-I neurons are working through glutamate, which was evident when blocking glutamate receptors with an AMPA-receptor antagonist led to an extinction in phototaxis behavior. The existence of glutamate receptors in the photoreceptor relay neurons, the primary target of the photoreceptors, strongly supports the glutamate use from the photoreceptors. However, what neurotransmitter receptors are the photoreceptors using to communicate with each other? The connectome shows that PR-I and -II are highly interconnected with chemical synapses, with almost no electrical synapses (Figures 2.1.1-2). This suggests that PR-I use a second neurotransmitter for interphotoreceptor communication.

This is further supported by the expression of adrenergic receptors in PR-I (Figure 3.4), suggesting expression of a catecholamine neurotransmitter that binds to these receptors. PR-II photoreceptors communicate with relay neurons through GABA via the $GABA_A$ receptor, as I demonstrated by blocking the $GABA_A$ receptor with picrotoxin, which led to a decrease in the dim response (Figures 2.6 and 2.7). However, whether $GABA_A$ receptors are used to communicate within the photoreceptors needs to be investigated. In summary, the receptors utilized by PR-I or -II for intragroup communication remains a mystery.

Chapter 3 presented a model processing neuronal circuit level of fold-change detection highlighting the synaptic connections between the prRNs and pr-AMG RNs; however, the cellular mechanisms and dynamics of this process are still unknown. For example, what are the receptors being utilized and how are they determining the appropriate FCD output? One poorly understood feature of the FCD circuit is the "memory component". A FCD system needs to make a transient memory of its initial state to be able to compare it to a new state to process the fold-change difference. It is thought that the memory component is integral to the modulator (Adler and Alon, 2018); however, the cellular mechanisms generating the memory appear to be variable and, in most cases, not well described. The expression of NMDA-R in prRNs and pr-AMG RNs suggests these receptors may have a role in memory formation, since they have well documented modulatory function. Further gene expression studies done in the pBV may reveal neuron-specific properties that can assist in our understanding of sensory processing.

The role of NMDA-R in other possible sensory processing is another remaining question. Most of the focus of this dissertation has been on two sensory systems and their associated behavior (dim response and phototaxis). However, as mentioned previously, the

Ciona larvae also exhibit other behaviors, such as gravitaxis and mechanosensation. The sensory neurons driving these behaviors are also glutamatergic, possibly tying the role of NMDA-R to varying mechanisms of sensory processing from all systems [except the coronet cells - which appear to be dopaminergic (Lemaire et al., 2021; Moret et al., 2005b, 2005a)].

Another behavior *Ciona* has been speculated to have, but is controversial, is the detection of hydrostatic pressure. The few studies that investigated this possibility reported no noticeable behavioral response when larvae were exposed to immediate changes in pressure (Tsuda et al., 2003a), with one exception that reported a pressure response when the larvae were 1.5 hour post hatching (Spagnuolo and Palladino). I investigated the possibility that *Ciona* may detect hydrostatic pressure using a prototype pressure chamber, pressurized to about 18.3 PSI (equivalent to the hydrostatic pressure at 2.5 m). My preliminary result was that the 25 hpf larvae left alone in the pressurized chamber for 5 minutes were more distributed, depth-wise, as opposed to the unpressurized control, which all sank and remained at the bottom. The larvae are denser than water and tend to just sink (Bostwick et al., 2020), however, all our experiments are done in shallow water (6 or 10 cm petri dishes). This result suggests the larvae are detecting the higher hydrostatic pressure and are interpreting it as being deeper in the water than they currently are. In response to this, the larvae are potentially attempting to maintain a shallower level in the chamber, resulting in a larger distribution. This hypothesis, however, requires further investigation.

The completion of the connectome has propelled the *Ciona* larva forward as a system to study neural circuits and behavior. Overall, the established research tools along with the availability of the *Ciona* connectome has furthered our understanding of visuomotor circuits in a chordate. Studying neural circuits with the granular detail (*i.e.*, role of individual neurons

and synaptic signaling mechanisms) explored in this dissertation help us gain a fundamental understanding of how neuronal circuits produce behavior. These studies may serve as a stepping stone to investigate animals with large, complex brains, such as humans or mice. Referring back to Marder's quote, we have the necessary details of how these neurons are connected, and now, we must continue working to gain the sufficient details to understand how they work.

6. REFERENCES

Adler, M., and Alon, U. (2018). Fold-change detection in biological systems. Curr. Opin. Syst. Biol. *8*, 81–89. .

Adler, M., Szekely, P., Mayo, A., and Alon, U. (2017). Optimal Regulatory Circuit Topologies for Fold-Change Detection. Cell Syst. *4*, 171-181.e8. https://doi.org/10.1016/j.cels.2016.12.009.

Alon, U. (2007). Network motifs: theory and experimental approaches. Nat Rev Genet *8*, 450–461. https://doi.org/10.1038/nrg2102.

Arendt, D. (2003). Evolution of eyes and photoreceptor cell types. Int J Dev Biol *47*, 563–571. .

Beg, A.A., and Jorgensen, E.M. (2003). EXP-1 is an excitatory GABA-gated cation channel. Nat Neurosci *6*, 1145–1152. https://doi.org/10.1038/nn1136.

Boorman, C.J., and Shimeld, S.M. (2002). Pitx homeobox genes in Ciona and amphioxus show left-right asymmetry is a conserved chordate character and define the ascidian adenohypophysis. Evol. Dev. *4*, 354–365. https://doi.org/10.1046/j.1525-142x.2002.02021.x.

Borba, C., Kourakis, M.J., Schwennicke, S., Brasnic, L., and Smith, W.C. (2021). Fold Change Detection in Visual Processing. Front. Neural Circuits *15*, 705161. https://doi.org/10.3389/fncir.2021.705161.

Bostwick, M., Smith, E.L., Borba, C., Newman-Smith, E., Guleria, I., Kourakis, M.J., and Smith, W.C. (2020). Antagonistic Inhibitory Circuits Integrate Visual and Gravitactic Behaviors. Curr. Biol. *30*, 600-609.e2. https://doi.org/10.1016/j.cub.2019.12.017.

Boyl, P.P., Signore, M., Annino, A., Barbera, J.P.M., Acampora, D., and Simeone, A. (2001). Otx genes in the development and evolution of the vertebrate brain. Int. J. Dev. Neurosci. *19*, 353–363. https://doi.org/10.1016/S0736-5748(01)00003-X.

Brown, E.R., Nishino, A., Bone, Q., Meinertzhagen, I.A., and Okamura, Y. (2005). GABAergic synaptic transmission modulates swimming in the ascidian larva. Eur J Neurosci *22*, 2541–2548. https://doi.org/10.1111/j.1460-9568.2005.04420.x.

Burkhardt, D.A. (1994). Light adaptation and photopigment bleaching in cone photoreceptors in situ in the retina of the turtle. J. Neurosci. *14*, 1091–1105. https://doi.org/10.1523/JNEUROSCI.14-03-01091.1994.

Callaway, E.M. (2005). Structure and function of parallel pathways in the primate early visual system. J Physiol *566*, 13–19. https://doi.org/10.1113/jphysiol.2005.088047.

Cañestro, C., Bassham, S., and Postlethwait, J. (2005). Development of the central nervous system in the larvacean Oikopleura dioica and the evolution of the chordate brain. Dev. Biol. *285*, 298–315. https://doi.org/10.1016/j.ydbio.2005.06.039.

Cao, C., Lemaire, L.A., Wang, W., Yoon, P.H., Choi, Y.A., Parsons, L.R., Matese, J.C., Wang, W., Levine, M., and Chen, K. (2019). Comprehensive single-cell transcriptome lineages of a proto-vertebrate. Nature *571*, 349–354. https://doi.org/10.1038/s41586-019-1385-y.

Choi, H.M.T., Schwarzkopf, M., Fornace, M.E., Acharya, A., Artavanis, G., Stegmaier, J., Cunha, A., and Pierce, N.A. (2018). Third-generation in situ hybridization chain reaction: multiplexed, quantitative, sensitive, versatile, robust. Development *145*. https://doi.org/10.1242/dev.165753.

Christiaen, L., Burighel, P., Smith, W.C., Vernier, P., Bourrat, F., and Joly, J.-S. (2002). Pitx genes in Tunicates provide new molecular insight into the evolutionary origin of pituitary. Gene *287*, 107–113. https://doi.org/10.1016/S0378-1119(01)00865-4.

Cole, A.G., and Meinertzhagen, I.A. (2004). The central nervous system of the ascidian larva: mitotic history of cells forming the neural tube in late embryonic Ciona intestinalis. Dev. Biol. *271*, 239–262. https://doi.org/10.1016/j.ydbio.2004.04.001.

Contractor, A., Mulle, C., and Swanson, G.T. (2011). Kainate receptors coming of age: milestones of two decades of research. Trends Neurosci. *34*, 154–163. https://doi.org/10.1016/j.tins.2010.12.002.

Corbo, J.C., Levine, M., and Zeller, R.W. (1997). Characterization of a notochord-specific enhancer from the Brachyury promoter region of the ascidian, Ciona intestinalis. Development *124*, 589–602. .

Dehal, P., and Boore, J.L. (2005). Two rounds of whole genome duplication in the ancestral vertebrate. PLoS Biol. *3*, e314. https://doi.org/10.1371/journal.pbio.0030314.

Delsuc, F., Brinkmann, H., Chourrout, D., and Philippe, H. (2006). Tunicates and not cephalochordates are the closest living relatives of vertebrates. Nature *439*, 965–968. https://doi.org/10.1038/nature04336.

Deschet, K., and Smith, W.C. (2004). Frimousse – a spontaneous ascidian mutant with anterior ectodermal fate transformation. Curr. Biol. *14*, R408–R410. https://doi.org/10.1016/j.cub.2004.05.029.

Deschet, K., Nakatani, Y., and Smith, W.C. (2003). Generation of Ci-Brachyury-GFP stable transgenic lines in the ascidian Ciona savignyi. Genesis *35*, 248–259. https://doi.org/10.1002/gene.10195.

Dunn, F.A., Lankheet, M.J., and Rieke, F. (2007). Light adaptation in cone vision involves switching between receptor and post-receptor sites. Nature *449*, 603–606. https://doi.org/10.1038/nature06150.

Eakin, R.M., and Kuda, A. (1971). Ultrastructure of sensory receptors in Ascidian tadpoles. Z Zellforsch Mikrosk Anat *112*, 287–312. .

Eichler, K., Li, F., Litwin-Kumar, A., Park, Y., Andrade, I., Schneider-Mizell, C.M., Saumweber, T., Huser, A., Eschbach, C., Gerber, B., et al. (2017). The complete connectome of a learning and memory centre in an insect brain. Nature *548*, 175–182. https://doi.org/10.1038/nature23455.

Esposito, R., Yasuo, H., Sirour, C., Palladino, A., Spagnuolo, A., and Hudson, C. (2017). Patterning of brain precursors in ascidian embryos. Development *144*, 258–264. https://doi.org/10.1242/dev.142307.

Fabian-Fine, R., Meisner, S., Torkkeli, P.H., and Meinertzhagen, I.A. (2015). Co-localization of Gamma-Aminobutyric Acid and Glutamate in Neurons of the Spider Central Nervous System. Cell Tissue Res *362*, 461–479. https://doi.org/10.1007/s00441-015-2241-5.

Fattorini, G., Antonucci, F., Menna, E., Matteoli, M., and Conti, F. (2015). Co-expression of VGLUT1 and VGAT sustains glutamate and GABA co-release and is regulated by activity in cortical neurons. J Cell Sci *128*, 1669–1673. https://doi.org/10.1242/jcs.164210.

Geramita, M.A., Burton, S.D., and Urban, N.N. (2016). Distinct lateral inhibitory circuits drive parallel processing of sensory information in the mammalian olfactory bulb. Elife *5*. https://doi.org/10.7554/eLife.16039.

Goentoro, L., Shoval, O., Kirschner, M.W., and Alon, U. (2009). The Incoherent Feedforward Loop Can Provide Fold-Change Detection in Gene Regulation. Mol. Cell *36*, 894–899. https://doi.org/10.1016/j.molcel.2009.11.018.

Gorman, A.L., McReynolds, J.S., and Barnes, S.N. (1971). Photoreceptors in primitive chordates: fine structure, hyperpolarizing receptor potentials, and evolution. Science *172*, 1052–1054. .

Grave, C. (1920). Amaroucium pellucidum (Leidy) form constellatum (Verrill) I. The activities and reactions of the tadpole larva. J Exp Zool *30*, 239–257. .

Hackley, C., Mulholland, E., Kim, G.J., Newman-Smith, E., and Smith, W.C. (2013). A transiently expressed connexin is essential for anterior neural plate development in Ciona intestinalis. Development *140*, 147–155. https://doi.org/10.1242/dev.084681.

Hamada, M., Shimozono, N., Ohta, N., Satou, Y., Horie, T., Kawada, T., Satake, H., Sasakura, Y., and Satoh, N. (2011). Expression of neuropeptide- and hormone-encoding genes in the Ciona intestinalis larval brain. Dev. Biol. *352*, 202–214. https://doi.org/10.1016/j.ydbio.2011.01.006.

Hanada, T., Hashizume, Y., Tokuhara, N., Takenaka, O., Kohmura, N., Ogasawara, A., Hatakeyama, S., Ohgoh, M., Ueno, M., and Nishizawa, Y. (2011). Perampanel: a novel, orally active, noncompetitive AMPA-receptor antagonist that reduces seizure activity in rodent models of epilepsy. Epilepsia *52*, 1331–1340. https://doi.org/10.1111/j.1528-1167.2011.03109.x.

Hashimoto, H., Robin, F.B., Sherrard, K.M., and Munro, E.M. (2015). Sequential Contraction and Exchange of Apical Junctions Drives Zippering and Neural Tube Closure in a Simple Chordate. Dev. Cell *32*, 241–255. https://doi.org/10.1016/j.devcel.2014.12.017.

Hirai, S., Hotta, K., Kubo, Y., Nishino, A., Okabe, S., Okamura, Y., and Okado, H. (2017). AMPA glutamate receptors are required for sensory-organ formation and morphogenesis in the basal chordate. Proc Natl Acad Sci U A *114*, 3939–3944. https://doi.org/10.1073/pnas.1612943114.

Hironaka, K., and Morishita, Y. (2014). Cellular Sensory Mechanisms for Detecting Specific Fold-Changes in Extracellular Cues. Biophys. J. *106*, 279–288. https://doi.org/10.1016/j.bpj.2013.10.039.

Holland, L.Z. (2015). ca. Philos. Trans. R. Soc. B Biol. Sci. *370*, 20150048. https://doi.org/10.1098/rstb.2015.0048.

Horie, T., Orii, H., and Nakagawa, M. (2005). Structure of ocellus photoreceptors in the ascidian Ciona intestinalis larva as revealed by an anti-arrestin antibody. J Neurobiol *65*, 241–250. https://doi.org/10.1002/neu.20197.

Horie, T., Sakurai, D., Ohtsuki, H., Terakita, A., Shichida, Y., Usukura, J., Kusakabe, T., and Tsuda, M. (2008a). Pigmented and nonpigmented ocelli in the brain vesicle of the ascidian larva. J Comp Neurol *509*, 88–102. https://doi.org/10.1002/cne.21733.

Horie, T., Kusakabe, T., and Tsuda, M. (2008b). Glutamatergic networks in the Ciona intestinalis larva. J Comp Neurol *508*, 249–263. https://doi.org/10.1002/cne.21678.

Horie, T., Nakagawa, M., Sasakura, Y., and Kusakabe, T.G. (2009). Cell type and function of neurons in the ascidian nervous system. Dev Growth Differ *51*, 207–220. https://doi.org/10.1111/j.1440-169X.2009.01105.x.

Horie, T., Shinki, R., Ogura, Y., Kusakabe, T.G., Satoh, N., and Sasakura, Y. (2011). Ependymal cells of chordate larvae are stem-like cells that form the adult nervous system. Nature *469*, 525–528. https://doi.org/10.1038/nature09631.

Hudson, C. (2016). The central nervous system of ascidian larvae. Wiley Interdiscip Rev Dev Biol https://doi.org/10.1002/wdev.239.

Hudson, C., Darras, S., Caillol, D., Yasuo, H., and Lemaire, P. (2003). A conserved role for the MEK signalling pathway in neural tissue specification and posteriorisation in the invertebrate chordate, the ascidian Ciona intestinalis. Development *130*, 147–159. https://doi.org/10.1242/dev.00200.

Ikuta, T., and Saiga, H. (2007). Dynamic change in the expression of developmental genes in the ascidian central nervous system: revisit to the tripartite model and the origin of the midbrain-hindbrain boundary region. Dev. Biol. *312*, 631–643. https://doi.org/10.1016/j.ydbio.2007.10.005.

Imai, K.S., Satoh, N., and Satou, Y. (2002). Region specific gene expressions in the central nervous system of the ascidian embryo. Mech Dev *119 Suppl 1*, S275-7. .

Imai, K.S., Stolfi, A., Levine, M., and Satou, Y. (2009). Gene regulatory networks underlying the compartmentalization of the Ciona central nervous system. Development *136*, 285–293. https://doi.org/10.1242/dev.026419.

Jamieson, D., and Roberts, A. (2000). Responses of young Xenopus laevis tadpoles to light dimming: possible roles for the pineal eye. J Exp Biol *203*, 1857–1867. .

Kajiwara, S., and Yoshida, M. (1985). Changes in Behavior and Ocellar Structure during the Larval Life of Solitary Ascidians. Biol. Bull. *169*, 565–577. https://doi.org/Doi 10.2307/1541299.

Kamesh, N., Aradhyam, G.K., and Manoj, N. (2008). The repertoire of G protein-coupled receptors in the sea squirt Ciona intestinalis. BMC Evol Biol *8*, 129. https://doi.org/10.1186/1471-2148-8-129.

Kamino, K., Kondo, Y., Nakajima, A., Honda-Kitahara, M., Kaneko, K., and Sawai, S. (2017). Fold-change detection and scale invariance of cell–cell signaling in social amoeba. Proc. Natl. Acad. Sci. *114*, E4149–E4157. https://doi.org/10.1073/pnas.1702181114.

Kikkawa, T., Obayashi, T., Takahashi, M., Fukuzaki-Dohi, U., Numayama-Tsuruta, K., and Osumi, N. (2013). Dmrta1 regulates proneural gene expression downstream of Pax6 in the mammalian telencephalon. Genes Cells *18*, 636–649. https://doi.org/10.1111/gtc.12061.

Kirkeby, A., Grealish, S., Wolf, D.A., Nelander, J., Wood, J., Lundblad, M., Lindvall, O., and Parmar, M. (2012). Generation of Regionally Specified Neural Progenitors and Functional Neurons from Human Embryonic Stem Cells under Defined Conditions. Cell Rep. *1*, 703–714. https://doi.org/10.1016/j.celrep.2012.04.009.

Knudsen, E.I. (2020). Evolution of neural processing for visual perception in vertebrates. J. Comp. Neurol. *528*, 2888–2901. https://doi.org/10.1002/cne.24871.

Kourakis, M.J., Borba, C., Zhang, A., Newman-Smith, E., Salas, P., Manjunath, B., and Smith, W.C. (2019). Parallel visual circuitry in a basal chordate. ELife *8*, e44753. https://doi.org/10.7554/eLife.44753.

Kourakis, M.J., Bostwick, M., Zabriskie, A., and Smith, W.C. (2021). Disruption of left-right axis specification in Ciona induces molecular, cellular, and functional defects in asymmetric brain structures. BMC Biol. *19*, 141. https://doi.org/10.1186/s12915-021-01075-4.

Kusakabe, T., and Tsuda, M. (2007). Photoreceptive systems in ascidians. Photochem Photobiol *83*, 248–252. https://doi.org/10.1562/2006-07-11-IR-965.

Kusakabe, T., Kusakabe, R., Kawakami, I., Satou, Y., Satoh, N., and Tsuda, M. (2001). Ci-opsin1, a vertebrate-type opsin gene, expressed in the larval ocellus of the ascidian Ciona intestinalis. FEBS Lett *506*, 69–72. .

Kusakabe, T., Yoshida, R., Ikeda, Y., and Tsuda, M. (2004). Computational discovery of DNA motifs associated with cell type-specific gene expression in Ciona. Dev. Biol. *276*, 563–580. https://doi.org/10.1016/j.ydbio.2004.09.037.

Lacalli, T. (2018). Amphioxus, motion detection, and the evolutionary origin of the vertebrate retinotectal map. EvoDevo *9*, 6. https://doi.org/10.1186/s13227-018-0093-2.

Lacalli, T.C. (2006). Prospective protochordate homologs of vertebrate midbrain and MHB, with some thoughts on MHB origins. Int. J. Biol. Sci. 104–109. https://doi.org/10.7150/ijbs.2.104.

Lagutin, O.V. (2003). Six3 repression of Wnt signaling in the anterior neuroectoderm is essential for vertebrate forebrain development. Genes Dev. *17*, 368–379. https://doi.org/10.1101/gad.1059403.

Lamb, T.D. (2013). Evolution of phototransduction, vertebrate photoreceptors and retina. Prog Retin Eye Res *36*, 52–119. https://doi.org/10.1016/j.preteyeres.2013.06.001.

Lamb, T.D., Collin, S.P., and Pugh, E.N. (2007). Evolution of the vertebrate eye: opsins, photoreceptors, retina and eye cup. Nat Rev Neurosci *8*, 960–976. https://doi.org/10.1038/nrn2283.

Larderet, I., Fritsch, P.M.J., Gendre, N., Neagu-Maier, G.L., Fetter, R.D., Schneider-Mizell, C.M., Truman, J.W., Zlatic, M., Cardona, A., and Sprecher, S.G. (2017). Organization of the Drosophila larval visual circuit. Elife *6*. https://doi.org/ARTN e28387 10.7554/eLife.28387.

Lemaire, L.A., Cao, C., Yoon, P.H., Long, J., and Levine, M. (2021). The hypothalamus predates the origin of vertebrates. Sci. Adv. *7*, eabf7452. https://doi.org/10.1126/sciadv.abf7452.

Lemaire, P., Smith, W.C., and Nishida, H. (2008). Ascidians and the plasticity of the chordate developmental program. Curr. Biol. CB *18*, R620-31. https://doi.org/10.1016/j.cub.2008.05.039.

Lin, J.Y., Knutsen, P.M., Muller, A., Kleinfeld, D., and Tsien, R.Y. (2013). ReaChR: a red-shifted variant of channelrhodopsin enables deep transcranial optogenetic excitation. Nat Neurosci *16*, 1499–1508. https://doi.org/10.1038/nn.3502.

Luk, K.C., Rymar, V.V., Munckhof, P. van den, Nicolau, S., Steriade, C., Bifsha, P., Drouin, J., and Sadikot, A.F. (2013). The transcription factor Pitx3 is expressed selectively in midbrain dopaminergic neurons susceptible to neurodegenerative stress. J. Neurochem. *125*, 932–943. https://doi.org/10.1111/jnc.12160.

Lyashenko, E., Niepel, M., Dixit, P.D., Lim, S.K., Sorger, P.K., and Vitkup, D. (2020). Receptor-based mechanism of relative sensing and cell memory in mammalian signaling networks. ELife *9*, e50342. https://doi.org/10.7554/eLife.50342.

Marsden, K.C., Beattie, J.B., Friedenthal, J., and Carroll, R.C. (2007). NMDA receptor activation potentiates inhibitory transmission through GABA receptor-associated protein-dependent exocytosis of GABA(A) receptors. J. Neurosci. Off. J. Soc. Neurosci. *27*, 14326–14337. https://doi.org/10.1523/JNEUROSCI.4433-07.2007.

Marsh, E.D., Nasrallah, M.P., Walsh, C., Murray, K.A., Nicole Sunnen, C., McCoy, A., and Golden, J.A. (2016). Developmental interneuron subtype deficits after targeted loss of Arx. BMC Neurosci. *17*, 35. https://doi.org/10.1186/s12868-016-0265-8.

Mast, S.O. (1921). Reactions to light in the larvae of the ascidians, Amaroucium constellatum and Amaroucium pellucidum with special reference to photic orientation. J Exp Zool *34*, 149–187. .

Matsunaga, E., Araki, I., and Nakamura, H. (2001). Role of Pax3/7 in the tectum regionalization. Development *128*, 4069–4077. .

Mazet, F., Hutt, J.A., Milloz, J., Millard, J., Graham, A., and Shimeld, S.M. (2005). Molecular evidence from Ciona intestinalis for the evolutionary origin of vertebrate sensory placodes. Dev. Biol. *282*, 494–508. https://doi.org/10.1016/j.ydbio.2005.02.021.

McHenry, M.J. (2005). The morphology, behavior, and biomechanics of swimming in ascidian larvae. Can. J. Zool. *83*, 62–74. https://doi.org/10.1139/z04-157.

Moret, F., Christiaen, L., Deyts, C., Blin, M., Joly, J.S., and Vernier, P. (2005a). The dopamine-synthesizing cells in the swimming larva of the tunicate Ciona intestinalis are located only in the hypothalamus-related domain of the sensory vesicle. Eur J Neurosci *21*, 3043–3055. https://doi.org/10.1111/j.1460-9568.2005.04147.x.

Moret, F., Christiaen, L., Deyts, C., Blin, M., Vernier, P., and Joly, J.S. (2005b). Regulatory gene expressions in the ascidian ventral sensory vesicle: evolutionary relationships with the vertebrate hypothalamus. Dev. Biol. *277*, 567–579. https://doi.org/10.1016/j.ydbio.2004.11.004.

Myronenko, A., and Song, X. (2010). Point set registration: coherent point drift. IEEE Trans Pattern Anal Mach Intell *32*, 2262–2275. https://doi.org/10.1109/TPAMI.2010.46.

Nakagawa, M., Miyamoto, T., Ohkuma, M., and Tsuda, M. (1999). Action spectrum for the photophobic response of Ciona intestinalis (Ascidieacea, Urochordata) larvae implicates retinal protein. Photochem Photobiol *70*, 359–362. .

Nakamura, M.J., Terai, J., Okubo, R., Hotta, K., and Oka, K. (2012). Three-dimensional anatomy of the Ciona intestinalis tailbud embryo at single-cell resolution. Dev. Biol. *372*, 274–284. https://doi.org/10.1016/j.ydbio.2012.09.007.

Newman-Smith, E., Kourakis, M.J., Reeves, W., Veeman, M., and Smith, W.C. (2015). Reciprocal and dynamic polarization of planar cell polarity core components and myosin. Elife *4*. https://doi.org/10.7554/eLife.05361.

Nicol, D., and Meinertzhagen, I.A. (1988). Development of the central nervous system of the larva of the ascidian, Ciona intestinalis L. II. Neural plate morphogenesis and cell lineages during neurulation. Dev. Biol. *130*, 737–766. .

Nicol, D., and Meinertzhagen, I.A. (1991). Cell counts and maps in the larval central nervous system of the ascidian Ciona intestinalis (L.). J Comp Neurol *309*, 415–429. https://doi.org/10.1002/cne.903090402.

Nilsson, D.E. (2009). The evolution of eyes and visually guided behaviour. Philos Trans R Soc Lond B Biol Sci *364*, 2833–2847. https://doi.org/10.1098/rstb.2009.0083.

Nishida, H. (1987). Cell lineage analysis in ascidian embryos by intracellular injection of a tracer enzyme. III. Up to the tissue restricted stage. Dev. Biol. *121*, 526–541. .

Nishino, A., Okamura, Y., Piscopo, S., and Brown, E.R. (2010). A glycine receptor is involved in the organization of swimming movements in an invertebrate chordate. BMC Neurosci *11*, 6. https://doi.org/10.1186/1471-2202-11-6.

Okamura, Y., Nishino, A., Murata, Y., Nakajo, K., Iwasaki, H., Ohtsuka, Y., Tanaka-Kunishima, M., Takahashi, N., Hara, Y., Yoshida, T., et al. (2005). Comprehensive analysis of the ascidian genome reveals novel insights into the molecular evolution of ion channel genes. Physiol Genomics *22*, 269–282. https://doi.org/10.1152/physiolgenomics.00229.2004.

Olsen, R.W. (2014). Analysis of gamma-aminobutyric acid (GABA) type A receptor subtypes using isosteric and allosteric ligands. Neurochem Res *39*, 1924–1941. https://doi.org/10.1007/s11064-014-1382-3.

Oonuma, K., Tanaka, M., Nishitsuji, K., Kato, Y., Shimai, K., and Kusakabe, T.G. (2016). Revised lineage of larval photoreceptor cells in Ciona reveals archetypal collaboration between neural tube and neural crest in sensory organ formation. Dev. Biol. *420*, 178–185. https://doi.org/10.1016/j.ydbio.2016.10.014.

Pál, B. (2018). Involvement of extrasynaptic glutamate in physiological and pathophysiological changes of neuronal excitability. Cell. Mol. Life Sci. *75*, 2917–2949. https://doi.org/10.1007/s00018-018-2837-5.

Paoletti, P., Bellone, C., and Zhou, Q. (2013). NMDA receptor subunit diversity: impact on receptor properties, synaptic plasticity and disease. Nat. Rev. Neurosci. *14*, 383–400. https://doi.org/10.1038/nrn3504.

Peng, G. (2006). Lhx5 promotes forebrain development and activates transcription of secreted Wnt antagonists. Development *133*, 3191–3200. https://doi.org/10.1242/dev.02485.

Pennati, R., Candiani, S., Biggiogero, M., Zega, G., Groppelli, S., Oliveri, D., Parodi, M., De Bernardi, F., and Pestarino, M. (2007). Developmental expression of tryptophan hydroxylase gene in Ciona intestinalis. Dev Genes Evol *217*, 307–313. https://doi.org/10.1007/s00427-007-0138-3.

Pergner, J., and Kozmik, Z. (2017). Amphioxus photoreceptors - insights into the evolution of vertebrate opsins, vision and circadian rhythmicity. Int J Dev Biol *61*, 665–681. https://doi.org/10.1387/ijdb.170230zk.

Randel, N., Asadulina, A., Bezares-Calderon, L.A., Veraszto, C., Williams, E.A., Conzelmann, M., Shahidi, R., and Jekely, G. (2014). Neuronal connectome of a sensory-motor circuit for visual navigation. Elife *3*. https://doi.org/10.7554/eLife.02730.

Razy-Krajka, F., Brown, E.R., Horie, T., Callebert, J., Sasakura, Y., Joly, J.S., Kusakabe, T.G., and Vernier, P. (2012). Monoaminergic modulation of photoreception in ascidian: evidence for a proto-hypothalamo-retinal territory. BMC Biol *10*, 45. https://doi.org/10.1186/1741-7007-10-45.

Reeves, W.M., Wu, Y., Harder, M.J., and Veeman, M.T. (2017). Functional and evolutionary insights from the *Ciona* notochord transcriptome. Development *144*, 3375–3387. https://doi.org/10.1242/dev.156174.

Roure, A., Rothbacher, U., Robin, F., Kalmar, E., Ferone, G., Lamy, C., Missero, C., Mueller, F., and Lemaire, P. (2007). A multicassette Gateway vector set for high throughput and comparative analyses in ciona and vertebrate embryos. PLoS One *2*, e916. https://doi.org/10.1371/journal.pone.0000916.

Roy, A., Gonzalez-Gomez, M., Pierani, A., Meyer, G., and Tole, S. (2014). Lhx2 Regulates the Development of the Forebrain Hem System. Cereb. Cortex *24*, 1361–1372. https://doi.org/10.1093/cercor/bhs421.

Ryan, K., and Meinertzhagen, I.A. (2019). Neuronal identity: the neuron types of a simple chordate sibling, the tadpole larva of Ciona intestinalis. Curr. Opin. Neurobiol. *56*, 47–60. https://doi.org/10.1016/j.conb.2018.10.015.

Ryan, K., Lu, Z., and Meinertzhagen, I.A. (2016). The CNS connectome of a tadpole larva of Ciona intestinalis (L.) highlights sidedness in the brain of a chordate sibling. Elife *5*, e16962. https://doi.org/10.7554/eLife.16962.

Ryan, K., Lu, Z., and Meinertzhagen, I.A. (2017). Circuit Homology between Decussating Pathways in the Ciona Larval CNS and the Vertebrate Startle-Response Pathway. Curr Biol *27*, 721–728. https://doi.org/10.1016/j.cub.2017.01.026.

Ryan, K., Lu, Z., and Meinertzhagen, I.A. (2018). The peripheral nervous system of the ascidian tadpole larva: Types of neurons and their synaptic networks. J Comp Neurol *526*, 583–608. https://doi.org/10.1002/cne.24353.

Sakurai, D., Goda, M., Kohmura, Y., Horie, T., Iwamoto, H., Ohtsuki, H., and Tsuda, M. (2004). The role of pigment cells in the brain of ascidian larva. J Comp Neurol *475*, 70–82. https://doi.org/10.1002/cne.20142.

Salas, P., Vinaithirthan, V., Newman-Smith, E., Kourakis, M.J., and Smith, W.C. (2018). Photoreceptor specialization and the visuomotor repertoire of the primitive chordate Ciona. J Exp Biol *221*. https://doi.org/10.1242/jeb.177972.

Satoh, N. (1994). Developmental biology of ascidians (Cambridge England ; New York: Cambridge University Press).

Satoh, N. (2014). Developmental genomics of ascidians (Hoboken, New Jersey: Wiley Blackwell).

Schredelseker, T., Veit, F., Dorsky, R.I., and Driever, W. (2020). Bsx Is Essential for Differentiation of Multiple Neuromodulatory Cell Populations in the Secondary Prosencephalon. Front. Neurosci. *14*, 525. https://doi.org/10.3389/fnins.2020.00525.

Shetty, A.S., Godbole, G., Maheshwari, U., Padmanabhan, H., Chaudhary, R., Muralidharan, B., Hou, P.-S., Monuki, E.S., Kuo, H.-C., Rema, V., et al. (2013). Lhx2 regulates a cortex-specific mechanism for barrel formation. Proc. Natl. Acad. Sci. *110*, E4913–E4921. https://doi.org/10.1073/pnas.1311158110.

Shoval, O., Goentoro, L., Hart, Y., Mayo, A., Sontag, E., and Alon, U. (2010). Fold-change detection and scalar symmetry of sensory input fields. Proc Natl Acad Sci U A *107*, 15995–16000. https://doi.org/10.1073/pnas.1002352107.

Spagnuolo, D.A., and Palladino, D.A. COMBINED FUNCTIONAL, CELLULAR AND BEHAVIOURAL STUDIES TO GET INSIGHTS ON SENSORY ORGANS OF CIONA ROBUSTA LARVAE. 95. .

Stehman, S.V. (1997). Selecting and interpreting measures of thematic classification accuracy. Remote Sens. Environ. *62*, 77–89. .

Stokes, M.D., and Holland, N.D. (1995). Ciliary Hovering in Larval Lancelets (=Amphioxus). Biol. Bull. *188*, 231–233. https://doi.org/10.2307/1542300.

Suzuki, D.G., Murakami, Y., Escriva, H., and Wada, H. (2015). A comparative examination of neural circuit and brain patterning between the lamprey and amphioxus reveals the evolutionary origin of the vertebrate visual center. J Comp Neurol *523*, 251–261. https://doi.org/10.1002/cne.23679.

Svane, I.B., and Young, C.M. (1989). The ecology and behavior of ascidian larvae. Mar Biol Rev *27*. .

Takahashi, T., and Holland, P.W.H. (2004). Amphioxus and ascidian Dmbx homeobox genes give clues to the vertebrateorigins of midbrain development. Development *131*, 3285–3294. https://doi.org/10.1242/dev.01201.

Takamura, K., Egawa, T., Ohnishi, S., Okada, T., and Fukuoka, T. (2002). Developmental expression of ascidian neurotransmitter synthesis genes. I. Choline acetyltransferase and

acetylcholine transporter genes. Dev Genes Evol *212*, 50–53. https://doi.org/10.1007/s00427-001-0205-0.

Takamura, K., Minamida, N., and Okabe, S. (2010). Neural map of the larval central nervous system in the ascidian Ciona intestinalis. Zool. Sci *27*, 191–203. https://doi.org/10.2108/zsj.27.191.

Thompson, J.A., Zembrzycki, A., Mansouri, A., and Ziman, M. (2008). Pax7 is requisite for maintenance of a subpopulation of superior collicular neurons and shows a diverging expression pattern to Pax3 during superior collicular development. BMC Dev. Biol. *8*, 62. https://doi.org/10.1186/1471-213X-8-62.

Toresson, H., Potter, S.S., and Campbell, K. (2000). Genetic control of dorsal-ventral identity in the telencephalon: opposing roles for Pax6 and Gsh2. Development *127*, 4361–4371. .

Tresser, J., Chiba, S., Veeman, M., El-Nachef, D., Newman-Smith, E., Horie, T., Tsuda, M., and Smith, W.C. (2010). doublesex/mab3 related-1 (dmrt1) is essential for development of anterior neural plate derivatives in Ciona. Development *137*, 2197–2203. https://doi.org/10.1242/dev.045302.

Tsuda, M., Sakurai, D., and Goda, M. (2003a). Direct evidence for the role of pigment cells in the brain of ascidian larvae by laser ablation. J Exp Biol *206*, 1409–1417. .

Tsuda, M., Kawakami, I., and Shiraishi, S. (2003b). Sensitization and habituation of the swimming behavior in ascidian larvae to light. Zool. Sci *20*, 13–22. https://doi.org/10.2108/zsj.20.13.

Veeman, M.T., Chiba, S., and Smith, W.C. (2011). Ciona genetics. Methods Mol Biol *770*, 401–422. https://doi.org/10.1007/978-1-61779-210-6_15.

Vogeler, S., Carboni, S., Li, X., Ireland, J.H., Miller-Ezzy, P., and Joyce, A. (2021). Cloning and characterisation of NMDA receptors in the Pacific oyster, Crassostrea gigas (Thunberg, 1793) in relation to metamorphosis and catecholamine synthesis. Dev. Biol. *469*, 144–159. https://doi.org/10.1016/j.ydbio.2020.10.008.

Vopalensky, P., Pergner, J., Liegertova, M., Benito-Gutierrez, E., Arendt, D., and Kozmik, Z. (2012). Molecular analysis of the amphioxus frontal eye unravels the evolutionary origin of the retina and pigment cells of the vertebrate eye. Proc Natl Acad Sci U A *109*, 15383–15388. https://doi.org/10.1073/pnas.1207580109.

Wada, H., Saiga, H., Satoh, N., and Holland, P.W. (1998). Tripartite organization of the ancestral chordate brain and the antiquity of placodes: insights from ascidian Pax-2/5/8, Hox and Otx genes. Development *125*, 1113–1122. .

Wagner, E., and Levine, M. (2012). FGF signaling establishes the anterior border of the Ciona neural tube. Development *139*, 2351–2359. https://doi.org/10.1242/dev.078485.

Wehr, R., Mansouri, A., de Maeyer, T., and Gruss, P. (1997). Fkh5-deficient mice show dysgenesis in the caudal midbrain and hypothalamic mammillary body. Dev. Camb. Engl. *124*, 4447–4456. .

Wong, E.H., Kemp, J.A., Priestley, T., Knight, A.R., Woodruff, G.N., and Iversen, L.L. (1986). The anticonvulsant MK-801 is a potent N-methyl-D-aspartate antagonist. Proc. Natl. Acad. Sci. U. S. A. *83*, 7104–7108. https://doi.org/10.1073/pnas.83.18.7104.

Yoshida, K., and Saiga, H. (2008). Left–right asymmetric expression of Pitx is regulated by the asymmetric Nodal signaling through an intronic enhancer in Ciona intestinalis. Dev. Genes Evol. *218*, 353–360. https://doi.org/10.1007/s00427-008-0230-3.

Yoshida, R., Sakurai, D., Horie, T., Kawakami, I., Tsuda, M., and Kusakabe, T. (2004). Identification of neuron-specific promoters in Ciona intestinalis. Genesis *39*, 130–140. https://doi.org/10.1002/gene.20032.

Yoshizawa, M., and Jeffery, W.R. (2008). Shadow response in the blind cavefish Astyanax reveals conservation of a functional pineal eye. J Exp Biol *211*, 292–299. https://doi.org/10.1242/jeb.012864.

Young, C.M., and Chia, F.S. (1985). An Experimental Test of Shadow Response Function in Ascidian Tadpoles. J. Exp. Mar. Biol. Ecol. *85*, 165–175. https://doi.org/Doi 10.1016/0022-0981(85)90141-8.

Zander, J.F., Munster-Wandowski, A., Brunk, I., Pahner, I., Gomez-Lira, G., Heinemann, U., Gutierrez, R., Laube, G., and Ahnert-Hilger, G. (2010). Synaptic and vesicular coexistence of VGLUT and VGAT in selected excitatory and inhibitory synapses. J Neurosci *30*, 7634–7645. https://doi.org/10.1523/JNEUROSCI.0141-10.2010.

Zega, G., Thorndyke, M.C., and Brown, E.R. (2006). Development of swimming behaviour in the larva of the ascidian Ciona intestinalis. J Exp Biol *209*, 3405–3412. https://doi.org/10.1242/jeb.02421.

Zega, G., Biggiogero, M., Groppelli, S., Candiani, S., Oliveri, D., Parodi, M., Pestarino, M., De Bernardi, F., and Pennati, R. (2008). Developmental expression of glutamic acid decarboxylase and of gamma-aminobutyric acid type B receptors in the ascidian Ciona intestinalis. J Comp Neurol *506*, 489–505. https://doi.org/10.1002/cne.21565.

Zeller, R.W. (2018). Electroporation in Ascidians: History, Theory and Protocols. Adv Exp Med Biol *1029*, 37–48. https://doi.org/10.1007/978-981-10-7545-2_5.